2018

# Surveying Host Innate Immune Responses To Interferon Antagonist-Deficient Murine Coronaviruses

Aaron Brian Volk
*Loyola University Chicago*

## Recommended Citation

Volk, Aaron Brian, "Surveying Host Innate Immune Responses To Interferon Antagonist-Deficient Murine Coronaviruses" (2018). *Master's Theses*. 3758.
https://ecommons.luc.edu/luc_theses/3758

LOYOLA UNIVERSITY CHICAGO

# SURVEYING HOST INNATE IMMUNE RESPONSES TO INTERFERON ANTAGONIST-DEFICIENT MURINE CORONAVIRUSES

A THESIS SUBMITTED TO

THE FACULTY OF THE GRADUATE SCHOOL

IN CANDIDACY FOR THE DEGREE OF

MASTER OF SCIENCE

PROGRAM IN INFECTIOUS DISEASE AND IMMUNOLOGY

BY

AARON B. VOLK

CHICAGO, ILLINOIS

DECEMBER 2018

# ACKNOWLEDGMENTS

I am lucky to have many people to thank for their unwavering support throughout my time as a graduate student. First, I would like to thank Dr. Susan Baker, whose incredible mentorship and enthusiasm for teaching made my master's project the success that it was. Of my cohort, I was the first to choose a PI/mentor because I realized after just a few days into my rotation in Dr. Baker's lab that I had found a home there (thankfully, Dr. Baker agreed).

It has been a wonderful honor to work and study under Dr. Baker's guidance alongside the rest of her lab. To Deng and Amornrat (who both deserve a shout-out for helping me with Figures 7 and 21 of this document!), Rob, Matt, Amani, and Yazmin: thank you for your technical assistance in lab, for showing me what good science looks like, and most importantly for your friendship.

I would also like to thank the rest of my thesis committee: Dr. Gail Reid for allowing me to shadow her and for offering much-needed advice and support as I applied to medical schools, Dr. Tom Gallagher for graciously allowing me to use one of his lab's desks, and Dr. Francis Alonzo for teaching the Baker lab how to generate and culture primary macrophages.

I owe special thanks to Dr. Qunfeng Dong, whose calm, reassuring guidance gave me the confidence and technical know-how that I needed in order to accurately carry out the bioinformatic analyses in this project.

Finally, I am truly grateful to my friends and family. To my closest friends—Josie, Stephanie, Ryan, and Sam—I owe a great debt. Your friendship is invaluable to me and I could not have done this without you all. My partner, Tony, is a daily source of emotional support for me and I am so thankful for his patience, love, and genuine interest in my graduate work. Most importantly, I want to thank my parents, Ron and Lisa, without whose unconditional love and encouragement an accomplishment like this never would have been possible.

May we do work that matters. Vale la pena, it's worth the pain.
—Gloria E. Anzaldúa

## TABLE OF CONTENTS

# LIST OF TABLES

# LIST OF FIGURES

# LIST OF ABBREVIATIONS

| | |
|---|---|
| BCV | bovine coronavirus |
| BMDM | bone marrow-derived macrophage |
| BMM | bone marrow/macrophage |
| CoV | coronavirus |
| DAVID | Database for Annotation, Visualization and Integrated Discovery |
| DEG | differentially-expressed gene |
| DMEM | Dulbecco's modified Eagle's medium |
| DMV | double-membrane vesicle |
| dpi | days post-infection |
| dsRNA | double-stranded RNA |
| DUB | deubiquitinase |
| DUB-mut | deubiquitinase-mutant |
| E | envelope |
| EndoU | endoribonuclease |
| EndoU-mut | endoribonuclease-mutant |
| ER | endoplasmic reticulum |
| FIPV | feline infectious peritonitis virus |
| HAE | human airway epithelial |
| hpi | hours post-infection |

| | |
|---|---|
| IBV | infectious bronchitis coronavirus |
| IFN | interferon |
| IFNAR | interferon-α receptor |
| ISG | interferon-stimulated gene |
| M | membrane |
| MERS | Middle East respiratory syndrome |
| MHV | mouse hepatitis coronavirus |
| MTase | methyltransferase |
| N | nucleocapsid |
| NF-κB | nuclear factor kappa-light-chain-enhancer of activated B cells |
| nsp | nonstructural protein |
| OAS | oligoadenylate synthase |
| ORF | open reading frame |
| PAMP | pathogen-associated molecular pattern |
| PEDV | porcine epidemic diarrhea coronavirus |
| PKR | protein kinase R |
| PRR | pattern recognition receptor |
| QC | quality control |
| qRT-PCR | quantitative reverse transcription polymerase chain reaction |
| RNA-seq | RNA-sequencing |
| S | spike |
| SARS | severe acute respiratory syndrome |
| SR50 | single-read 50 nucleotide |

| | |
|---|---|
| ssRNA | single-stranded RNA |
| ST | swine testis |
| TGEV | transmissible gastroenteritis coronavirus |
| UCGF | University of Chicago Genomics Facility |
| UPR | unfolded protein response |
| WT | wild type |
| βME | β -mercaptoethanol |

# ABSTRACT

Two coronaviruses (CoVs)—severe acute respiratory syndrome (SARS) virus and Middle East respiratory syndrome (MERS) virus—have emerged in the 21st century from animal reservoirs into the human population, each causing an epidemic associated with significant disease and mortality. CoV epidemics are currently only controllable by rigorous public health measures; no targeted therapeutics or vaccines exist to treat or prevent any human CoV infection. One method of generating attenuated CoV strains to be studied as vaccine candidates involves specifically disrupting CoV-encoded interferon (IFN) antagonists, thereby rendering the virus vulnerable to host innate antiviral immunity. Deubiquitinating (DUB) activity encoded within CoV nonstructural protein (nsp) 3 and endoribonuclease (EndoU) activity encoded within nsp15 are both reported to suppress IFN-mediated antiviral immunity during infection. Using murine hepatitis virus (MHV) as a model CoV, we generated viruses that encode enzymatically deficient forms of these proteins and have shown that EndoU-mutant- and DUB-mutant-MHV elicit significantly increased type I IFN responses relative to the parental wild type (WT) strain. However, despite similar patterns of IFN induction by both mutant viruses, we previously found that only the EndoU-mut virus is attenuated and does not cause detectable disease in mice, whereas DUB-mut-MHV is not attenuated *in vivo* and causes disease similar to WT-MHV. The purpose of this project was to investigate the host transcriptional response to infection with EndoU-mut-, DUB-mut-, and WT-MHV in primary murine macrophages using RNA-sequencing (RNA-seq) technology to examine the cellular dynamics that underlie the remarkably distinct phenotypes of EndoU-mut- and DUB-mut-MHV infections in mice.

The results of our RNA-seq experiments and subsequent bioinformatic analyses demonstrate that WT-MHV infection led to profound transcriptional dysregulation of hundreds of host genes, many of which encode proteins that are involved in inflammation, antiviral defense, signaling pathways, and transcription regulation. DUB-mut-MHV elicited a statistically indistinguishable transcriptional response of all but a select few genes relative to WT-MHV. In stark contrast, EndoU-mut-MHV-infected cells exhibited markedly diminished transcription of the vast majority of genes that were induced by DUB-mut- and WT-MHV, leading to a profoundly distinct transcriptional response overall. Both EndoU-mut- and DUB-mut-MHV induced significantly higher expression of multiple type I IFN isoforms relative to the WT virus, with the EndoU-mut strain prompting a dramatically higher IFN response than even the DUB-mut virus. Together, the results of this work suggest that the induction of IFN alone is not a sufficient marker for mutant CoV attenuation or of widespread dysregulation of host gene expression in the context of studying interferon antagonist-deficient coronavirus strains; rather, the magnitude and timing of IFN expression are critical. We conclude that there is a threshold of interferon expression that must be crossed before a host macrophage mounts a differential response to an IFN antagonist-deficient coronavirus that is capable of limiting the infection. Furthermore, we propose that MHV encodes a hierarchy of IFN antagonists that suppress and/or evade the host immune response in different ways and to different degrees. The results of this project advance what is known about how coronavirus-encoded IFN antagonists fine-tune the host response to viral infection and we hope that this work will guide future studies involving interferon antagonist-deficient coronaviruses being evaluated as vaccine candidates.

# CHAPTER I

# BACKGROUND

## Coronaviruses Are Important and Diverse Pathogens

Recent outbreaks of the Middle East respiratory syndrome (MERS) virus (2012-present) and the severe acute respiratory syndrome (SARS) virus (2002-2004) demonstrated that coronaviruses (CoVs) can emerge from animal reservoirs to pose significant threats to human populations worldwide. Four other CoVs—HCoV-229E, -OC43, -NL63, and -HKU1—are known to infect the human population and generally cause relatively mild, self-limiting cold symptoms in immunocompetent individuals but can lead to lethal disease in children and immunocompromised or immunosuppressed patients (Dijkman and van der Hoek 2009; Gaunt *et al*. 2010). Both SARS-CoV and MERS-CoV cause highly lethal respiratory disease in their hosts: about 35-40% of patients infected with MERS-CoV, and about 10% of patients infected with SARS-CoV, died during the course of each respective outbreak (Hui *et al*. 2014). Importantly, these epidemics were controlled only by virtue of public health initiatives and strict quarantine protocols. At present, no vaccines or specific antivirals are available for the prevention or treatment of any CoV infection, which is cause for concern given the possibility of a novel, lethal CoV akin to SARS-CoV or MERS-CoV emerging into the human population in the future. Without such therapies, the human immune system alone seems to be inherently inefficient in staving off CoV replication and pathogenesis, rendering the host vulnerable to severe coronaviral disease (Perlman and Netland 2009; de Wit *et al*. 2016).

Depicted in Figure 1 is a phylogenetic tree of 50 CoVs within the *Coronavirinae* subfamily of the *Coronaviridae* order. All of these viruses assemble into virions that share the same basic structural morphology, which features a "corona" (halo) of spike (S) proteins for which the family is named (Figure 2) (Almeida and Tyrrell 1967; Virology: Coronaviruses 1968). The *Coronaviridae* subfamily includes, in addition to human-tropic viruses, a host of other CoVs that infect and cause disease in a variety of animal species, including cattle, swine, mice, cats, and others. Several of these animal CoVs, such as bovine coronavirus (BCV) and porcine epidemic diarrhea virus (PEDV), wreak economic havoc on the agriculture industries of developed nations like China and the United States by causing infections and fatalities among millions of calves and piglets (Cho and Yoon 2014; Lee 2015; Sunniva Oma *et al*. 2016). Other animal CoVs—feline infectious peritonitis virus (FIPV), for example—are important veterinary viruses because they cause untreatable and often lethal infections in animals that are kept as pets (Pedersen 2014). Murine hepatitis coronavirus (MHV), which is in the same genus as SARS- and MERS-CoV and is commonly used in biomedical research as a mouse model for human CoV infections, is used in the study described herein. Collectively, several members of the *Coronaviridae* subfamily pose serious threats to human populations due to their abilities to act as direct human pathogens (SARS-CoV, MERS-CoV, etc.), impact our food supply by devastating the agriculture industry (BCV, PEDV, etc.), and even cause disease in our domesticated pets (FIPV). It is critical, therefore, that we study how these viruses interact with their hosts and identify the factors that make them such successful pathogens throughout the animal kingdom. The ultimate goal of such research is to develop vaccines and targeted antivirals that we can use to protect ourselves from current CoV strains as well as from novel strains that may emerge in the future.

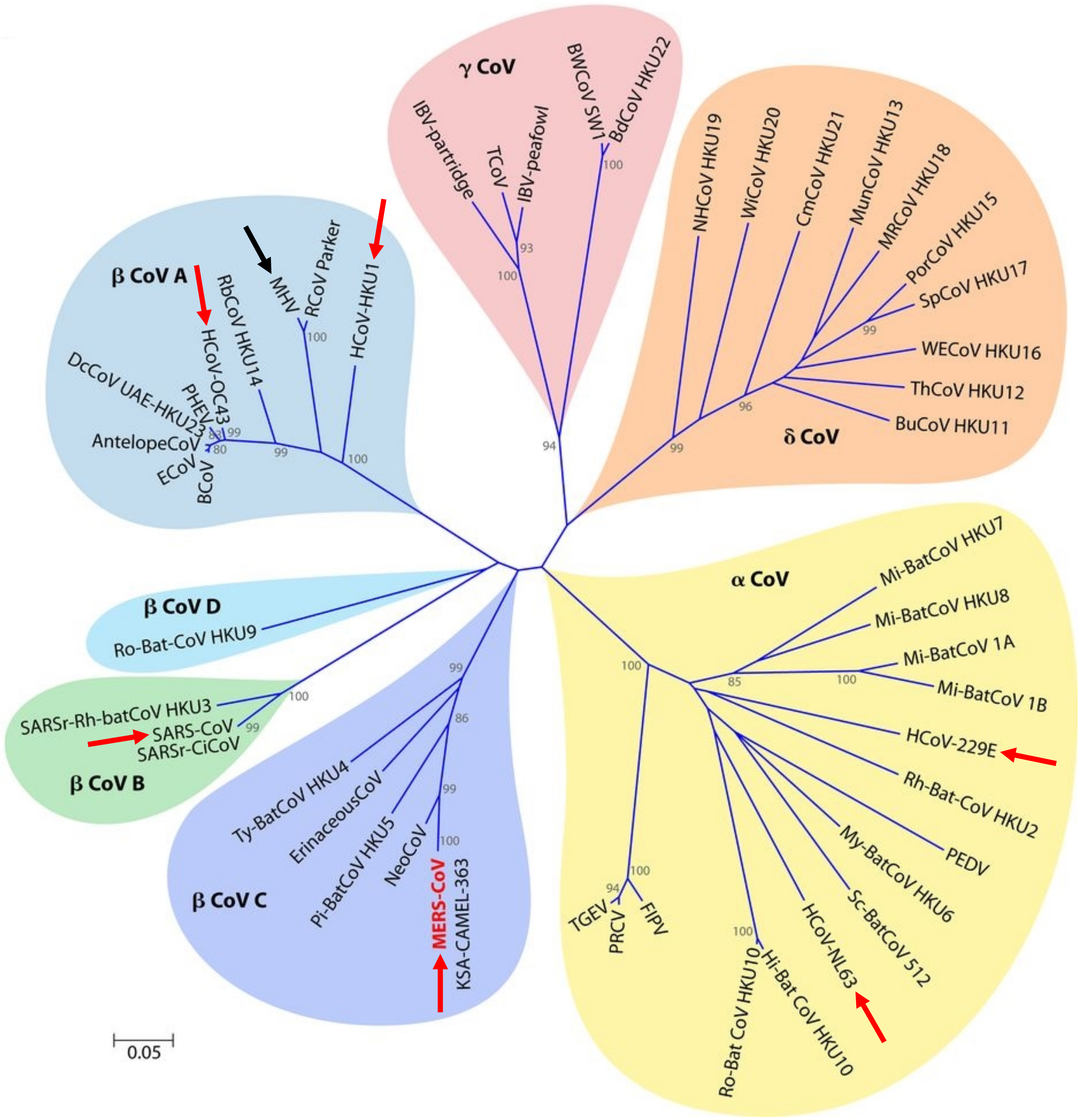

**Figure 1. Phylogenetic Tree of the *Coronaviridae* Subamily.** Phylogenetic tree depicting 50 CoVs, organized by genus (α-, β-, δ-, and λ-CoVs) and lineage (β-CoV A, B, C, and D). This tree was constructed by Chan *et al*. (2015) based on partial nucleotide sequences of the RNA-dependent RNA polymerase encoded by each virus. The scale bar represents the degree of sequence identity—*via* the estimated number of substitutions within the RdRp per 20 nucleotides—as a measure of relationship between viruses. Red arrows denote the 6 CoVs that infect humans; black arrow denotes the murine hepatitis virus (MHV) that was used as a model CoV in the experiments described herein. Modified with permission from Chan *et al*. (2015).

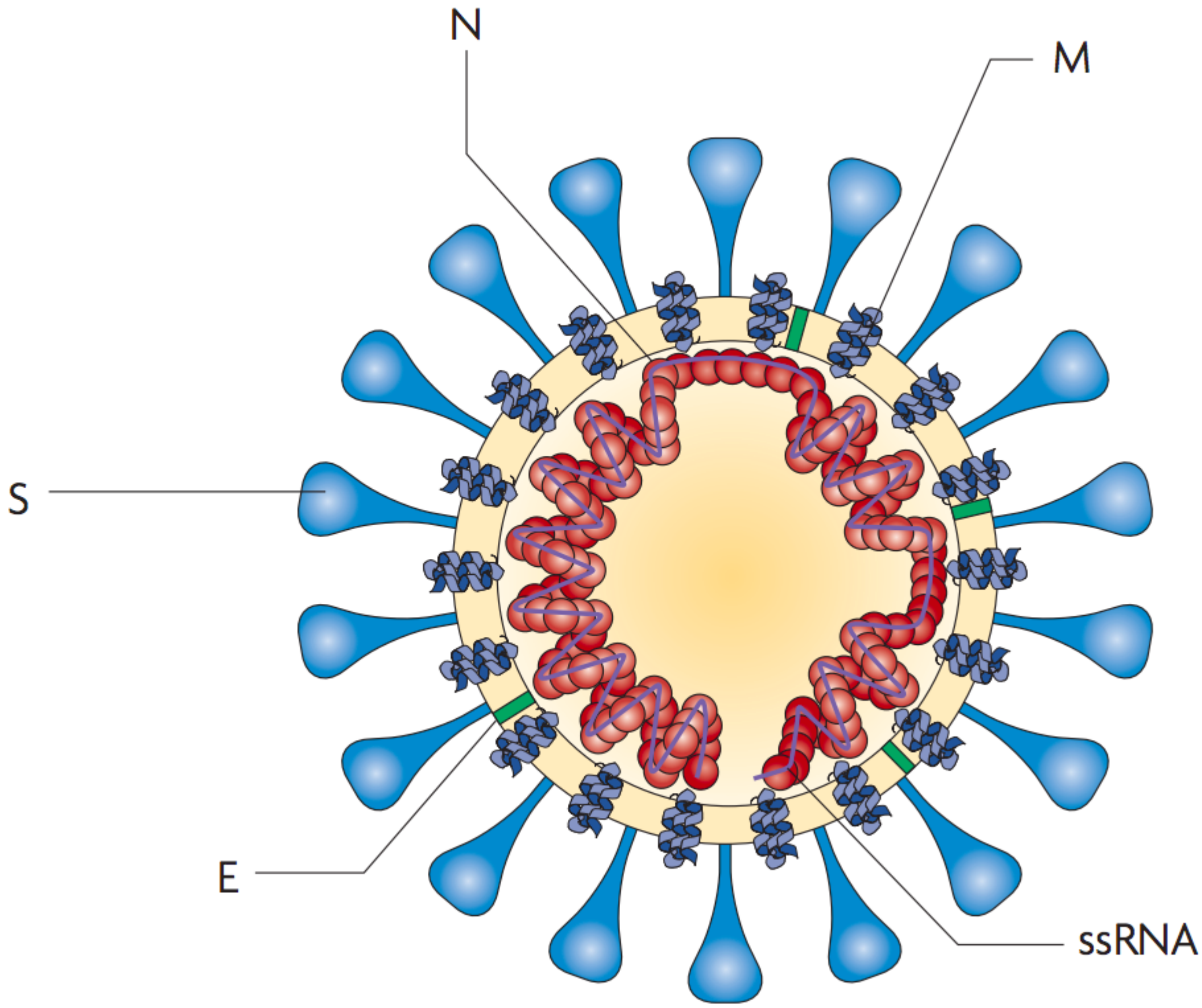

**Figure 2. Typical Structure of a Coronavirus Virion.** Coronaviruses form spherical, enveloped virions, each of which encloses a single copy of the positive-sense single-stranded RNA (ssRNA) viral genome. Encapsulating and protecting the viral genome are nucleocapsid (N) proteins. Viral envelope (E), membrane (M), and spike (S) proteins integrate into the host-derived envelope. S proteins form a “crown” around each virion that is readily discernible by electron microscopy. Used with permission from Perlman and Netland (2009).

## The Type I Interferon Response

One key factor that contributes to the inefficient human immune response to CoV infections, and therefore to the success of coronaviruses as pathogens, is the impressive ability of these viruses to evade and/or antagonize the type I interferon (IFN) response, an antiviral process that falls under the umbrella of innate immunity (Perlman and Netland 2009; Zhou *et al*. 2014; de Wit *et al*. 2016). Type I IFNs, which include IFN-α and IFN-β, are signaling molecules that act as a first line of defense against viral pathogens and some non-viral intracellular infections (Bogdan *et al*. 2004; Ivashkiv and Donlin 2014). These cytokines are expressed by a variety of cell types in response to the detection of pathogen-associated molecular patterns (PAMPs) by cellular pathogen recognition receptors (PRRs), as illustrated in Figure 3. For the recognition of viruses, relevant PRRs include Toll-like receptors (TLRs) 3, 7/8, and 9; RIG-I-like receptors (RLRs) RIG-I and MDA-5; and the protein kinase R (PKR) and 2′-5′ oligoadenylate synthetase (OAS)/RNase L systems (Hsu *et al*. 2004; Thompson *et al*. 2011). These receptors, which are shared between mice and humans, recognize 3 main types of viral PAMPs: double-stranded RNA (dsRNA), single-stranded RNA (ssRNA) in endosomes, and cytoplasmic DNA. Upon activation by PAMPs, many PRRs initiate signaling pathways that culminate in the induction of IFN and other genes. Shown in Figure 3, once IFNs are translated, cleaved, and secreted, they act in an autocrine and paracrine manner to induce an antiviral state within infected and neighboring cells through signaling pathways that terminate in the expression of antiviral IFN-stimulated genes (ISGs) (Haller *et al*. 2006; Ivashkiv and Donlin 2014). The canonical signaling pathway for the type I IFNs through the interferon-$\alpha$ receptor (IFNAR) is depicted in Figure 4. Many of the ISGs and inflammatory genes that are expressed as a consequence of IFN signaling restrict the virus by impeding the replication and expression of the viral genome, halting translation, inducing apoptosis, initiating inflammation, and a number of other processes that collectively combat the viral infection (Haller *et al*. 2006; Schoggins and Rice 2011; Schneider *et al*. 2014). Type I IFNs are also crucial activators of innate immune cells like macrophages and natural killer cells, which participate in coordinating the immune response, phagocytosing apoptotic virus-infected cells, and killing virus-infected cells (Fujimoto *et al*. 2000; Paolini *et al*. 2015).

Finally, type I IFNs can enhance the adaptive immune response to viral infections by augmenting the functions of B and T cells (Ivashkiv and Donlin 2014).

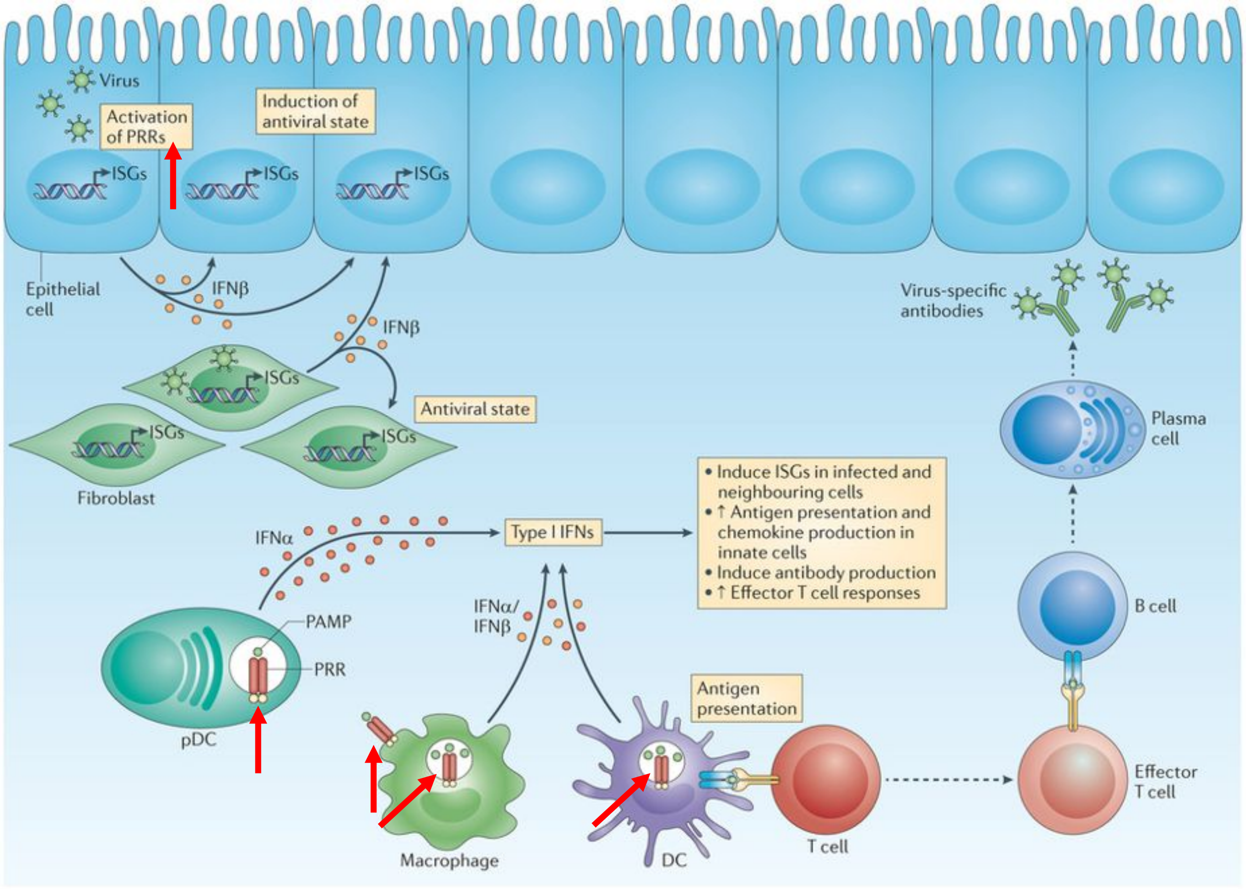

Nature Reviews | Immunology

**Figure 3. The type I IFN Response to Viral Infection.** The IFN response is initiated when viral pathogen-associated patterns (PAMPs) are detected by host pattern recognition receptors (PRRs) (red arrows) in infected cells. Upon activation of PRRs, non-immune cells such as epithelial cells and fibroblasts (top left) express and secrete type I IFN-β (yellow circles), which act as signaling molecules in a paracrine and autocrine fashion to induce an antiviral state within infected and uninfected host cells. This antiviral state is achieved as a consequence of IFN signaling, which induces the expression of IFN-stimulated genes (ISGs) that act in a variety of ways to counteract the viral life cycle. Additionally, immune cells such as macrophages and dendritic cells (DCs) (bottom) secrete large amounts of type I IFN-α and IFN-β (orange and yellow circles, respectively) upon PRR activation, which contribute to the innate and adaptive antiviral response by inducing the expression of ISGs in host cells, increasing the production of chemokines to attract antiviral immune cells including macrophages and natural killer cells, and enhancing the activities of B and T cells. Modified with permission from Ivashkiv and Donlin (2014).

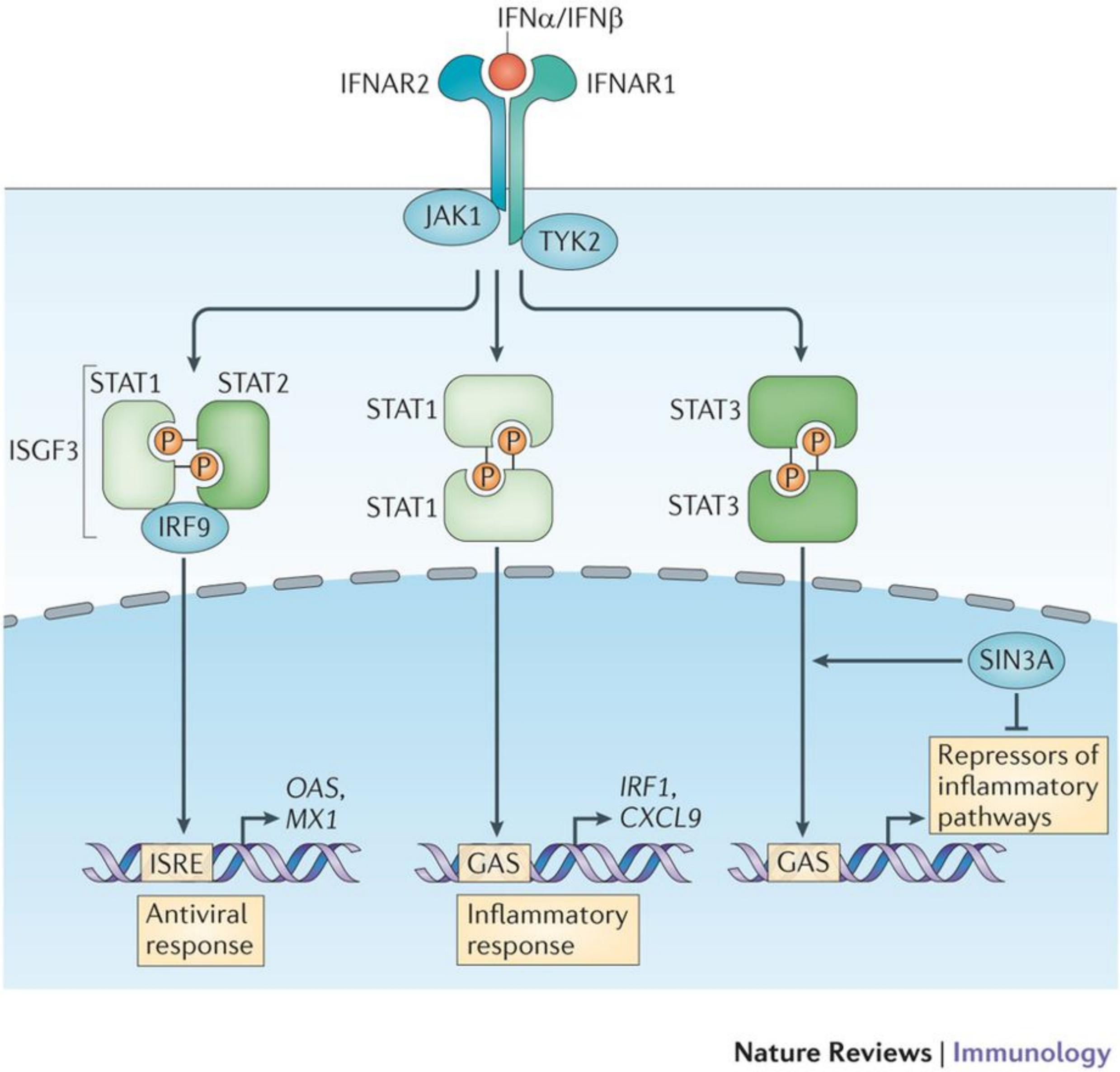

**Figure 4. Canonical Type I IFN Signaling Pathway through the IFN-α Receptor.** Type I IFN-α and IFN-β bind the type I IFN-α receptor (IFNAR) on infected and uninfected cells and initiate signaling cascades that terminate in the expression of ISGs (OAS, MX1, IRF1, etc.), inflammatory molecules (CXCL9, etc.), and regulators of the inflammatory response. Shown are the 3 primary signaling cascades that comprise the canonical type I IFN signaling pathway. Used with permission from Ivashkiv and Donlin (2014).

In summary, the type I IFN response lies at the foundation of our bodies' ability to combat a viral infection. It is therefore no surprise that many viruses, including CoVs, have evolved a variety of means to escape, dysregulate, and/or antagonize the IFN induction and signaling pathways at various points in order to ensure that their replication and dissemination within the host remain unchecked (Schulz and Mossman 2016). Figure 5 illustrates a number of known strategies, many of which are achieved by CoV proteins (indicated with red arrows), that viruses employ to counteract the induction of IFN expression. It is critical that we study the diverse mechanisms through which CoVs disrupt the antiviral innate immune response so that we might guide the development therapeutics and vaccines that can be used to enhance the ability of our immune system to successfully clear a coronaviral infection.

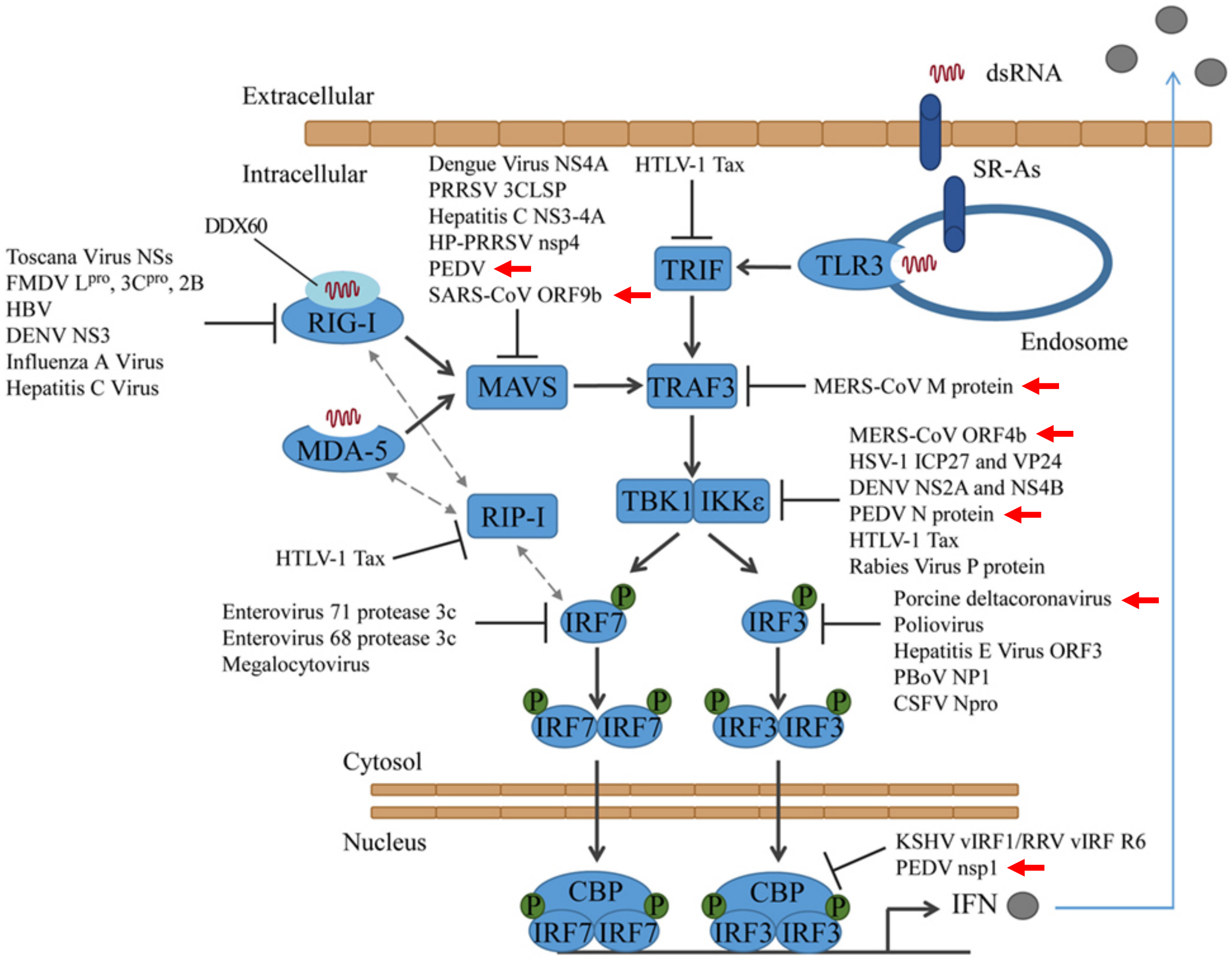

**Figure 5. Viral Strategies for Evading and Antagonizing IFN Induction.** Most viruses encode at least one factor that acts to antagonize and/or evade the activation of the signaling pathways that initiate the expression of type I IFN (grey circles) during infection. Shown are some of these viruses, including several coronaviruses and CoV-encoded factors (indicated with red arrows), and the respective step(s) at which they act to suppress the induction of IFN. Modified with permission from Schulz and Mossman (2016).

## CoV-encoded IFN Antagonists

Coronaviruses are particularly successful at potently dysregulating the IFN and subsequent ISG responses during infection, thereby enabling these viruses to evade clearance by the host's immune system (Cheung *et al*. 2005; Frieman *et al*. 2009; Menachery *et al*. 2014; Deng *et al*. 2017; Kindler *et al*. 2017). In particular, it is increasingly clear that CoVs *delay* the IFN and ISG responses during infection, which ultimately contributes to unchecked viral replication and the development of disease (Menachery *et al*. 2014; Channappanavar *et al*. 2016). In their study using a mouse-adapted strain of human SARS-CoV, Channappanavar *et al*. (2016) found that treating SARS-CoV-infected mice with exogenous type I IFN early during infection at 6 hpi completely protected the mice from weight loss and clinical disease, whereas infected mice treated with type I IFN at 24 hpi experienced weight loss and succumbed to clinical disease at the same rate as untreated infected mice. These results, which are depicted schematically in Figure 6, demonstrated that the timing of the IFN response is critical in determining the outcome of a CoV infection and suggest that CoVs are capable of delaying IFN expression until a point in time when it is no longer sufficient to curb viral replication or clinical disease. Therefore, understanding the mechanism(s) by which CoVs achieve this delay in the IFN response might reveal strategies for combatting coronaviral disease.

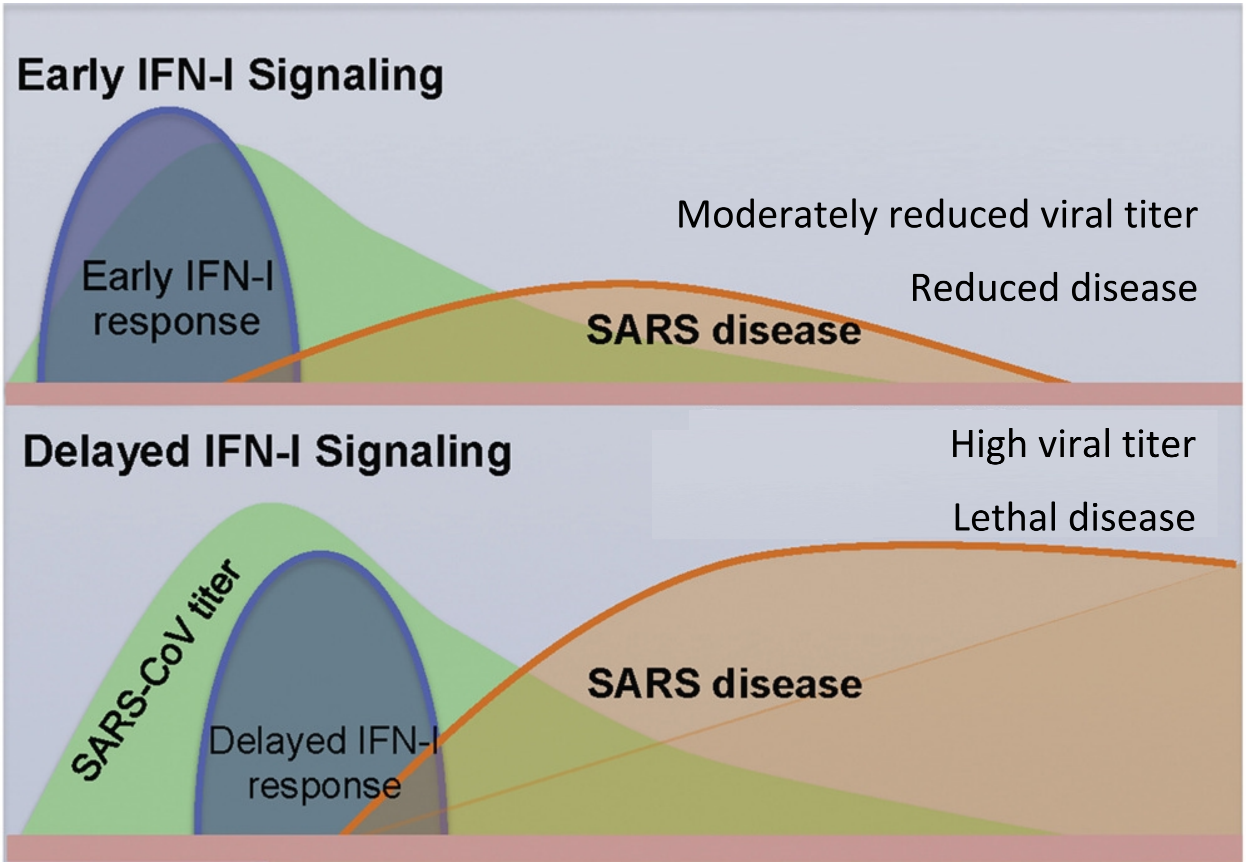

**Figure 6. CoVs Delay the Type I IFN Response.** (Bottom) Mice infected with a mouse-adapted strain of SARS-CoV exhibited a delay in the induction of the type I IFN response (blue curves) during infection, which contributed to high viral titer (green curves) and lethal disease (orange curves). (Top) Treatment of SARS-CoV-infected mice with type I IFN early during infection led to an earlier type I IFN response, which in turn was associated with moderately reduced viral titer, significant reduction in clinical disease, and mouse survival. This experiment suggests that CoVs delay the type I IFN response during infection, thereby identifying coronavirus-mediated IFN antagonism as a target for the development of vaccines and antiviral therapeutics. Modified with permission from Channappanavar *et al*. (2016).

Coronaviruses possess the largest genomes of all RNA viruses (ranging from approximately 27-32 kilobases, depending on the particular virus), which encode many structural and nonstructural proteins (nsps), as illustrated for MHV in Figure 7 (Gorbalenya *et al*. 2006). Many CoV-nsps are known to participate in the replication process of the virus, depicted in Figure 8, as components of viral replication complexes within virus-induced double-membrane vesicles (DMVs) (Gosert *et al*. 2002; Knoops *et al*. 2008). Previous studies from our lab and other groups revealed that several murine and human coronavirus structural and nonstructural proteins, albeit encoding markedly different enzymatic and structural properties, also participate in IFN antagonism during infection (Frieman *et al*. 2009; Schulz and Mossman 2016; Deng *et al*. 2017; Kindler *et al*. 2017). Two of these proteins—nsp3 and nsp15—were the focus of the project herein using MHV-A59 as a model coronavirus.

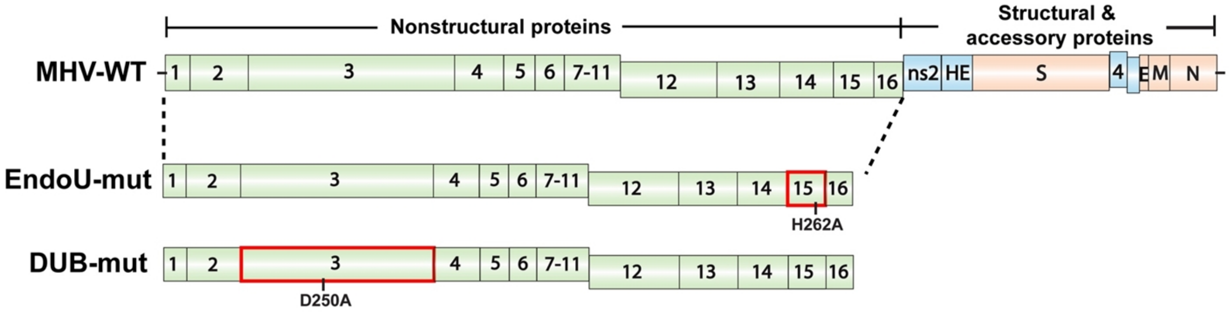

**Figure 7. Schematic diagram of EndoU-mut, DUB-mut, and WT-MHV genomes.** Illustration of the annotated genomes for WT-MHV A59 parental strain (Top), EndoU-mut- (Middle), and DUB-mut-MHV (Bottom). Structural, nonstructural, and accessory proteins are colored salmon, green, and blue, respectively. Mutations in EndoU-mut- and DUB-mut-MHV are listed below the target nsps (red boxes). Modified with permission from Deng *et al*. (2017).

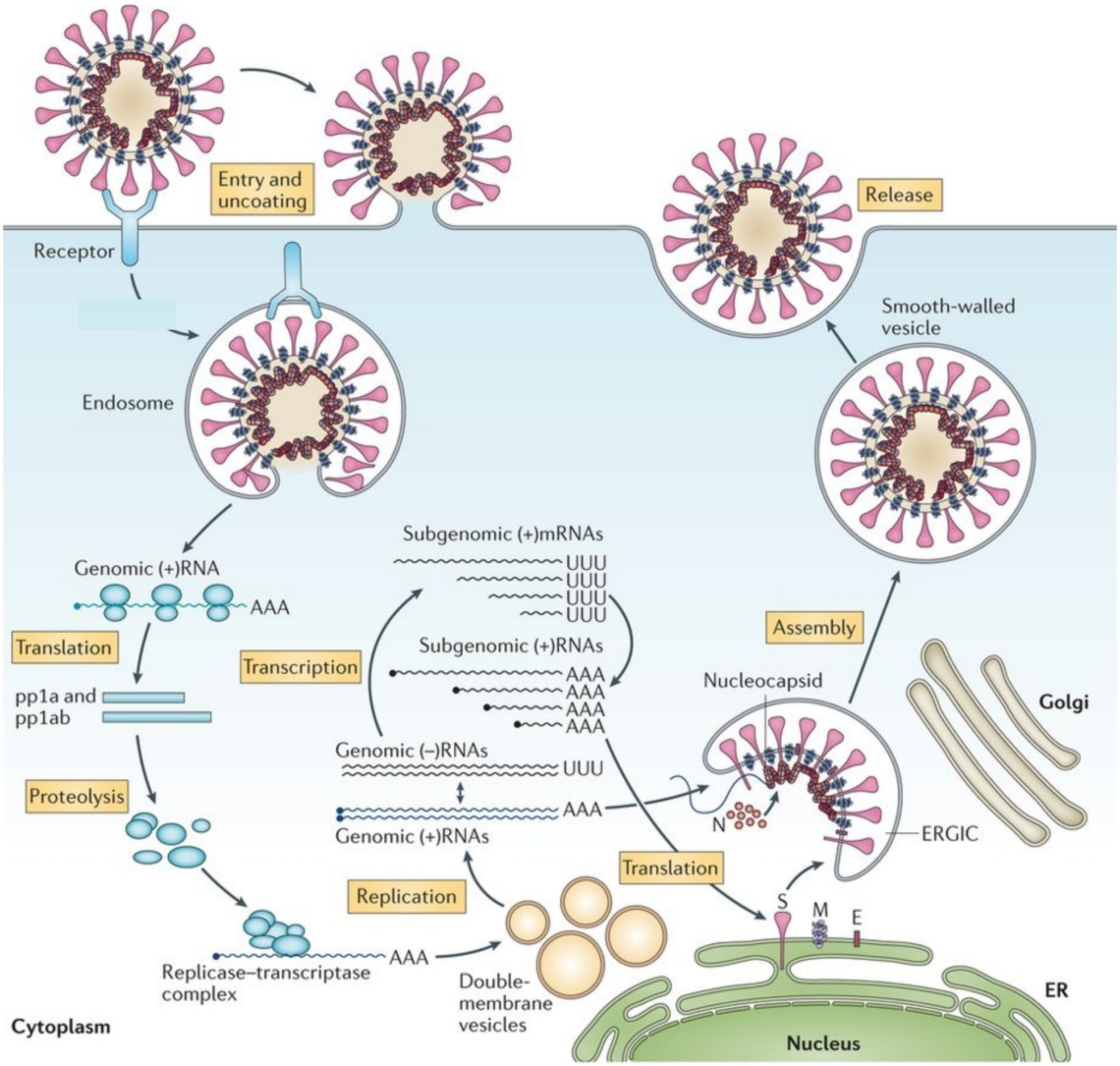

Nature Reviews | Microbiology

**Figure 8. Life Cycle of a Typical CoV.** Coronaviruses bind their respective cellular receptors *via* their S proteins (pink, top left). Upon entering the host cell by endocytosis, the viral envelope fuses with the membrane of the host endosome, releasing the viral genome. The genome is subsequently translated by host machinery into viral polyproteins pp1a and pp1ab, which are then cleaved into their constituent nsps by viral proteases (center left). The nsps comprise the viral replicase machinery (in the form of replication complexes), which is housed in host-derived DMVs (center bottom). Replication complexes coordinate transcription of the positive-sense viral genome into negative-sense RNAs, which are then either replicated and packaged into virions to be released as infectious particles (right), or reverse-transcribed into a nested set of subgenomic mRNAs (a unique hallmark of nidovirus replication for which the *Nidovirales* order is named) to be translated into viral structural proteins (center). Note that the positioning of the

viral membrane proteins in the ER should be inverted, such that the ectodomains of the proteins should protrude into the ER lumen. Used with permission from de Wit *et al*. (2016).

### Nsp3-DUB.

The nsp3 of MHV contains multiple functional domains with different enzymatic properties, including two papain-like protease (PLP) domains that are known to be critical for viral replication by cleaving the viral polyprotein into some of its constituent nsps (Ziebuhr *et al*. 2000; Mielech, Chen, *et al*. 2014; Chen *et al*. 2015; Lei *et al*. 2018). Other coronaviruses like PEDV and HCoV-NL63 also contain two PLPs (PLP1 and PLP2) within their nsp3s, whereas SARS-CoV and MERS-CoV only encode a single PLP domain (PLpro) in their respective nsp3 genes (Mielech, Chen, *et al*. 2014). In 2005 Sulea *et al*. published sequence homology data revealing that, in addition to its known protease activity, SARS-PLpro exhibited striking resemblance to known cellular deubiquitinase (DUB) herpesvirus-associated ubiquitin-specific protease (HAUSP, aka USP18). Shortly thereafter, two groups independently demonstrated that SARS-PLpro was indeed capable of deubiquitinating K48- and K63-linked polyubiquitin chains and showed that this DUB activity was dependent on catalytic residues within the protease domain (Barretto *et al*. 2005; Lindner *et al*. 2005). Deubiquitinating and deISGylating activities have since been reported in PEDV, HCoV-NL63, MERS-CoV, MHV, and other coronaviruses (Zheng *et al*. 2008; Frieman *et al*. 2009; Clementz *et al*. 2010; Xing *et al*. 2013; Mielech, Kilianski, *et al*. 2014). It is well-established that ubiquitination and deubiquitination of many proteins are critical post-translational modifications involved in the regulation of multiple innate immune pathways, including IFN induction and signaling pathways (Bibeau-Poirier and Servant 2008; Bhoj and Chen 2009; Fuchs 2012; Heaton *et al*. 2016). As such, an intriguing possibility is that the DUB activity of MHV-PLP2 deubiquitinates host factors in one or more of these pathways to disrupt the IFN response during infection.

That a coronavirus-encoded DUB might disrupt innate immune signaling pathways is not without precedent in nature; PLPs from several arteriviruses (which, along with CoVs, mesoniviruses, and roniviruses, comprise the *Nidovirales* order) have also been shown to antagonize the IFN response (Frias-Staheli *et al*. 2007; Sun *et al*. 2010; van Kasteren *et al*. 2012). However, whether or not CoV-encoded DUB activity contributes to suppression and/or evasion of antiviral immunity during infection remains unclear. For example, Wang *et al*. (2011) reported that MHV-PLP2 deubiquitinates TBK1, an important kinase involved in IRF3-mediated IFN induction, and Xing *et al*. (2013) demonstrated that PEDV-PLP2 deubiquitinates RIG-I and STING, two classic antiviral sensors that induce the expression of type I IFN. These studies point to a clear role for CoV-encoded DUBs as IFN antagonists. In contrast, Clementz *et al*. (2010) demonstrated that HCoV-NL63-PLP2 *inhibits* RIG-I- and TLR3-dependent induction of IFNβ even in the absence of catalytic activity and that SARS-PLpro does not require catalytic activity to inhibit IRF3- or NF-κB-dependent reporters. Mielech and Kilianski *et al*. (2014), on the other hand, concluded that catalytic activity *is* required for MERS-PLpro-mediated inhibition of a MAVS-induced IFNβ reporter and a nuclear factor kappa-light-chain-enhancer of activated B cells (NF-κB) reporter and that SARS- and MERS-PLpro both inhibit the expression of other pro-inflammatory cytokines. These seemingly contradictory reports could indicate that there exist strain-specific differences between coronavirus DUBs; they might also be explained at least in part by the distinct experimental procedures used by each group. Nevertheless, this evolving body of work strongly suggests that at least some CoV-PLPs antagonize innate immunity and implicates DUB activity as a potential IFN antagonist, invoking the need for additional research to further investigate this possibility.

### Nsp15-EndoU.

Recent work involving another coronavirus IFN antagonist, nsp15, has shown that it is associated with viral replication complexes during infection but, unlike nsp3, is not strictly required for the production of virus progeny (Deng *et al*. 2017; Kindler *et al*. 2017). Structural data and *in vitro* studies first indicated that nsp15 is an endoribonuclease that forms oligomers that recognize and cleave ss- and dsRNA species, with particular affinity for the 3'-ends of uridylates (Ivanov *et al*. 2004; Bhardwaj *et al*. 2006; Ricagno *et al*. 2006; Kang *et al*. 2007). Notably, the presence of an endoribonuclease (EndoU) domain is a genetic marker that is uniquely conserved among the vertebrate-infecting members of the *Nidovirales* order (but is apparently absent in several recently-characterized arthropod nidoviruses), potentially rendering it an excellent target for broad-spectrum rational vaccine design and antiviral therapies (Ivanov *et al*. 2004; Nga *et al*. 2011; Deng and Baker 2018). However, like nsp3-DUB activity, the role, mechanism(s), and specific target(s) of nsp15-EndoU activity during coronavirus infection are unclear. Some groups have reported that the preferred target of EndoU is ssRNA, while others demonstrated a preference for dsRNA (Bhardwaj *et al*. 2004; Ivanov *et al*. 2004). Recently, we and others showed that MHV-EndoU co-localizes with dsRNA within replication complexes and that infection with a mutant MHV strain encoding a catalytically-inactive EndoU resulted in increased accumulation of cytosolic dsRNA, collectively implicating dsRNAs—obligate intermediates in the replication of positive-sense RNA viruses—as the primary targets of EndoU (Deng *et al*. 2017; Kindler *et al*. 2017). These studies also provided compelling data to suggest that at least one role for EndoU activity during infection is to suppress the type I IFN response and limit apoptosis in macrophages in a manner that involves evasion and/or antagonism of host sensing by RIG-I, MDA-5, and the PKR and OAS/RNase L systems (Deng *et al*. 2017; Kindler *et al*. 2017). Thus, nsp15-EndoU is one of the newest additions to the ever-growing list of CoV-encoded IFN antagonists.

## IFN Antagonists Are Compelling Targets for Rational Vaccine Design

Due to its critical roles in initiating and mediating the innate antiviral response and even priming adaptive antiviral immunity, IFN induction and signaling must be antagonized and/or evaded by viruses in order for them to replicate and spread efficiently, a requirement that has led to the evolution of numerous strategies for IFN suppression in most viruses (Figure 5) (Haller *et al*. 2006; Schoggins and Rice 2011; Ivashkiv and Donlin 2014; Schulz and Mossman 2016). Because of this relationship between host immunity and viral antagonism, virus-encoded IFN antagonists like nsp3-DUB and nsp15-EndoU are appealing targets for the rational design of CoV vaccine strains. In addition to their roles as IFN antagonists, nsp3-DUB and nsp15-EndoU activities are ideal candidates for targeted vaccine design because they are conserved among most known nidoviruses, including the highly pathogenic SARS- and MERS-CoVs (Ivanov *et al*. 2004; Mielech, Chen, *et al*. 2014). A universal approach to generating live-attenuated versions of current and future CoVs might therefore be achieved by specifically disrupting conserved viral proteins like nsp3-DUB and nsp15-EndoU, thereby allowing for the rapid development of vaccines to protect against novel emergent strains. Conceptually, if the ability of a virus to evade and/or suppress the antiviral response can be disrupted without abrogating virus replication *in vitro*—an important requirement for vaccine production—perhaps such a live-attenuated virus will elicit a sufficient and appropriate immune response that will restrict its replication *in vivo* without causing disease and spur the induction of immunological memory that is protective against infection by the wild type strain. Notably, the logic of this strategy is supported by the results of the study shown in Figure 6, which suggested that manipulating the IFN response such that IFN signaling occurs earlier during SARS-CoV infection might be sufficient to attenuate the virus without causing clinical disease (Channappanavar *et al*. 2016). The possibility of generating live-attenuated virus strains by deleting or disrupting virus-encoded IFN antagonists is currently being studied for a number of viruses, including MHV, MERS-CoV, SARS-CoV, Nipah virus, measles virus, Sindbis virus, West Nile virus, respiratory syncytial virus, and influenza A virus (Talon *et al*. 2000; Laurent-Rolle *et al*. 2010; Simmons *et al*. 2010; Yoneda *et al*. 2010; Devaux *et al*. 2011; Teng 2012; Deng *et al*. 2017; Menachery, Gralinski, *et al*. 2017; Du *et al*. 2018; Menachery *et al*. 2018). Indeed, recent studies involving IFN antagonist-deficient strains of influenza A virus are in the proof-of-concept stage and have shown remarkable promise in the lab, demonstrating the potential for IFN antagonist-deficient viruses as live-attenuated vaccines *in vivo* (Du *et al*. 2018).

### EndoU-mut- and DUB-mut-MHV Vaccine Candidates.

Using a mutant strain of MHV that encodes a histidine to alanine substitution (H262A) in the catalytic triad of nsp15-EndoU, illustrated in Figure 7, we recently demonstrated the utility of EndoU activity as a target for vaccine design. The replication of EndoU-mut-MHV was profoundly attenuated *in vitro* in normal murine BMDMs but exhibited WT-like replication kinetics in macrophages that were deficient in type I IFN signaling; accordingly, we also found that this strain elicited robust expression of type I IFN during infection of wild type macrophages (Deng *et al*. 2017). Furthermore, EndoU-mut-MHV was strikingly attenuated *in vivo* (Figure 9) and inoculated mice were protected from disease upon subsequent challenge with the parental strain (Deng *et al*. 2017). In unpublished data from a manuscript in preparation, we also found that a different mutant strain of MHV encoding an aspartate to alanine substitution (D250A, Figure 7) that impairs the DUB—but not the protease—activity of MHV-PLP2 also induced earlier and more robust expression of type I IFN than the parental strain. We were surprised, therefore, when subsequent *in vivo* studies using this DUB-mutant-MHV reproducibly resulted in no statistically significant difference in mortality or clinical pathology in mice compared with infection using the WT parental strain (Deng *et al*. manuscript in preparation) (Figure 9). That two distinct MHV mutants, each encoding a different catalytic mutation in a different IFN antagonist, both amplified IFN expression during infection but were associated with dramatically different responses *in vivo* suggests that the mere induction of type I IFN during infection is not a sufficient marker for an effective live-attenuated coronavirus vaccine strain. Additionally, these data preliminarily indicate that nsp15 is capable of dysregulating the host response to a greater extent than nsp3, suggesting that CoVs encode a hierarchy of IFN antagonists that work in concert to modulate antiviral immunity at multiple steps. In the work described herein, we sought to determine how a host cell responds differently to EndoU-mut- and DUB-mut-MHV infections at the level of transcription in order to better understand the dynamics that might explain the distinct outcomes of infection with these mutant strains that we observed *in vivo*.

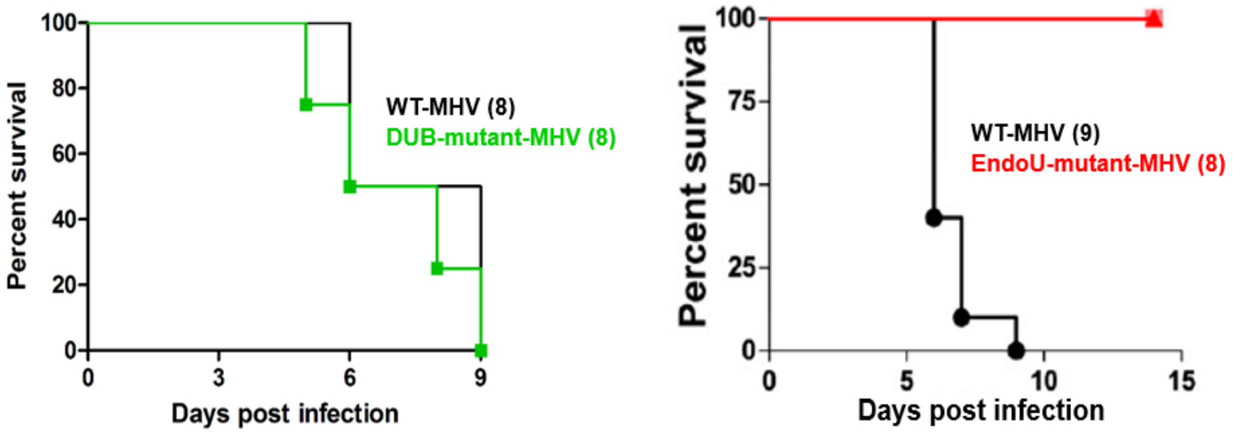

**Figure 9. Infection with DUB-mut- or EndoU-mut-MHV Leads to Distinct Responses in Mice.** (Left) Mice inoculated intracranially with 600 pfu of DUB-mut- or WT-MHV all succumbed to infection by 9 days-post infection. Used with permission from Deng *et al*., manuscript in preparation. (Right) Mice inoculated intracranially with 600 pfu of EndoU-mut-MHV all survived infection compared with WT-MHV-infected mice. Modified with permission from Deng *et al*. (2017). (Both panels) Mouse numbers for each group are indicated in parentheses. Data are representative of at least two independent experiments.

## Utilizing RNA-sequencing to Study CoV-infected Cells and Tissues

To investigate the factors that might contribute to the differential outcomes of *in vivo* infection with EndoU-mut- and DUB-mut-MHV (Figure 9), we applied RNA-sequencing (RNA-seq) to primary murine bone marrow-derived macrophages (BMDMs) infected with EndoU-mut-, DUB-mut, or WT-MHV to obtain a profile of the transcriptional responses elicited by each virus. Other groups have sequenced the transcriptomes of non-immune CoV-infected cell types infected using microarrays or RNA-seq, obtaining results that collectively suggest that the cell type and identity of the infecting virus largely dictate the transcriptional response to coronavirus infections. Table 1 outlines the major findings from a number of these published studies in various cell and tissue types. Given that the 6 known human CoVs most commonly cause respiratory disease in their hosts, RNA-seq or microarray experiments involving coronaviruses are most commonly performed in cells derived from lung and airway tissues such as Calu-3 cells, A549 cells, LA-4 cells, HAE cells, lung tissue homogenates, trachea tissue homogenates, among others (see Table 1 for references). Another common cell type used in transcriptomic studies of CoV infections is the fibroblast (17Cl-1 cells, MEFs, L cells, etc.) (Table 1). Notably, in 2005 Cheung *et al*. published the only paper of which we are aware in which full transcriptome sequencing (using microarray technology) was applied to CoV-infected macrophages (see Table 1); however, this publication only contains the microarray data for 35 genes at a single, early timepoint (3 hpi). The authors revealed that, although SARS-CoV did not induce the expression of any type I IFN gene by 3 hpi, the infected macrophages expressed appreciable amounts of several chemokines that are known to be important in the context of inflammatory disease, thereby implicating macrophage activity in SARS-CoV pathogenesis. Despite the important contributions that these studies have made toward our understanding of CoV-induced transcriptional changes, the striking lack of transcriptomic data from CoV-infected primary macrophages over multiple timepoints renders a large gap in what is known about how the innate immune system responds to these infections. What are the consequences of coronavirus-mediated IFN antagonism in the very cells that represent a first line of cellular defense against the viral infection?

| Cell or Tissue Type(s) | Coronavirus(es) | Major Finding(s) | Reference |
|---|---|---|---|
| 17Cl-1 (mouse fibroblast) cells | MHV-A59 | MHV induced an unfolded protein response (UPR) and host translation shutoff within the first 8 hours post-infection (hpi). | Irigoyen *et al*., preprint (2018) |
| mouse lung tissue homogenates | SARS-CoV | WT-SARS-CoV and a mutant SARS-CoV lacking its nsp16 (**Δ**nsp16) induced similar global transcriptional responses thru 2 dpi. By 6 dpi, the host response to **Δ**nsp16-SARS-CoV was markedly diminished relative to the WT parental strain. | Menachery *et al*., J Virol (2018) |
| chicken kidney tissue homogenates | IBV-SCDY2;<br>IBV-SCK2;<br>IBV-LDT3-A | Virulent IBV upregulated the expression of apoptosis genes and downregulated the expression of innate immune response and cellular metabolism genes by 5 and 6 dpi. | Liu *et al*., Microb Pathog (2017) |
| Calu-3 (human lung epithelium) cells;<br>human airway epithelial (HAE) cells | MERS-CoV | MERS-CoV lacking ORFs 3-5 dysregulated host responses by 24 hpi, marked by the induction of IFN and robust inflammation. | Menachery *et al*., mBio (2017) |
| Calu-3 cells | MERS-CoV;<br>SARS-CoV | The absence of SARS- and MERS-CoV-encoded 2'-O-methyltransferase (2'O-MTase) activity during infection yielded significant transcriptional changes thru 24 and 72 hpi, respectively, relative to WT infections. | Menachery *et al*., mSphere (2017) |
| A59 (human adenocarcinomic alveolar basal epithelium) cells;<br>HuH7 (hepatocellular carcinoma) cells | HCoV-229E | HCoV-229E fine-tuned NF-κB signaling, inducing NF-κB-dependent and independent gene expression, and reprogrammed the host's chromatin landscape thru 2 dpi. | Poppe *et al*., PLOS Pathog (2017) |

| Cell or Tissue Type(s) | Coronavirus(es) | Major Finding(s) | Reference |
|---|---|---|---|
| LA-4 (murine lung epithelium) cells | MHV-1 | MHV infection had a limited impact overall on the host transcriptome and only minimally upregulated the expression of IFNs and ISGs by 24 hpi. | VanLeuven *et al*., PLOS ONE (2017) |
| mouse lung tissue homogenates | SARS-CoV | By 9 dpi, several genes associated with wound healing and fibrosis were differentially expressed in the lungs of STAT1$^{-/-}$ mice and mice in which EGFR (epidermal growth factor receptor) is constitutively active. | Venkataraman *et al*., J Virol (2017) |
| mouse lung tissue homogenates | MERS-CoV | MERS-CoV profoundly perturbed the expression of thousands of host genes by 7 dpi, impacting the immune response in a way that implicated T cell and macrophage recruitment during infection. | Coleman *et al*., J Virol (2017) |
| 17Cl-1 cells | MHV-A59 | RNA-seq allowed for detailed profiling of the replication and translation kinetics of the MHV genome during the first 8 hpi. | Irigoyen *et al*., PLOS Pathog (2016) |
| mouse lung tissue homogenates | SARS-CoV | A number of immune response genes were differentially expressed upon SARS-CoV infection; the effects of Kepi and TNF expression were found to be of particular importance and were shown to oppositely impact pathogenesis. | McDermott *et al*., BMC Syst Biol (2016) |
| swine testis (ST) cells | TGEV | > 50 microRNAs, a number of which are immune-related, were found to be differentially expressed during infection. | Liu *et al*., PLOS ONE (2015) |
| marmoset lung tissue homogenates | MERS-CoV | Pathways associated with chemotaxis, cell proliferation, fibrogenesis, inflammation, vascularization, endothelial activation, tissue repair, and others were upregulated thru 3-6 dpi in individual animals. No expression of type I IFN was observed. | Falzarano *et al*., PLOS Pathog (2014) |

| Cell or Tissue Type(s) | Coronavirus(es) | Major Finding(s) | Reference |
|---|---|---|---|
| mouse embryonic fibroblast (MEF) cells; mouse lung tissue homogenates | SARS-CoV | Significant differential expression of > 5,000 lncRNAs occurred by 4 dpi upon infection of multiple strains of mice. | Josset *et al*., RNA Biol (2014) |
| Calu-3 cells | MERS-CoV; SARS-CoV | Both MERS- and SARS-CoV delayed type I IFN and subsequent ISG responses. | Menachery *et al*., mBio (2014) |
| mouse lung tissue homogenates | SARS-CoV | Thousands of novel transcripts were induced during SARS-CoV infection by 2 dpi; the induction of most of these transcripts was markedly diminished by 4 dpi. | Xiong *et al*., G3 (Bethesda) (2014) |
| chicken kidney tissue homogenates | IBV | Upon analysis 5 or 6 dpi, tissues exhibited significant differential expression of genes in multiple pathways. Regulation of > 100 genes associated with inflammation was found to be particularly important during the response to infection. | Cong *et al*., BMC Genomics (2013) |
| ST cells | TGEV | TGEV lacking its gene 7 upregulated host genes involved in the immune response, the interferon response, and inflammation by 12 hpi. | Cruz *et al*., J Virol (2013) |
| mouse spinal cord tissue homogenates | MHV-A59 | Expression of several genes involved in osteoclast or bone-resident macrophage function, as well as genes characterizing a Th1-biased cytokine/chemokine response, accompanied persistent MHV infection by 33 dpi. | Elliott *et al*., PLOS ONE (2013) |
| Crandell Rees feline kidney (CRFK) cells | FIPV | FIPV infection significantly upregulated a handful of genes by 3 hpi, the majority of which were associated with macrophage and Th1 cell functions and the regulation of apoptosis. | Harun *et al*., Virol J (2013) |

| Cell or Tissue Type(s) | Coronavirus(es) | Major Finding(s) | Reference |
|---|---|---|---|
| Calu-3 cells | MERS-CoV; SARS-CoV | MERS- and SARS-CoVs induced both overlapping and distinct transcriptional responses, especially after 12 hpi. | Josset *et al*. mBio (2013) |
| ferret lung tissue homogenates | SARS-CoV | Initial infection with SARS-CoV upregulated the expression of genes in innate immune and IFN signaling pathways thru 14 dpi and genes involved in adaptive immunity by 28 dpi. Reinfection did not stimulate IFN-responsive gene expression. | Cameron *et al*., PLOS ONE (2012) |
| Vero-E6 (monkey kidney epithelial) cells; MA-104 (monkey kidney epithelial) cells | SARS-CoV | SARS-CoV without its E protein upregulated the expression of a handful of genes, most of which are involved in the stress response, compared with WT-SARS-CoV infection thru 15 and 65 hpi, depending on the cell type. | DeDiego *et al*., PLOS Pathog (2011) |
| mouse lung tissue homogenates | SARS-CoV | SARS-CoV induced differential expression of more than 200 small RNAs by 2 dpi, revealing a role for non-protein-coding transcripts in coronavirus infections. | Peng *et al*., mBio (2011) |
| L cells (fibroblast-like) | MHV-A59 | Very few transcriptional changes occurred by 3 hpi; by 6 hpi a chemokine response was induced along with changes in RNA and protein metabolism, the cell cycle, and apoptosis. IFN was not triggered during infection. | Versteeg *et al*., J Gen Virol (2006) |
| chicken trachea tissue homogenates | IBV | Innate immune and Th1-biased adaptive immune responses were induced by 3 dpi in response to IBV infection. | Wang *et al*., Viral Immunol (2006) |
| human monocyte-derived macrophages | SARS-CoV | By 3 hpi, SARS-CoV-infected macrophages expressed no detectable type I IFN but did express several chemokines. | Cheung *et al*., J Virol (2005) |

**Table 1. Summary of Transcriptional Profiling Studies Involving Coronavirus-infected Cells and Tissues.** Entries are arranged first by date of publication and second, when necessary, by first author's last name.

## The Importance of Macrophages in CoV Infections.

For this project, we elected to utilize primary BMDMs, which are known to produce a substantial portion of secreted type I IFN during infection and are also potently IFN-responsive, relying on IFN signaling to dictate the induction and execution of an antiviral response (Ivashkiv and Donlin 2014). Given that the goal of this work was to investigate a host cell's transcriptional response to IFN antagonist-deficient mutant CoVs, it was important that we use an IFN-responsive cell type. Additionally, many CoVs—including MHV, SARS-CoV, MERS-CoV, HCoV-229E, IBV, FIPV, among others—have been shown to naturally and productively infect macrophages (Bang and Warwick 1960; Virelizier and Allison 1976; Collins 2002; Yilla *et al.* 2005; Zhou *et al.* 2014; Amarasinghe *et al.* 2017; Shirato *et al.* 2018). The IFN-responsiveness of macrophages (*via* signaling through the type I IFN-α receptor) has even been shown to be critical for controlling MHV infection, implicating macrophages and type I IFN signaling as key players in the anti-coronaviral immune response (Cervantes-Barragán *et al.* 2009). Likewise, depletion of macrophages has been shown to exacerbate MERS-CoV pathology in mice expressing the human MERS-CoV receptor (Coleman *et al.* 2017). On the other hand, Channappanavar *et al.* (2016) demonstrated that at least one type of macrophages—termed inflammatory monocyte-macrophages (IMMs)—accumulated during SARS-CoV infection and contributed to the development and worsening of severe disease. In a similar vein, Hartwig *et al.* (2014) showed that depletion of alveolar macrophages reduced MHV-induced morbidity and mortality in intranasally-infected mice. The work of Zhou *et al.* (2014) proposed that secretion of pro-inflammatory cytokines by macrophages exacerbates the development of severe pneumonia and respiratory dysfunction in patients infected with MERS-CoV. Taken together, the results of these studies indicate that IFN-responsive macrophages play a central role in the host's response to CoV infections and that dysregulated accumulation and/or transcriptional responses of certain types of macrophages may even contribute to the severity of coronavirus-induced disease.

A recent paper by Savarin *et al*. (2018) described the expression profiles of 754 genes in mouse BMDMs in response to an *in vivo* infection with a neurotropic strain of MHV (strain JHM) between 5-14 dpi using a gene expression panel technology called "nCounter." Although the method of expression profiling used by the authors did not involve global transcriptomic profiling, to our knowledge this is nevertheless the only published report that contains extensive gene expression profiling data from coronavirus-infected macrophages. The results of this study, which most notably revealed a mix of upregulated M1- and M2-associated gene expression in MHV-infected BMDMs, provide a partial view of a macrophage's transcriptional response to coronavirus infection. The authors concluded, in agreement with previous reports, that BMDMs likely do not play an essential role in the overall pathogenesis of MHV-JHM in their murine model of multiple sclerosis-like demyelination (Savarin *et al*. 2018). However, we speculate that the lack of data prior to 5 dpi leaves open the possibility of BMDM involvement in the early innate immune response to infection. Additionally, since gene expression was assessed in BMDMs that were isolated from the spinal milieu of infected mice, it is unclear whether or not the BMDMs were themselves infected by the virus. In order to investigate the *full* scope of the transcriptional response to CoV infection in macrophages, we determined that the use of microarray or RNA-seq technology is required. Using RNA-seq, we therefore sought to explore the dynamics of the transcriptional response that occurs in BMDMs upon MHV infection in the presence and absence of MHV-encoded IFN antagonists. The results of our work point to profound transcriptional dysregulation of nearly 2,900 host genes during MHV infection of murine BMDMs, including a staggering majority of which that were differentially regulated by our IFN antagonist-deficient mutants.

# CHAPTER II

# MATERIALS AND METHODS

## Viruses

EndoU-mut- and DUB-mut-MHV strains were derived from parental WT-MHV A59 strain (GenBank accession # AY910861) (Figure 7), all of which were generated by Dr. Xufang Deng, Loyola University Chicago, Maywood IL, by process of reverse genetics as described by Yount *et al*. (2002). All viruses were subjected to whole-genome sequencing to confirm the results of reverse genetics.

## Generation and Culture of Murine Bone Marrow-derived Macrophages

### Extraction of Bone Marrow from Mice.

To obtain BMDMs, total bone marrow was first extracted from the femurs of C57BL/6J mice (#000664, The Jackson Laboratory). Mice were euthanized by use of $CO_2$, their femurs removed, and the contents of the femoral marrow cavities were flushed out using Dulbecco's Modified Eagle's Medium (DMEM, #10-017-CV, Corning). The mixture of bone marrow + DMEM was centrifuged at 500 rpm for 1 min at 4 ºC, the supernatant transferred to a new tube and centrifuged again at 1500 rpm for 5 min at 4 ºC. The cell pellet from the second centrifugation was resuspended in 10 mL of DMEM, cells were counted, and $5 \times 10^6$ cells were plated in 15 mL of "bone marrow/macrophage medium" (BMM) medium supplemented with 0.1% $5 \times 10^{-2}$M β-mercaptoethanol (βME) in 100 x 26 mm Petri dishes (25387-030, VWR).

### Bone Marrow/Macrophage Medium.

The recipe for BMM medium is as follows: DMEM supplemented with 30% L929 cell supernatant (obtained as described below); 20% fetal bovine serum (FBS); 1% 0.2M L-glutamine; and 1% 0.1M sodium pyruvate. When differentiating bone marrow into BMDMs, BMM medium was also supplemented with 0.1% 5 x $10^{-2}$M (βME).

### L929 Cell Medium and Conditioned Supernatant.

L929 cells, which secrete macrophage colony-stimulating factor (M-CSF), were a gift from Dr. Francis Alonzo, Loyola University Chicago, Maywood IL. To generate L929 cell conditioned supernatant for use in BMM medium as described above, L929 cells were cultured in the following medium: DMEM supplemented with 10% FBS; 1% 0.2M L-glutamine; 1% 0.1M sodium pyruvate; 1% nonessential amino acids; 1% penicillin/streptomycin. Specifically, 3.75 x $10^5$ cells were plated in 75 mL L292 medium in a T150 flask (#10-126-34, Thermo Fisher) and incubated for 6 d at 37 ºC and 5% $CO_2$, after which point the supernatant was collected, filtered, and frozen in 50 mL aliquots at -20 ºC for later use in making BMM medium.

### Differentiating Bone Marrow into Macrophages.

Upon plating bone marrow in BMM medium supplemented with 0.1% 5 x $10^{-2}$M βME, cells were incubated at 37 ºC and 5% $CO_2$. After 72 hr, 10 mL fresh BMM medium (without βME) was added to each plate and cells were incubated for an additional 72 hr, after which point the bone marrow cells had differentiated into macrophages (BMDMs). Media was removed from plates and cells—now macrophages—were washed with 1x cold PBS, after which point an additional 1x PBS was added to each plate and cells were incubated at 4 ºC for 30 min. This refrigerated incubation aided in gently detaching macrophages from the plates. After 30 min, macrophages were washed off the plates by repeatedly and gently pipetting the cold PBS over the cell monolayer. The resultant PBS + macrophage mixture was centrifuged for 5 min at 1500 rpm, the supernatant removed, and cells resuspended in BMM medium (without βME) for use in experiments as described below. Alternatively, 1 x $10^7$ cells/mL were suspended in BMM medium with 10% DMSO and stored in liquid nitrogen until later use.

### Infection of BMDMs

BMDMs were obtained as described above and 24 hr prior to infection, 6 x $10^5$ BMDMs were plated in 1 mL BMM medium per well in a 12-well plate. Alternatively, frozen BMDMs were first reconstituted by incubation in 100 x 26 mm Petri dishes in BMM media for 3 days at 37 °C and 5% $CO_2$. After 3 days, 6 x $10^5$ BMDMs were plated onto 12-well plates and grown for 24 hr before use in infection experiments. After 24 hr, media was removed from the wells and cells were washed once with PBS. 400 µL infectious media (comprising EndoU-mut-, DUB-mut-, or WT-MHV virus at MOI = 1.0, aka 6 x $10^5$ pfu per well, in fresh DMEM) was added to BMDMs; alternatively, for mock-infected controls, 400 µL fresh DMEM was added in lieu of inoculum. Wells were infected in quadruplicate for each infection condition in each timepoint (e.g., a total of 16 wells were incubated with infectious medium containing 6 x $10^5$ pfu EndoU-mut-MHV, 4 of which were infected for a total of 3 hr, another 4 of which were infected for a total of 6 hr, etc.). After 1 hr of incubation—tilting the plates every 15 min to ensure even coverage—inocula were removed and 1 mL fresh BMM medium without βME was added to each well. EndoU-mut-, DUB-mut, and WT-MHV-infected cells were then cultured for an additional 2, 5, 8, or 11 hr (for 3, 6, 9, and 12 hr total, respectively), whereas mock-infected cells were only cultured for 3 hr total. After these timepoints, media was removed from wells and 350 µL RLT buffer (79216, Qiagen) was added. BMDMs were scraped off the bottom of the wells and the RLT + BMDM lysate mixtures were frozen at -80 ºC until subsequent RNA isolation.

## RNA Isolation, cDNA Synthesis, and qRT-PCR

### RNA isolation.

Total RNA was isolated from all RLT + BMDM lysate samples—obtained from virus- and mock-infected cells as described above—using an RNeasy Mini Kit (74104, Qiagen) per the manufacturer's instructions. The concentration of isolated RNA per sample was determined using NanoDrop technology. An average of 6,950 ng of total RNA was isolated from each well.

### cDNA Synthesis.

To determine the expression of *Ifna11*, 18S rRNA, and MHV N gene, an equal amount of total isolated RNA (733 ng) was used as the template for cDNA synthesis using an RT$^2$ HT First Strand Kit (330401, Qiagen) per the manufacturer's instructions.

### qRT-PCR.

Upon obtaining cDNA for all samples in this manner, qRT-PCR was performed using specific primers for murine *Ifna11* (PPM03050B-200, Qiagen), murine 18S rRNA (PPM57735E, Qiagen), and MHV N gene (FWD: 5'-AGCAGACTGCAACTACTCAACCCAACTC-3'; REV: 5'-GCAATAGGCACTCCTTGTCCTTCTGCA-3'). RT$^2$ SYBR Green qPCR Mastermix (330502, Qiagen) was used per the manufacturer's instructions in the Bio-Rad CFX96 thermocycler system, in which the qRT-PCR experiments were set up as follows: one step at 95 ºC for 10 min; 40 cycles of 95 ºC for 15 sec each followed by 60 ºC for 1 min and subsequent plate read; one step at 95 ºC for 10 sec; and a melt curve step obtained from 65 to 95 ºC at increments of 0.5 ºC/5 sec. All samples were evaluated in this manner in technical triplicate and the data shown in Figures 11 and 12 are representative of at least 3 independent experiments. The levels of mRNA of the genes of interest (*Ifna11* and N gene) were normalized to the expression of 18S rRNA and reported as fold-change relative to mock- or WT-MHV-infected cells, respectively. Fold induction values were calculated using the $2^{-\Delta\Delta Ct}$ method with the following formula: $2^{-\Delta\Delta Ct}$ [$\Delta C_t = (C_{t(gene\ of\ interest)} - C_{t(18s\ rRNA)})$ ; $\Delta\Delta Ct = (\Delta C_{t(test\ sample)} - \Delta C_{t(calibrator\ group)})$].

## RNA-seq and Subsequent Data Processing, Visualization, and Analysis

### RNA-seq.

At least 12 µL of total RNA at a concentration of at least 100 ng/µL—isolated from EndoU-mut, DUB-mut, WT-MHV-, and mock-infected BMDMs as described above—was submitted to the University of Chicago Genomics Facility (UCGF) for RNA-sequencing. Although BMDMs were initially infected in quadruplicate, only 3 replicate samples from each infection group in each timepoint were submitted for sequencing, for a total of 39 samples (3 mock-infected samples at 3 hpi; 3 EndoU-mut-MHV-infected samples at 3, 6, 9, and 12 hpi; 3 DUB-mut-MHV-infected samples at 3, 6, 9, and 12 hpi; and 3 WT-MHV-infected samples at 3, 6, 9, and 12 hpi). Prior to initiating library preparation, the UCGF first applied quality control analyses to all RNA samples, the results of which are shown in Table 2 in the Results chapter of this document. After passing quality control, samples were subjected to poly-A selection (to enrich mRNAs) and subsequent single-read, 50 bp (SR50) sequencing using Illumina HiSeq 4000 technology. Per our request that an approximately equal number of total reads (~$4.0 \times 10^6$) be generated per sample, approximately $1.6 \times 10^9$ total reads were obtained in this manner across all samples. Raw (unprocessed) reads were downloaded in the form of 7 FASTQ files per sample and were subjected to analysis and processing as described below.

### Processing and Analysis of RNA-seq Data Using Galaxy.

We utilized the public server of an online bioinformatic data manipulation platform called Galaxy (https://usegalaxy.org/) to process and analyze the raw reads obtained from the UCGF in order to derive differential gene expression information from the raw data (Afgan *et al*. 2016). The process by which we analyzed the raw reads using Galaxy is outlined schematically in Figure 13 in the Results chapter. Raw reads (in the form of FASTQ files) were uploaded directly to Galaxy. The sequence and annotation files of the GRCm38 Ensembl build of the C57BL/6J mouse genome were downloaded from Illumina's iGenomes website (https://support.illumina.com/sequencing/ sequencing_software/igenome.html). These files were too large to be uploaded directly to Galaxy and were instead uploaded by way of FileZilla, which is a free FTP client that is readily downloadable from the internet (https://filezilla-project.org/). Once all files were successfully uploaded into Galaxy, we first clipped all FASTQ files to remove any residual unique barcode sequences (the vast majority of which had been removed already by the UCGF prior to making the raw read data available to us) using the "Clip adapter sequences" (Galaxy version 1.0.2) tool. The default options were kept, with the exception of the following: "discard sequences with unknown (N) bases" was changed to "no;" and "output options" was changed to "output both clipped and non-clipped sequences" to ensure that reads that had already been clipped by the UCGF were not eliminated from the outputs. Once clipped, FASTQ files were then concatenated (combined) such that a single FASTQ file pertained to each sample. This was achieved using the "Concatenate datasets tail-to-head (cat)" (Galaxy version 0.1.0) tool. There were no changeable parameters associated with this tool. Next, concatenated files were "groomed" using the "FASTQ Groomer" (Galaxy version 1.1.1) tool to ensure that all reads were in the appropriate Sanger FASTQ format (all files and reads should have already been in FASTQ format upon receipt from the UCGF, such that this step was merely an opportunity for us to double-check the format of the data that we had downloaded from the UCGF). No defaults were changed at this step. After grooming, all files were appropriately clipped, combined, and in the required FASTQ format.

We next sought to align the reads in all samples to the mouse genome. Notably, all virus-infected samples were expected to contain reads that originated from mouse RNA *and* reads that originated from viral RNA, since both species of RNA would have been present in the original samples that we submitted for sequencing. As such, we performed two alignment steps, the first of which was intended to weed out any non-murine (i.e., viral) reads in order to reduce file sizes since the public domain of Galaxy only allows for a relatively small amount of data storage at one time. Thus, we first aligned all reads to the mouse genome using the "HISAT2" (Galaxy version 2.1.0) alignment tool (Kim *et al*. 2015). Instead of using a built-in genome, we used the version of the C57BL/6J sequence that we previously uploaded into Galaxy. Other default options were left unchanged with the following exception: under "Advanced Options > Output options" the option to "write aligned reads (in fastq format) to separate file(s)" was changed to "yes" since we wanted to keep only those reads that corresponded to the murine genome. After obtaining aligned (i.e., murine-only) reads as an output from this first alignment step in the form of a FASTQ file, those reads were again submitted to HISAT2 to obtain the alignment information in the form of a single BAM file for each sample. For this second alignment step, default options were left unchanged except that we again used the C57BL/6J sequence as a reference genome instead of a built-in genome.

After removing non-murine reads from all samples and aligning the remaining murine-only reads to the mouse genome, we next counted the number of reads that pertained to each annotated gene in the genome using the “featureCounts” (Galaxy version 1.6.0.6) tool (Liao *et al*. 2014). Using as inputs into featureCounts the BAM files that were generated as a result of the second HISAT2 alignment step, we did not change any default options except for the following: “gene annotation file” was changed to “in your history” in order to utilize the annotation file for the C57BL/6J genome that we previously uploaded into Galaxy. After applying featureCounts in this manner to the single BAM file associated with each sample, the final step we employed was to determine differential gene expression using “DESeq2” (Galaxy version 2.11.40.2) (Love *et al*. 2014). Using as inputs into DESeq2 the tabular outputs that were generated as a result of the featureCounts step, we ran DESeq2 separately for each timepoint (3, 6, 9, and 12 hpi). We specified the factor name as “Virus_Infection” and 4 factor levels for each timepoint as “Mock,” “WT,” “EndoU-mut,” and “DUB-mut” and uploaded the appropriate tabular files from featureCounts into each factor level (i.e., the tabular files associated with EndoU-mut-MHV-infected BMDMs—in triplicate—were uploaded into the respective timepoint, and so on). Note that the same 3 tabular files associated with mock-infected cells at 3 hpi (in triplicate) were used in the DESeq2 analysis of all 4 timepoints. The following options were changed from their defaults: “output normalized counts table” was changed to “yes;” and “output all levels vs all levels of primary factor” was changed to “yes.” Using these parameters, DESeq2 generated as outputs 7 total files for each timepoint: 6 tabular files containing the differential expression analyses for each gene in the mouse genome each containing a different comparison (Mock vs WT, Mock vs DUB-mut, Mock vs EndoU-mut, DUB-mut vs WT, EndoU-mut vs WT, and DUB-mut vs EndoU-mut) and a 7th tabular file containing the normalized count information for all genes across all replicate samples. Importantly, these DESeq2-generated “normalized” counts are distinct from the “raw” counts from which they were derived. In order to account for differences in sequencing depths between libraries (aka samples), DESeq2 automatically normalizes raw count data to scale up or down those counts for each gene according to the number of *total* counts in each sample relative to the others. This process of normalization is described in depth by Love *et al*. (2014). The normalization of raw reads was particularly important for our datasets since our mock-infected samples contained a substantially larger number of total murine reads than did virus-infected samples (especially as the infection developed over time, as transcription of the viral genome begins to overwhelm expression of host genes as infection progresses). These normalized counts are then used by DESeq2 to calculate differential expression in the form of fold-change; we also used these normalized count values to generate Figures 14, 16-19, and 21 in the Results and Discussion chapters of this document.

### Method for Independent Confirmation of DESeq2-generated Normalized Counts.

We sought to independently confirm that the process by which DESeq2 produces normalized reads from raw counts did not inappropriately skew our data. Therefore, in addition to creating Figures 14 and 16-19 using the DESeq2-generated normalized counts for each timepoint, we utilized the *raw* count data (which was produced as the output of the featureCounts tool) to generate similar heatmaps and line graphs. If the normalized counts were appropriately derived from the raw counts without skewing the data, then the general patterns displayed in a heatmap produced using normalized counts should be visually similar to one produced using the values obtained by dividing the number of raw counts for each gene by the total number of raw reads in each sample. The same should also be true of line graphs constructed using the two different kinds of count data. Indeed, as shown in Figure 10 below, that is what we found. Figure 10A shows two heatmaps containing the gene expression data for only the 12 hpi timepoint (using the same gene list as in Figure 14 in the Results chapter of this document) in the form of either row z-score-standardized *normalized* counts or row z-score-standardized *raw* counts. Notably, the colors (and therefore the row z-scores) are often not the same for each gene between the two heatmaps, which is not unexpected given that the actual values of the normalized and raw gene counts divided by the total raw counts are not the same; however, the overall patterns of differential gene expression are conserved between the two heatmaps. Similarly, Figure 10B displays line graphs for 3 different genes—*Ifna11*, *Ifih1*, and *Csf1*—using either raw reads for each gene divided by the total number of raw reads in each sample or DESeq2-generated normalized reads. These line graphs, like the heatmaps, demonstrate that the overall patterns of gene expression observed between samples over time were conserved regardless of which type of count data is used. Thus, having confirmed the validity of the DESeq2-generated normalized counts by an independent means of data analysis and presentation, we were confident that the normalized count data were appropriate for use in our analyses shown in multiple figures and tables in the Results chapter.

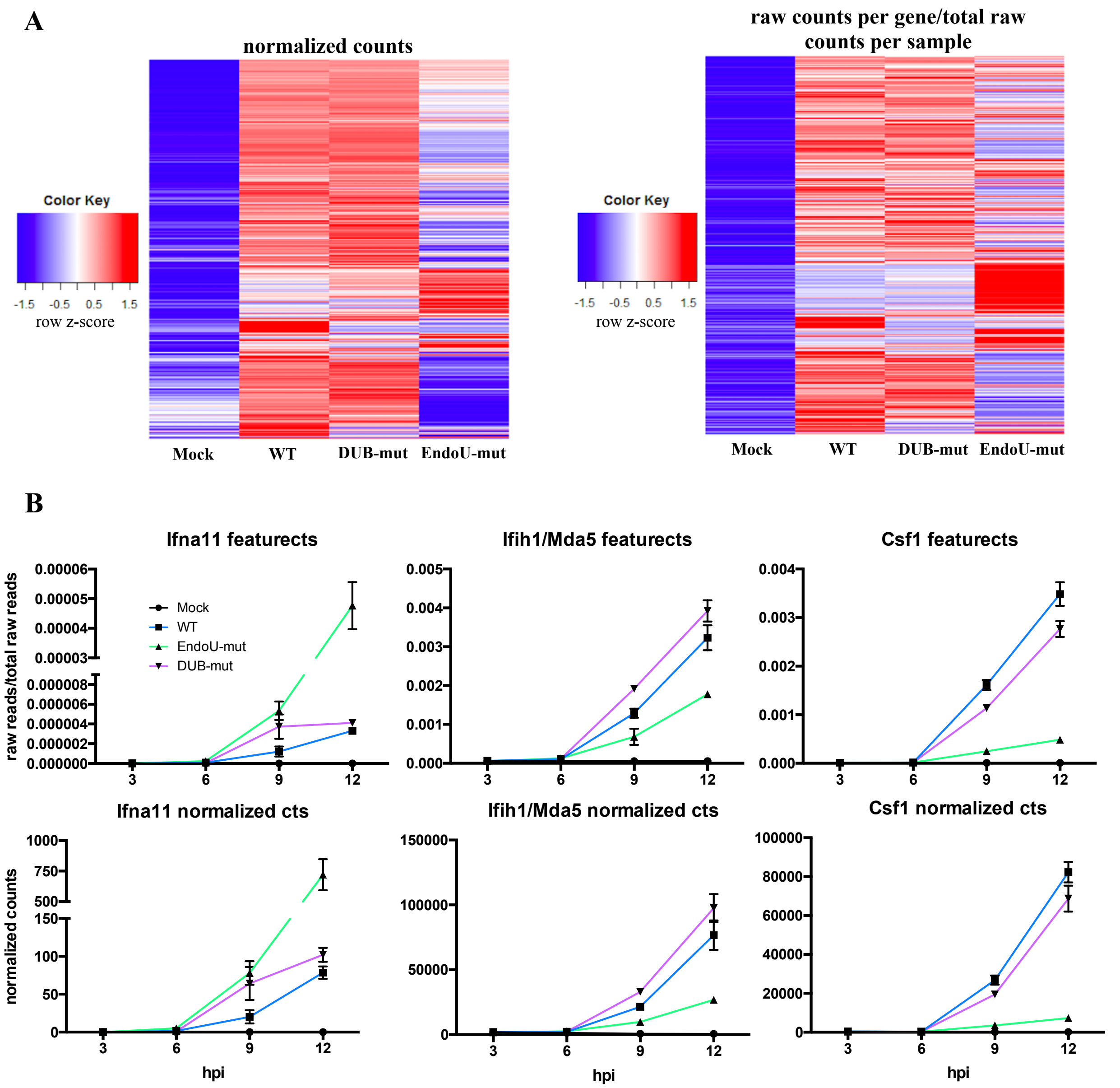

**Figure 10. Method for Independent Confirmation of DESeq2-generated Normalized Counts.** (A) Heatmaps showing gene expression data for the same 2,879 genes as in Figure 14 at 12 hpi only. On the left, DESeq2-generated normalized counts were plotted as row z-scores; on the right, raw counts for each gene were divided by the total number of raw counts in each sample and the resulting values were plotted as row z-scores. Color keys indicate the colors that correspond to each z-score value, with warmer colors indicating higher relative expression in each row and cooler colors corresponding to lower relative expression. (B) Line graphs showing gene expression data as non-z-score-standardized counts over time for 3 genes. The graphs in the top row were produced by plotting the values that were obtained by dividing the raw read counts for each gene by the total number of raw reads in each sample (as determined from data analysis using featureCounts). The graphs in the bottom row display DESeq2-generated normalized counts for the same 3 genes. Data are presented as means ± SD.

### Selecting the Most Highly Differentially-expressed Genes.

After obtaining differential expression data for all genes across all samples and timepoints using Galaxy, we next generated a list of the most highly upregulated genes that we would use in subsequent analyses. To do this, we analyzed the differential expression data—generated as an output of DESeq2 analysis—between WT-MHV-infected BMDMs at 12 hpi and mock-infected cells and selected only those genes whose differential upregulation in WT-MHV-infected cells (as determined by DESeq2) was statistically significant by eliminating genes associated with a q-value (adjusted p-value, calculated by DESeq2 using the Benjamini-Hochberg procedure) of > 0.05 (Love *et al.* 2014). We applied an additional parameter using a fold-change magnitude cutoff, such that genes that were not differentially upregulated by at least 4-fold (aka a $\log_2$ fold-change value > 2) in WT-MHV-infected- compared with mock-infected BMDMs were excluded. After applying these cutoffs, 2,879 genes remained.

### Visualizing Gene Expression Data.

Upon identifying the top 2,879 genes that were most differentially expressed between WT-MHV-infected- and mock-infected BMDMs, we next sought to visualize the expression data for these genes in heatmap form. To do this, we averaged the normalized counts for each of the 2,879 genes—obtained from DESeq2 as described above—from the triplicates, ordered the list of genes from most- to least-highly differentially expressed between WT-MHV-infected- and mock-infected BMDMs, and imported the z-score-standardized $\log_2$-trasformed mean normalized count values into Cluster 3.0 software. Cluster 3.0 allows for hierarchical arrangement of gene lists using expression data by clustering together genes whose expression patterns are similar to each other (de Hoon *et al.* 2004). Specifically, we used the default settings—the similarity metric “Pearson correlation (uncentered)” and the clustering method "centroid linkage"—in order to mathematically arrange the genes based on expression similarities. Note that this is *not* the same as functional clustering/arrangement in that Cluster 3.0 only utilizes expression data, and not gene-encoded functional information, in order to hierarchically arrange genes. In order to visualize the result of this clustering, the output file of Cluster 3.0 processing was imported into Java TreeView software, which generates heatmaps from Cluster 3.0 outputs (Saldanha 2004). The outcome of this clustering and visualization process is shown as a heatmap in Figure 14 in the Results chapter. By studying this heatmap, we identified 6 groups of genes—which had been arranged as such by Cluster 3.0—whose gene expression profiles between infection cohorts and over time warranted additional analysis. We used Java TreeView to extract the list of gene names that corresponded to each of these 6 groups, which are indicated with brackets in the heatmap in Figure 14.

## Functional Clustering Analyses Using DAVID

In order to determine the general biological functions of the differentially-expressed genes identified from our experiments that are shown in Figure 14, we utilized DAVID (Database for Annotation, Visualization and Integrated Discovery; https://david.ncifcrf.gov/gene2gene.jsp), which is a free online tool that allows for functional clustering (aka gene ontology) analyses of lists of genes (Huang *et al*. 2009a; Huang *et al*. 2009b). We submitted the list of gene names (obtained from Java TreeView) from each of the 6 groups indicated in Figure 14 to DAVID and converted the gene names to Ensembl IDs, the latter of which are better suited for DAVID analyses. Not all genes corresponded to an Ensembl ID, which is not surprising given that many of the genes within the heatmap in Figure 14 are putative and/or have not yet been assigned any function. The lists of Ensembl IDs—one list per each of the 6 groups—were then submitted to DAVID for functional clustering analyses. Specifically, under the "Gene

Ontology" category, the chart associated with the "GOTERM_BP_DIRECT" result (which is always conspicuously highlighted in red, as it is one of the DAVID-defined defaults) was used for all 6 groups.

For each term in its output (a term corresponds to a functional cluster into which a given number of one's input genes were clustered by DAVID), DAVID assigns a q-value that is determined based on the relative enrichment profiles of the genes from one's input list of genes. For example, whether or not a list of input genes contains a statistically significant overrepresentation of "immune response" genes will be reflected in the q-value associated with the "immune response" term in the DAVID results page. Using these q-values, we excluded all functional cluster terms that were not statistically significant using a cutoff of $q < 0.05$. We then further organized the remaining terms into even fewer clusters based on general relationships between terms (i.e., "immune response," "inflammation," and other semantically similar DAVID-generated terms were organized together under the blanket term "immune response"). By creating a "sublist" in DAVID that included only the statistically significant functional clusters within each of the 6 groups, we determined the number of unique genes within each group that appeared in at least one functional cluster of statistical significance. The row z-score-standardized $\log_2$-transformed normalized counts for these "unique genes in statistically significant functional clusters" were then plotted over time in heatmaps using the gplots package in RStudio, a free downloadable package and program, respectively, that together allow for the visualization and manipulation of data in various forms (RStudio Team 2015; Warnes *et al.* 2016).

# CHAPTER III

# RESULTS

## Evaluating Expression of Type I IFN in BMDMs during Infection with EndoU-mut-, DUB-mut-, and WT-MHV

Given the data from our lab and other groups demonstrating that nsp15-EndoU and nsp3-DUB contain type I IFN antagonism activity, mutant viruses encoding catalytically deficient (EndoU-mut) or catalytically impaired (DUB-mut) versions of these proteins, shown in Figure 7, should elicit greater IFN responses during infection compared to the WT parental strain (Clementz *et al*. 2010; Mielech, Kilianski, *et al*. 2014; Deng *et al*. 2017; Kindler *et al*. 2017; Deng *et al*. manuscript in preparation). Indeed, published and unpublished data in which each mutant virus was used in separate experiments demonstrated that both EndoU-mut- and DUB-mut-MHV-infected cells exhibited enhanced IFN production during infection relative to WT-MHV infection (Deng *et al*. 2017; Kindler *et al*. 2017; Deng *et al*. manuscript in preparation). Importantly, however, the effects on the IFN response that are elicited by the two mutant strains have not been directly compared. Thus, we first evaluated the expression of type I IFN in the context of a timecourse infection with these 3 different viruses. Briefly, BMDMs were infected with WT-, EndoU-mut-, or DUB-mut-MHV (MOI = 1.0) for 3, 6, 9, or 12 hr, after which timepoints total RNA was collected for subsequent analysis by quantitative reverse transcription polymerase chain reaction (qRT-PCR) (see Materials and Methods for primer information). RNA was also collected from mock-infected cells at 3 hpi and was used as a negative control for analyses of all timepoints. In Figure 11, the expression of *Ifna11* is reported as fold-change relative to mock-infected cells (using the $2^{-\Delta\Delta Ct}$ method) and is normalized to the expression of 18S ribosomal RNA (18S rRNA) as an internal control. Statistical significance between infection groups was determined using two-tailed Student's t-tests.

We found that BMDMs infected with either mutant virus expressed significantly higher ($p < 0.05$) amounts of a type I IFN—*Ifna11*— compared to BMDMs infected with WT-MHV at 6, 9, and 12 hpi. No significant difference was found between groups at 3 hpi. Notably, while cells infected with either mutant virus exhibited significantly earlier and more robust IFN expression compared to WT-infected cells, these effects were most potent in the EndoU-mut-infected groups at all timepoints (except 3 hpi). Thus, in addition to demonstrating the impaired ability of EndoU-mut- and DUB-mut-MHV to suppress IFN expression during infection, these experiments provided an initial indication that both mutant viruses being studied (Endo-mut- and DUB-mut-MHV), although similar in that each encodes a catalytically-deficient or impaired viral IFN antagonist, elicit distinct host responses during infection.

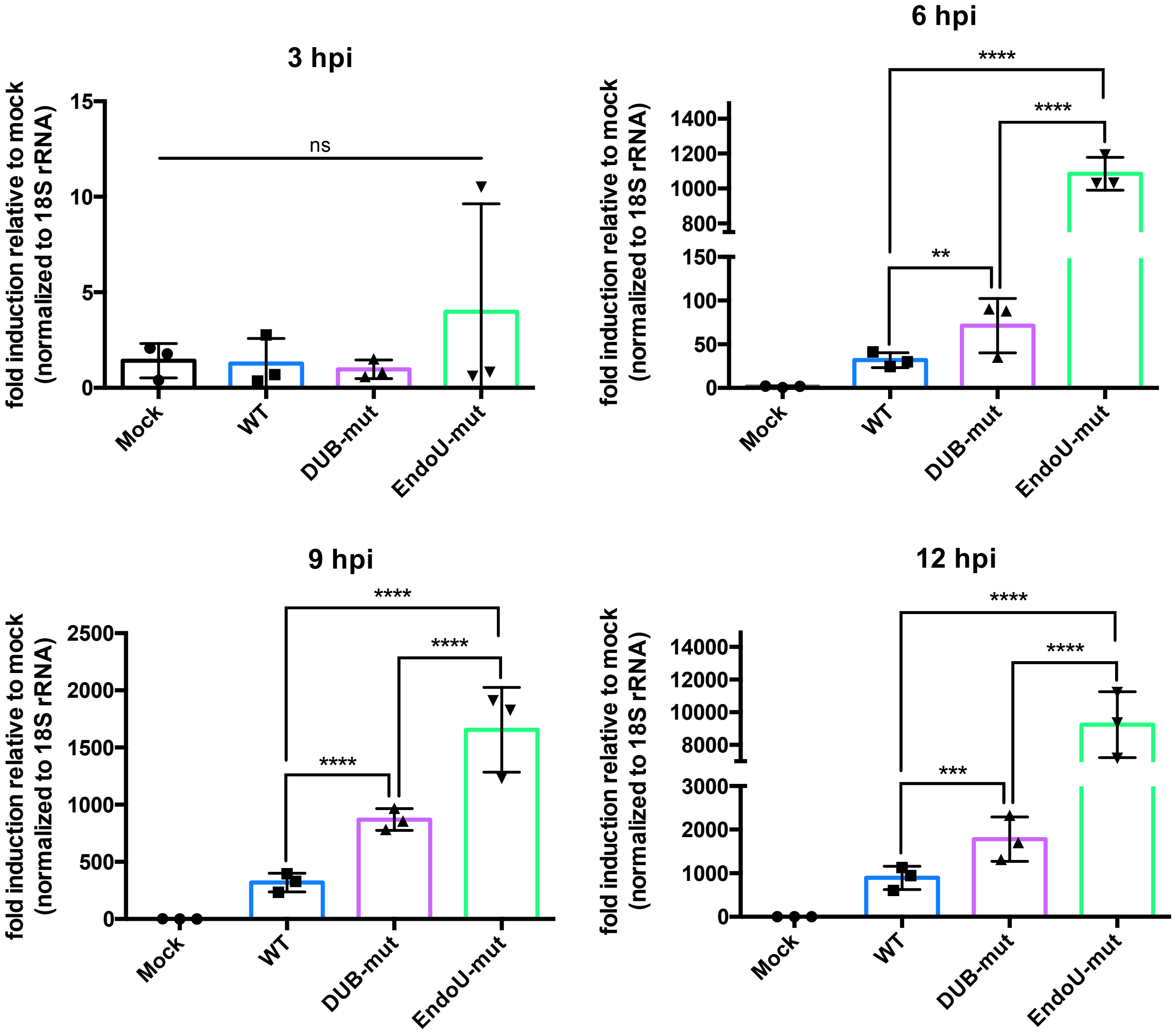

**Figure 11. EndoU-mut- and DUB-mut-MHV Induce Significantly Higher Expression of *Ifna11* during Infection of BMDMs.** BMDMs were infected with EndoU-mut, DUB-mut, and WT-MHV at MOI = 1.0. Cells were lysed and total RNA was extracted at 3, 6, 9, and 12 hpi. RNA from mock-infected cells at 3 hpi was included in analyses of all timepoints as a negative control. Total RNA from each sample was converted to cDNA, which was then evaluated for expression of *Ifna11* and 18S rRNA, the latter of which served as an internal control. Expression of *Ifna11* is reported as fold-change relative to mock-infected cells (normalized to 18S rRNA expression) and was calculated *via* the $2^{-\Delta\Delta Ct}$ method using the following equation: $2^{-[(Ct(Ifna11) - Ct(18S\ rRNA))test\ sample - (Ct(Ifna11) - Ct(18S\ rRNA))mock\ group]}$. Statistical significance between infection groups within each timepoint was determined using two-tailed Student's t-tests. ** $p < 0.01$; *** $p < 0.001$; **** $p < 0.0001$; ns, not significant. Data are presented as means ± SD.

## Evaluating Expression of Nucleocapsid Gene in BMDMs during Infection with EndoU-mut-, DUB-mut-, and WT-MHV

To determine if the mutant viruses exhibited any differences in viral gene expression, we evaluated the expression of nucleocapsid (N) gene in the context of a timecourse infection with these different viruses (Figure 12). Evaluating the levels of N gene transcript over time is a method of indirectly assessing CoV replication kinetics since N gene mRNA levels increase as wild type viral infection progresses and nucleocapsid protein is essential for the packaging of coronaviral genetic material into assembling virions (*Irigoyen et al. 2016; Kuo et al*. 2016). The same RNA samples from the experiment described in Figure 11 were also used to evaluate N gene expression by qRT-PCR. In Figure 12, the expression of N gene is reported as fold-change relative to WT-MHV-infected cells (since there was no detectable expression of N gene in mock-infected samples) and is normalized to the expression of 18S rRNA. Fold induction was calculated using the following equation: $2^{-[\mathrm{Ct(N\ gene)} - \mathrm{Ct(18S\ rRNA)}]}$. Statistical significance between infection groups was determined using two-tailed Student's t-tests.

We found no significant difference between relative expression levels of N gene in WT- and DUB-mut-MHV-infected BMDMs at any timepoint, indicating that the IFN induction observed in the context of DUB-mut-MHV infection (Figure 11) was not sufficient to interfere with replication of DUB-mut-MHV. In contrast, levels of N gene transcript were significantly lower in EndoU-mut-MHV-infected BMDMs than in WT- or DUB-mut-MHV-infected cells at 6, 9, and 12 hpi. Notably, the timing of this decreased N gene expression in EndoU-mut-MHV-infected BMDMs inversely mirrored the timing of the *Ifna11* expression profile that was elicited during infection with the EndoU-mut virus (Figure 11). This relationship suggests that the inability of mutant EndoU to antagonize the IFN response during infection contributed to the observed attenuated expression of N gene during infection of WT-BMDMs with EndoU-mut-MHV. No significant difference in the expression of N gene between infection groups was observed at 3 hpi.

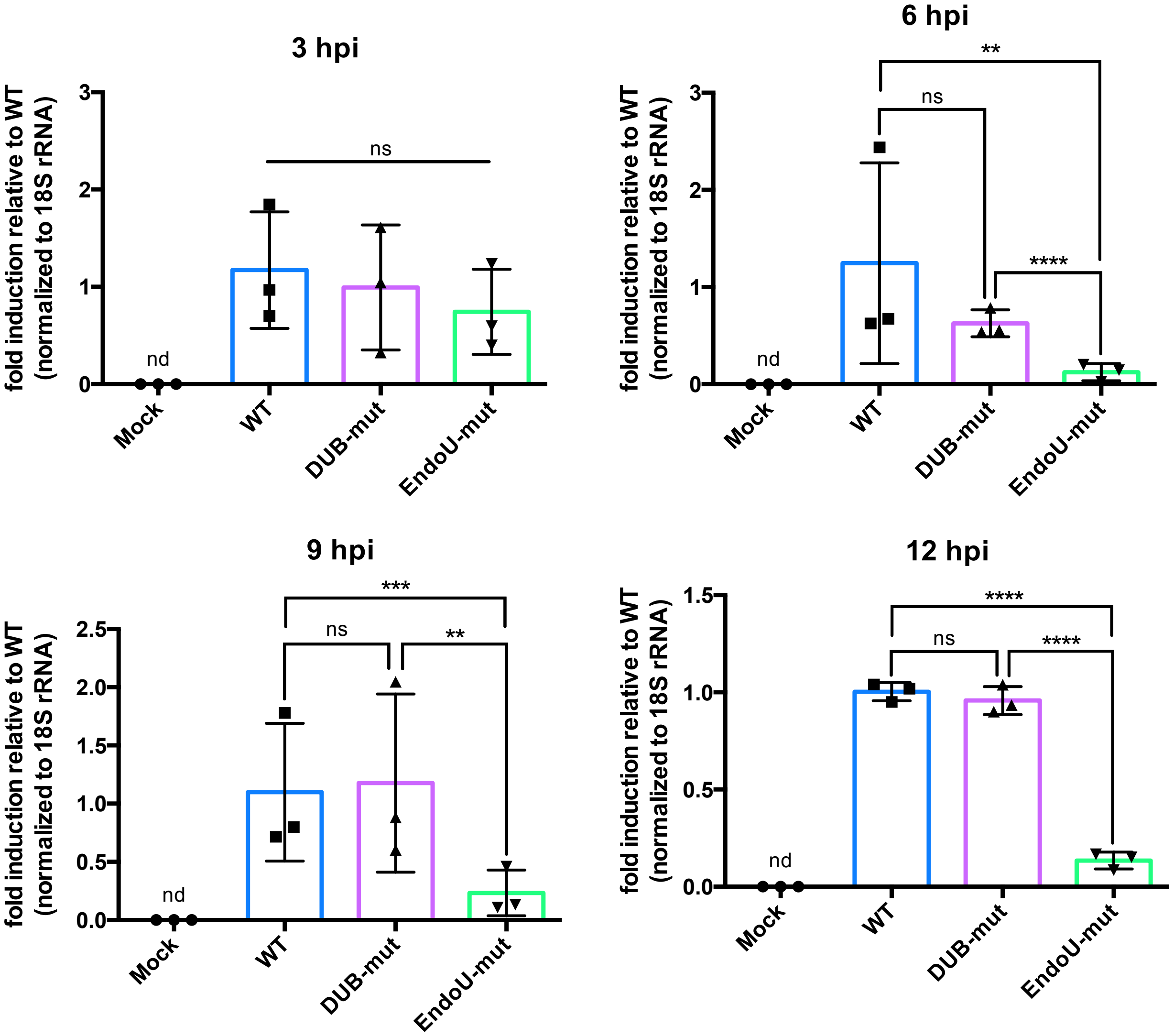

**Figure 12. Expression of Viral Nucleocapsid Gene is Attenuated during Infection of BMDMs with EndoU-mut- but not DUB-mut-MHV.** BMDMs were infected and RNA was collected for qRT-PCR as described in Figure 11. Expression of viral nucleocapsid (N) gene is reported as fold-change relative to WT-MHV-infected cells (normalized to 18S rRNA expression) and was calculated *via* the $2^{-\Delta\Delta Ct}$ method using the following equation: $2^{-[(Ct(Ifna11) - Ct(18S\ rRNA))test\ sample - (Ct(Ifna11) - Ct(18S\ rRNA))WT\ group]}$. Statistical significance between infection groups within each timepoint was determined using two-tailed Student's t-tests. ** $p < 0.01$; *** $p < 0.001$; **** $p < 0.0001$; ns, not significant; nd, not detected. Data are presented as means ± SD.

Taken together, the qRT-PCR timecourse experiments in Figures 11 and 12 demonstrate that EndoU-mut- and DUB-mut-MHV triggered an earlier and more robust type I IFN response in WT-BMDMs compared to WT-MHV, indicating that the wild type versions of EndoU and DUB proteins both function as IFN antagonists. Additionally, the observed differences in the expression of *Ifna11* and N gene between EndoU-mut- and DUB-mut-MHV suggest that the endoribonuclease activity of nsp15 is a more potent suppressor of the IFN response than the deubiquitinase activity of nsp3, given that a catalytic mutation in nsp15-EndoU dramatically impaired the expression of at least one viral gene, while a catalytically impaired nsp3-DUB exhibited WT-like viral gene expression kinetics. These results provided rationale for subsequent RNA-seq experiments, the goal of which was to determine the global transcriptional effects—with particular interest in the transcription of genes whose protein products are involved in innate antiviral immunity—that are elicited during infection with these different strains of MHV.

## Global Gene Expression Induced by EndoU-mut-, DUB-mut-, and WT-MHV in BMDMs

To obtain a comprehensive, global view of how WT-, EndoU-mut-, and DUB-mut-MHV shape the antiviral innate immune response during infection, RNA-seq was applied to RNA samples from virus-infected BMDMs at multiple timepoints. Specifically, BMDMs were infected with WT-, EndoU-mut-, or DUB-mut-MHV (MOI = 1.0) in quadruplicate and total RNA was isolated from whole cell lysates at 3, 6, 9, and 12 hpi. As above, RNA was also collected from mock-infected cells at 3 hpi to be used as a negative control for analyses of all timepoints. RNA samples—which included both host and viral RNAs—were then submitted in triplicate to the University of Chicago Genomics Facility, where samples first underwent poly-A selection to separate mRNAs from rRNAs. Total mRNA from each sample was then subjected to quality control (QC) analysis by Bioanalyzer technology. Results of QC tests on all samples are reported as RNA integrity numbers (RINs) in Table 2, with a maximum RIN value of 10 corresponding to the highest obtainable RNA quality (Schroeder *et al*. 2006). All samples were of sufficient quality for RNA-seq; however, we note that the RNA from each of the EndoU-mut-MHV-infected replicates at 12 hpi were of lower quality than all other groups, possibly indicating that BMDMs infected with EndoU-mut-MHV—but not DUB-mut- or WT-MHV—endured some level of RNA degradation by 12 hpi. After passing quality control, cDNA libraries were generated from total mRNA from each sample and libraries were subsequently subjected to next-generation single-read 50 base pair (SR50) sequencing by Illumina technology. Approximately 4 x $10^7$ total reads—which, in virus-infected samples, included reads of both host and viral origin—were generated from each sample (3 replicates per infection condition per timepoint) for a total of approximately 1.6 x $10^9$ reads across all samples from all timepoints.

| | | RIN Value | | |
|---|---|---|---|---|
| | | *Replicate 1* | *Replicate 2* | *Replicate 3* |
| **3 hpi** | Mock | 10 | 10 | 10 |
| | WT | 10 | 10 | 10 |
| | DUB-mut | 10 | 10 | 9.5 |
| | EndoU-mut | 10 | 10 | 10 |
| **6 hpi** | WT | 10 | 10 | 10 |
| | DUB-mut | 10 | 10 | 10 |
| | EndoU-mut | 10 | 10 | 10 |
| **9 hpi** | WT | 10 | 10 | 10 |
| | DUB-mut | 10 | 10 | 10 |
| | EndoU-mut | 9.8 | 9.9 | 9.6 |
| **12 hpi** | WT | 10 | 8.2 | 10 |
| | DUB-mut | 10 | 10 | 10 |
| | EndoU-mut | 8.5 | 8.4 | 8.2 |

**Table 2. RIN Values of Samples Submitted for RNA-seq.** Prior to applying RNA-seq to submitted samples, QC analyses were performed using Bioanalyzer technology to determine the quality of the RNA in each sample. Shown are the results of these QC analyses, reported as RIN values that are a relative indication of RNA quality, for each of the 3 replicates for each infection group across all 4 timepoints. A value of 10 represents the highest quality RNA.

To extract biologically-relevant information from the sequencing information that was generated from each RNA sample, the total reads were then analyzed using an established RNA-seq bioinformatic analysis pipeline through an online platform called Galaxy (Afgan *et al*. 2016). This pipeline is outlined schematically in Figure 13 (see Materials and Methods for an in-depth explanation of each step). Briefly, residual barcode sequences—unique to each sample—were clipped from all reads and clipped reads originating from the same sample were then concatenated into a single file per sample. Next, each concatenated file containing clipped reads was "groomed" to ensure that all reads were in the appropriate Sanger FASTQ format that is required for downstream analyses. Groomed reads were then aligned to the C57BL/6J murine genome using the tool HISAT2 (Kim *et al*. 2015). The sequence and annotation files of the GRCm38 Ensembl build of the mouse genome were downloaded from Illumina's iGenomes website. After using HISAT2, all reads that did not successfully align to the reference genome were discarded; for virus-infected samples, this step was important to eliminate those reads that originated from viral mRNAs. The reads in each sample that aligned with the sequence of an annotated gene in the reference genome were then counted by featureCounts and those "raw" counts were used along with the tool DESeq2 to calculate differential expression values for each gene between each of the 4 treatment groups (WT-MHV-, EndoU-mut-MHV-, DUB-mut-MHV-, and mock-infected BMDMs) (Liao *et al*. 2014; Love *et al*. 2014). Importantly, DESeq2 transforms "raw" counts for each gene in each sample into "normalized" count values, the latter of which it then uses to calculate fold-change in expression between groups. Raw count values are normalized by DESeq2 to take into account size differences between samples; for example, if $2 \times 10^6$ reads from one sample aligned to the reference genome, but $3 \times 10^6$ reads from another sample aligned to the same genome, then DESeq2 takes those differences into account by scaling the raw reads for a given gene across all compared samples (Love *et al*. 2014).

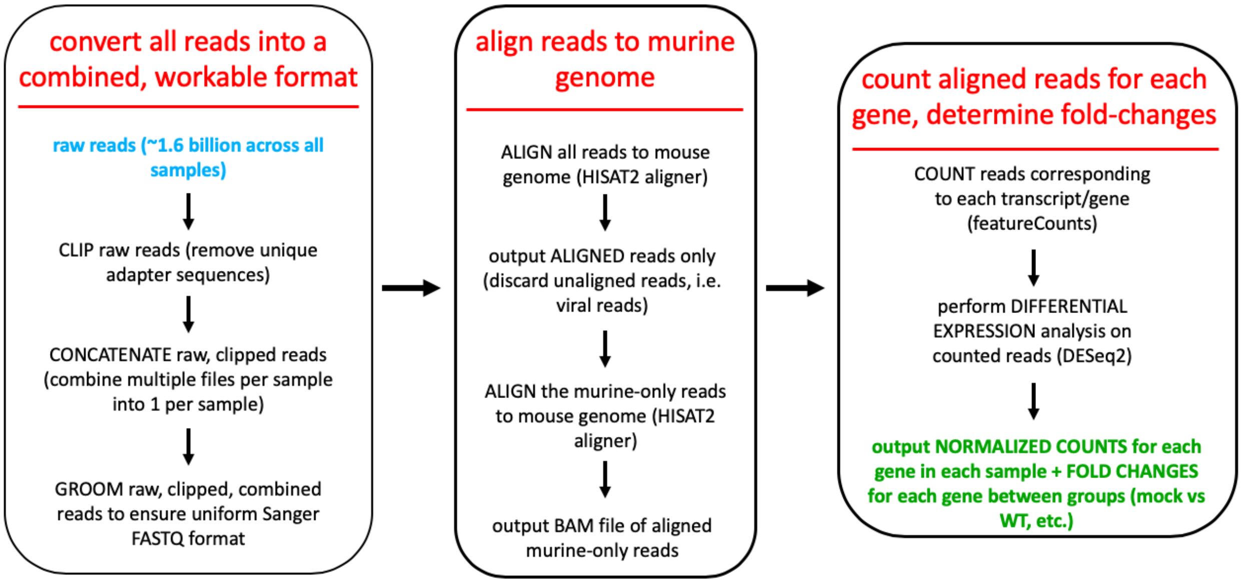

**Figure 13. RNA-seq Data Analysis Pipeline.** Raw RNA-seq data in the form of reads (strings of nucleotide sequences) were processed using Galaxy's online platform in order to generate differential gene expression data between infection groups. Reads were first clipped to remove any residual unique barcode sequences that were originally added during preparation of each RNA sample for sequencing. Reads were then concatenated to combine multiple files per sample into a single file for each sample. Combined files were then groomed to ensure that all reads were in Sanger FASTQ format. Next, reads were aligned to the GRCm38 Ensembl build of the C57BL/6J mouse genome using HISAT2 aligner, which locates the region of the genome to which each read corresponds. Because most samples contained both viral and mouse RNA, the first alignment step was used to weed out all reads that did not correspond to any location along the mouse genome. All reads not aligning to the mouse genome (i.e., reads that originated from viral RNA) were discarded to reduce file sizes. The remaining murine-only reads were re-aligned to the mouse genome to obtain an output BAM file for each sample. BAM files contained the alignment information for each read in that sample and were used as inputs into featureCounts, which counts the number of reads in each sample that corresponds to each gene in the mouse genome. Finally, the outputted count data from featureCounts was used as the input for DESeq2 to calculate differential expression for each gene across all samples and treatment groups. In addition to differential gene expression and fold-change data, DESeq2 generated normalized count values for each gene in all samples. These normalized counts are intended to correct for size differences between samples that might otherwise skew differential expression calculations if some samples contain substantially more or fewer total reads than the others. These values are plotted and visualized in a variety of ways, as shown in Figures 14, 16-19, and 21.

After applying this pipeline to our raw reads and obtaining as an output expression information for each gene across all samples, we next sought to identify and analyze differentially-expressed genes (DEGs) between infection groups. We used as a starting point the list of DEGs between mock and WT-MHV-infected BMDMs at 12 hpi that was generated as an output by DESeq2. We filtered this list of genes based on the statistical significance associated with the fold-change differential expression value. A q-value (aka adjusted p-value, calculated by DESeq2 for each gene in each comparison using the Benjamini-Hochberg procedure) of $< 0.05$ was chosen as the cutoff for statistical significance; genes whose differential upregulation values did not meet this cutoff in WT-MHV-infected BMDMs at 12 hpi compared with mock-infected cells were removed from the list (Love *et al*. 2014). Next, a differential expression magnitude cutoff of $> 4$ was applied to the remaining genes; genes that were not more highly expressed by at least 4-fold in WT-MHV-infected cells at 12 hpi compared to mock were removed from the list. After applying these cutoffs, 2,879 genes remained and were arranged in order of most- to least-highly upregulated in WT-MHV-infected cells at 12 hpi compared to mock. Cluster 3.0 software was then used to apply mathematical clustering to the z-score-standardized $\log_2$-normalized mean normalized count values associated with each gene in each timepoint and infection group (de Hoon *et al*. 2004). Specifically, the default settings—the similarity metric "Pearson correlation (uncentered)," and the clustering method "centroid linkage"—were applied to the list of 2,879 genes and the corresponding expression values for each gene across all samples to produce a hierarchically-clustered gene list based on how similar or different the expression patterns were between groups of genes across all samples. This new list of clustered genes and their associated expression values was then visualized as a heatmap using Java TreeView software, which is shown in Figure 14 (Saldanha 2004). Figure 14 depicts global differences in gene expression between WT-, EndoU-mut-, and DUB-mut-MHV-infected BMDMs. Plotted are row z-score-standardized $\log_2$-transformed normalized counts for each of the 2,879 different murine genes across all timepoints and infection groups. The normalized counts represent the average of the replicates for a given timepoint and infection group. The names of all 2,879 genes in Figure 14 are listed, in the same order in which they are clustered in the heatmap, in Table S1 in the Appendix of this document.

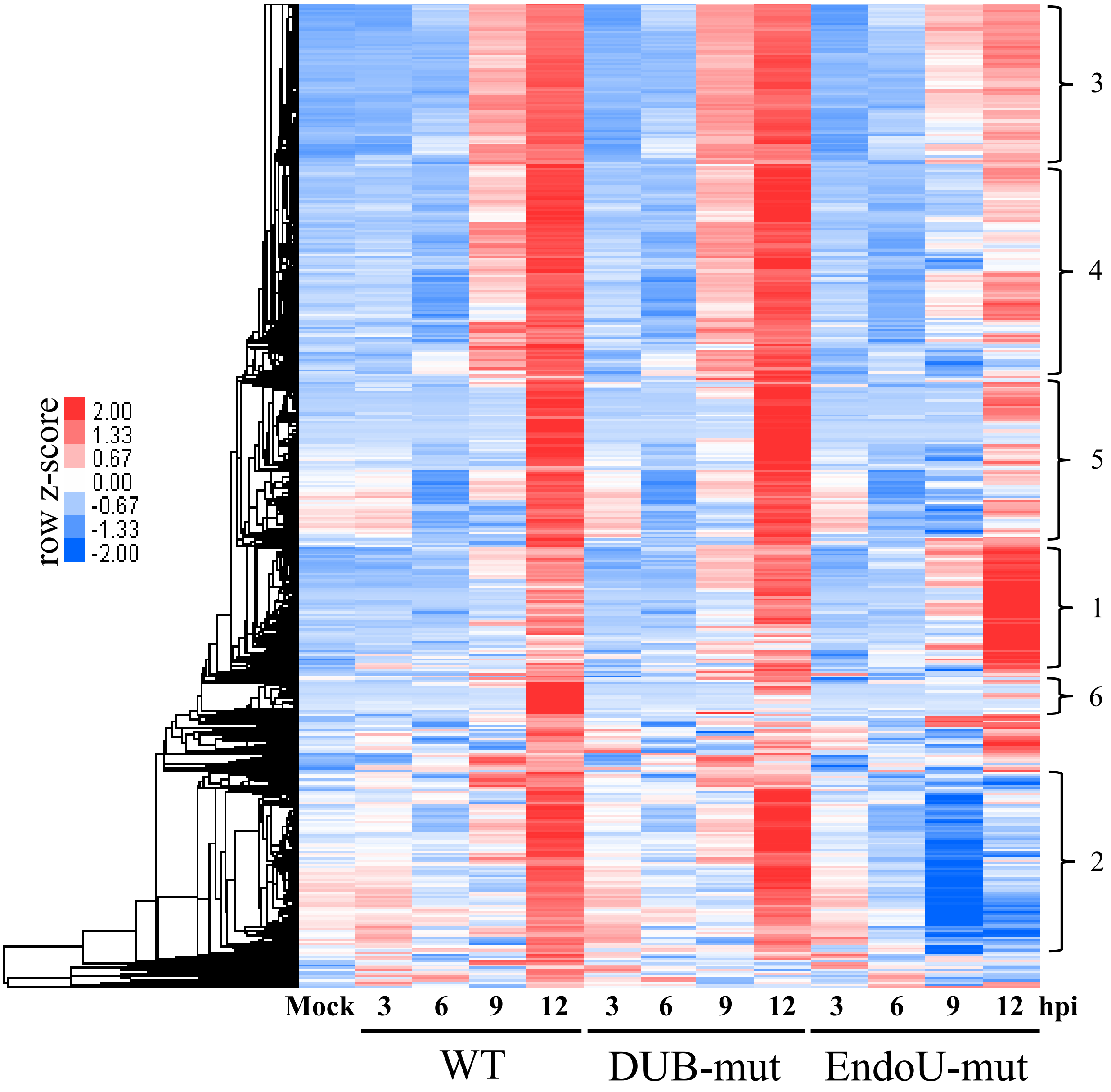

**Figure 14. Global Expression Profiles of EndoU-mut-, DUB-mut-, WT-MHV, and Mock-infected BMDMs.** Total RNA was extracted from EndoU-mut-, DUB-mut-, and WT-MHV-infected BMDMs at 3, 6, 9, and 12 hpi. Samples were poly-A-selected to enrich mRNAs (without eliminating viral RNAs, which resemble host mRNAs) and subjected to SR50 sequencing by Illumina technology. Raw reads were processed as described in Figure 13 to generate differential expression data and normalized counts for each gene in each sample. Next, the expression data from WT-MHV-infected BMDMs at 12 hpi was compared with mock-infected cells; a statistical significance cutoff of $q < 0.05$ and a fold-change cutoff of $> 4$ were

applied to select only the most highly differentially-expressed genes. The normalized counts for the 2,879 genes that met these cutoffs were averaged across replicates and converted to $\log_2$-transformed z-scores, which were then imported into Cluster 3.0 software to mathematically arrange the gene list based on similarity in expression patterns between samples *via* the Pearson correlation (uncentered) and centroid linkage metrics. Finally, Java TreeView software was used to visualize the output from Cluster 3.0, the outcome of which is shown here. Plotted are row z-score-standardized $\log_2$-transformed values for each gene across all samples and timepoints. The color bar indicates the approximate row z-score that is associated with each color, with warmer colors corresponding to higher relative expression values in each row and cooler colors corresponding to lower relative expression values. Bracketed on the right are 6 groups of genes that we selected for subsequent analyses.

The global patterns of gene expression over time that are illustrated in Figure 14 indicate that the transcription of these 2,879 genes in response to WT- and DUB-mut-MHV infection in BMDMs was remarkably similar over time, whereas the response to EndoU-mut-MHV infection was profoundly distinct. In other words, the absence of an enzymatically active EndoU protein—but not the absence of a fully functional DUB protein—was sufficient to elicit dramatic differences in the transcriptional response to infection compared to WT-MHV infection. These results therefore suggest that the enzymatic activity of the WT-EndoU protein broadly regulates the cellular response to infection, whereas the WT-DUB protein participates in a much narrower range of regulatory processes. To further differentiate between the transcriptional profiles of the different infection groups, we next individually analyzed several groups of genes from the heatmap in Figure 14.

## Functional Clustering/Gene Ontological Analyses of Differentially-Expressed Genes

We bracketed several distinct groups of genes within the heatmap in Figure 14 and numbered them 1-6. We sought to determine if these groups of genes, which had already been mathematically clustered together in Figure 14 based on similarities in their expression patterns, encode proteins that also have similar functions. Figure 15 shows a schematic of the pipeline that we employed to analyze these groups of genes denoted in Figure 14. Briefly, the list of gene names within each group was converted to the corresponding Ensembl IDs, and those IDs were subjected to gene ontological (aka functional clustering) analyses using an online tool called DAVID (Database for Annotation, Visualization and Integrated Discovery) (Huang et al. 2009a; Huang et al. 2009b). DAVID is a valuable tool for clustering lists of genes based on functional similarities of the proteins that they encode; for example, if a list of genes contains multiple known pro-inflammatory genes, they will be clustered together under a blanket term like "inflammation" or "inflammatory response." Additionally, each functional cluster is associated with a q-value that is indicative of the false-discovery rate (FDR, via the Benjamini-Hochberg Procedure) and represents the statistical significance of a given cluster. A cluster generated by DAVID will meet statistical significance (which we defined as $q < 0.05$) if it contains a sufficient number of genes to be considered a non-random enrichment of the functional group in the context of the full list of genes that was originally submitted to DAVID for analysis. Table 3 shows the results of these DAVID analyses for each of the 6 groups of genes denoted in Figure 14. The column labeled "Total genes in group" refers to the total number of genes in each group that were submitted to DAVID for gene name conversion and subsequent clustering; notably, not all of these genes correspond to Ensembl IDs and not all Ensembl IDs were ultimately clustered by DAVID into clusters of statistical significance. The column titled "Statistically significant functional clusters within group" shows the functional clusters within each group that were statistically significant. As there was substantial redundancy among many of the clusters, we further organized the functional clusters into groups of essentially redundant terms (e.g., "immune response" represents functional cluster terms such as "immune response," "inflammatory response," "inflammation," etc.). "Unique genes in statistically significant clusters" refers to the total number of genes in each group that were clustered into at least one of the functional clusters that met statistical significance in that group. A gene that appears in multiple clusters of statistical significance is counted as one unique gene. In this way, as outlined in Figure 15, we extracted all of the unique, statistically significant functionally-clustered genes from the groups in Figure 14. As shown in Table 3, genes in Groups 5 and 6 were not clustered by DAVID into any clusters of statistical significance, indicating that the genes within those groups are not highly functionally similar despite having been grouped together based on similar expression patterns. Therefore, Groups 5 and 6 were not further analyzed. We next generated heatmaps of the expression profiles of the unique genes in statistically significant functional clusters from each of the remaining 4 groups, which are shown in Figures 16-19. The names of the genes whose expression profiles are displayed in the heatmaps Figures 16-19 are listed, in order, in Tables S2-S5 in the Appendix of this document. Finally, the unique, functionally-clustered genes within each group were ordered from most- to least-highly upregulated in terms of their expression levels in WT-MHV-infected BMDMs at 12 hpi compared to mock-infected BMDMs, and the normalized counts for the top 12 genes from each group whose expression was associated with at least 100 normalized counts in any sample were plotted over time. These line graphs are displayed in Figures 16-19.

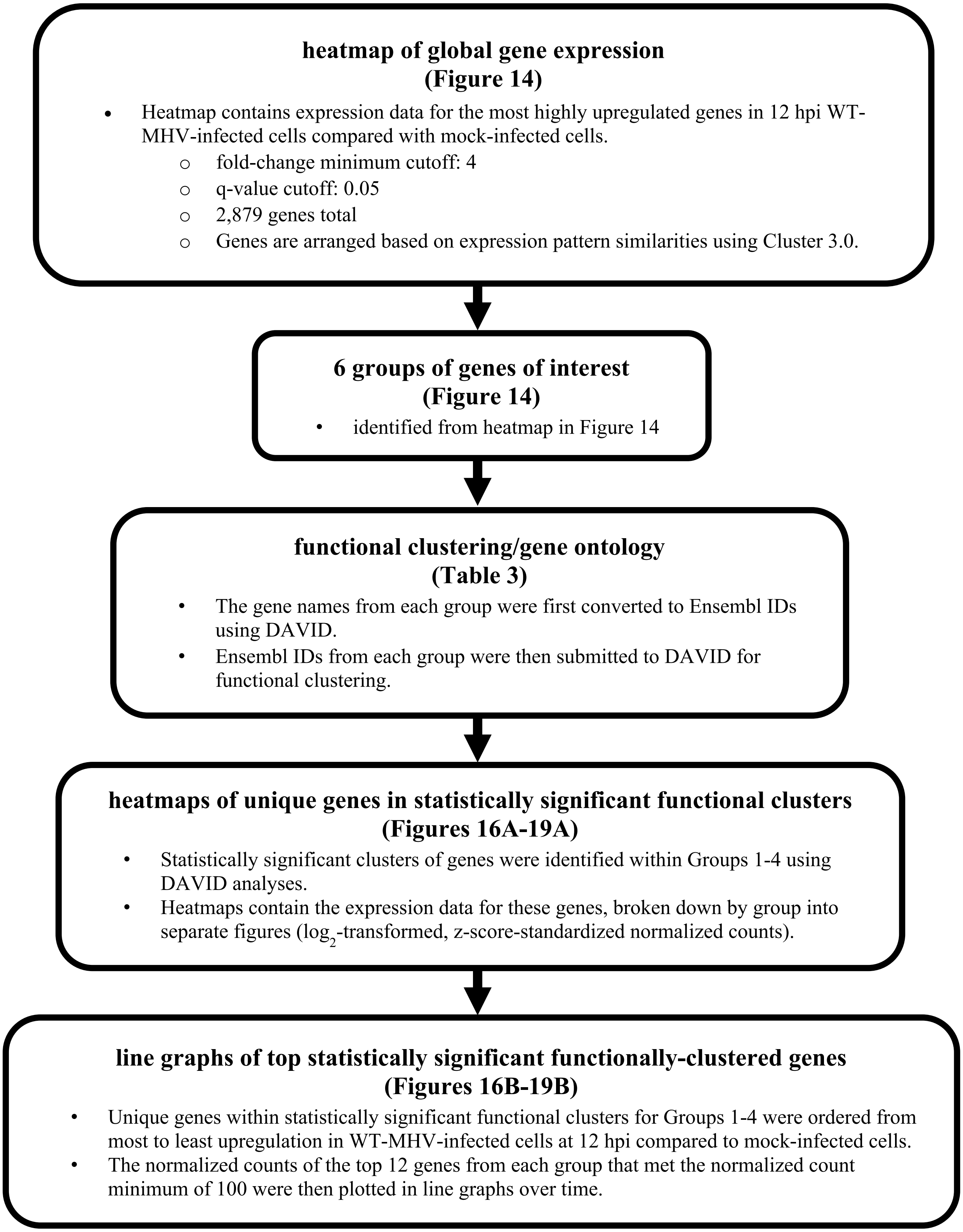

**heatmap of global gene expression (Figure 14)**

- Heatmap contains expression data for the most highly upregulated genes in 12 hpi WT-MHV-infected cells compared with mock-infected cells.
  - fold-change minimum cutoff: 4
  - q-value cutoff: 0.05
  - 2,879 genes total
  - Genes are arranged based on expression pattern similarities using Cluster 3.0.

**6 groups of genes of interest (Figure 14)**

- identified from heatmap in Figure 14

**functional clustering/gene ontology (Table 3)**

- The gene names from each group were first converted to Ensembl IDs using DAVID.
- Ensembl IDs from each group were then submitted to DAVID for functional clustering.

**heatmaps of unique genes in statistically significant functional clusters (Figures 16A-19A)**

- Statistically significant clusters of genes were identified within Groups 1-4 using DAVID analyses.
- Heatmaps contain the expression data for these genes, broken down by group into separate figures ($\log_2$-transformed, z-score-standardized normalized counts).

**line graphs of top statistically significant functionally-clustered genes (Figures 16B-19B)**

- Unique genes within statistically significant functional clusters for Groups 1-4 were ordered from most to least upregulation in WT-MHV-infected cells at 12 hpi compared to mock-infected cells.
- The normalized counts of the top 12 genes from each group that met the normalized count minimum of 100 were then plotted in line graphs over time.

**Figure 15. Schematic of Analysis and Data Presentation Methods Applied to Genes in Groups 1-6.** After generating the heatmap in Figure 14 (top bubble), 6 groups of genes of interest (labeled Groups 1-6) were identified from the heatmap based on noteworthy patterns of

expression across infection groups (second bubble). The gene names in each group were converted to Ensembl IDs using DAVID and the resulting lists of Ensembl IDs were submitted to DAVID for functional clustering analyses (third bubble). The results of these analyses are shown and described in Table 3. The expression patterns of each of the unique genes from statistically significant functional clusters within each group were then plotted in a separate heatmap for each group, shown in Figures 16A-19A (fourth bubble). Finally, the top 12 unique genes from statistically significant functional clusters within each group were then selected based on highest degree of upregulation in WT-MHV-infected cells at 12 hpi compared with mock-infected cells with a minimum normalized count cutoff of at least 100 counts; the normalized counts of these genes (48 total) were then plotted over time in Figures 16B-19B (bottom bubble).

| Group | Total genes in group | Statistically significant functional clusters within group | Unique genes in statistically significant functional clusters |
|---|---|---|---|
| 1 | 231 | immune response (11)<br>signaling cascades (1) | 30 |
| 2 | 520 | transcription (2)<br>protein ubiquitination (2)<br>embryonic hemopoiesis (1)<br>phosphorylation (1) | 151 |
| 3 | 466 | immune response (60)<br>signaling cascades (14)<br>transcription and cell proliferation (6)<br>apoptosis (5)<br>response to non-microbial stimuli (5)<br>host/symbiont biology (2) | 203 |
| 4 | 623 | transcription (3)<br>immune response (3)<br>signaling cascades (2) | 149 |
| 5 | 491 | none | N/A |
| 6 | 91 | none | N/A |

**Table 3. Functional Clustering Analyses of Gene Groups 1-6 Using DAVID.** Genes from each of the 6 groups bracketed in Figure 14 were submitted to DAVID for functional clustering, as described in Figure 15. Shown here are the results of these analyses, including the total genes in each group that were originally submitted to DAVID for clustering (second column), the number of statistically significant functional clusters within each of the 6 groups as determined by DAVID (third column), and the number of unique genes that appear in at least one of the statistically significant functional clusters within each group (last column). Because DAVID reported many functional clusters that were semantically redundant, we further condensed the

results of these DAVID analyses into the clusters shown in the third column. The number in parentheses after each of the terms listed in the third column indicates the number of statistically significant DAVID-generated clusters that we condensed into each larger cluster (i.e., we binned 60 statistically significant functional clusters within Group 3 into the "immune response" term shown in the third column). Groups 5 and 6 were not associated with any functional clusters of statistical significance. N/A, not applicable.

Note that the reads from the same 3 hpi mock-infected BMDMs were included as a negative control during analyses of all timepoints and are also plotted in all panels in Figures 16-19. Due to the process by which DESeq2 normalizes counts across samples, which corrects for differences in the total number of mapped reads between samples, it may appear in some individual line graphs within Figures 16-19 as though the number of reads from the same mock-infected samples are somehow decreasing over time. However, this trend is merely an artifact of the read normalization process and is due in this case to the fact that the total number of reads mapping to the murine host genome decreased in MHV-infected samples as infection progressed. In other words, the total number of murine reads in an MHV-infected sample at 12 hpi was significantly lower than the number of murine reads in a mock-infected sample at 3 hpi because expression of the viral genome dominates cellular transcription machinery in MHV-infected cells by 9-12 hpi. DESeq2 accounts for these differences in sequencing depth by scaling up or down the number of raw counts that were mapped to each gene in each sample according to a "scaling factor" that is calculated from the average of the number of reads pertaining to that gene across all samples included in the analysis. The authors of the DESeq2 package describe this process in detail in their 2014 paper (Love *et al*. 2014). It is therefore best to compare the normalized counts pertaining to each sample against the other samples in that same timepoint (i.e., compare the normalized counts for a particular gene in WT-MHV-infected samples at 12 hpi with the normalized counts for that same gene in EndoU-mut-MHV-, DUB-mut-MHV-, or mock-infected cells at 12 hpi).

The data in Table 3 indicate that genes involved in the immune response, transcription, and various signaling cascades appear in multiple groups in the heatmap in Figure 14. This scattering of functionally similar genes throughout the heatmap is a consequence of the method of clustering that was used to generate Figure 14, which involved ordering the genes based on their expression patterns and not based on their functions. Additionally, it is notable that Group 3 contained the highest number of functional clusters of statistical significance (95) despite having the third-lowest number of total genes of all 6 groups. However, most of these clusters within Group 3 were essentially redundant (60 clusters were various iterations of “immune response” genes, for example) and most of the 203 unique genes in Group 3 were clustered by DAVID into more than one functional cluster.

### Group 1.

The 4 groups containing genes that were organized by DAVID into statistically significant functional clusters (Groups 1-4) can be classified in terms of the gene expression profile associated with EndoU-mut-MHV-infected BMDMs in each group. Thus, Group 1 contains genes that were most highly expressed in EndoU-mut-MHV-infected cells; Group 2, on the other hand, includes genes that were least highly expressed in EndoU-mut-MHV-infected cells; and Groups 3 and 4 comprise genes that were associated with an intermediate expression phenotype induced by EndoU-mut-MHV relative to the other two groups. Notably, the unique genes in statistically significant functional clusters within Group 1—all of which were most highly expressed during EndoU-mut-MHV infection—include a number of type I IFN genes (Figure 16A). Indeed, 17 of these 30 genes are type I IFN isoforms. Because the top 12 most upregulated unique genes from Group 1 in WT-MHV-infected cells at 12 hpi compared with mock-infected cells were all type I IFN isoforms with virtually indistinguishable expression profiles, we elected to show only 9 of these isoforms and selected 3 other genes from the Group 1 list—Lta, Oas1b, and Isg15—to display in line graphs Figure 16B. All of the genes in Figure 16B encode proteins that are known to participate in the antiviral response. Importantly, these data indicate that EndoU-mut-MHV elicited a substantially higher type I IFN response than the other two viruses while simultaneously pointing to a similar—yet much subtler—increase in expression of the same type I IFN genes during DUB-mut-MHV infection compared to WT-MHV infection. Our RNA-seq data therefore corroborate the results of qRT-PCR experiments in Figure 11.

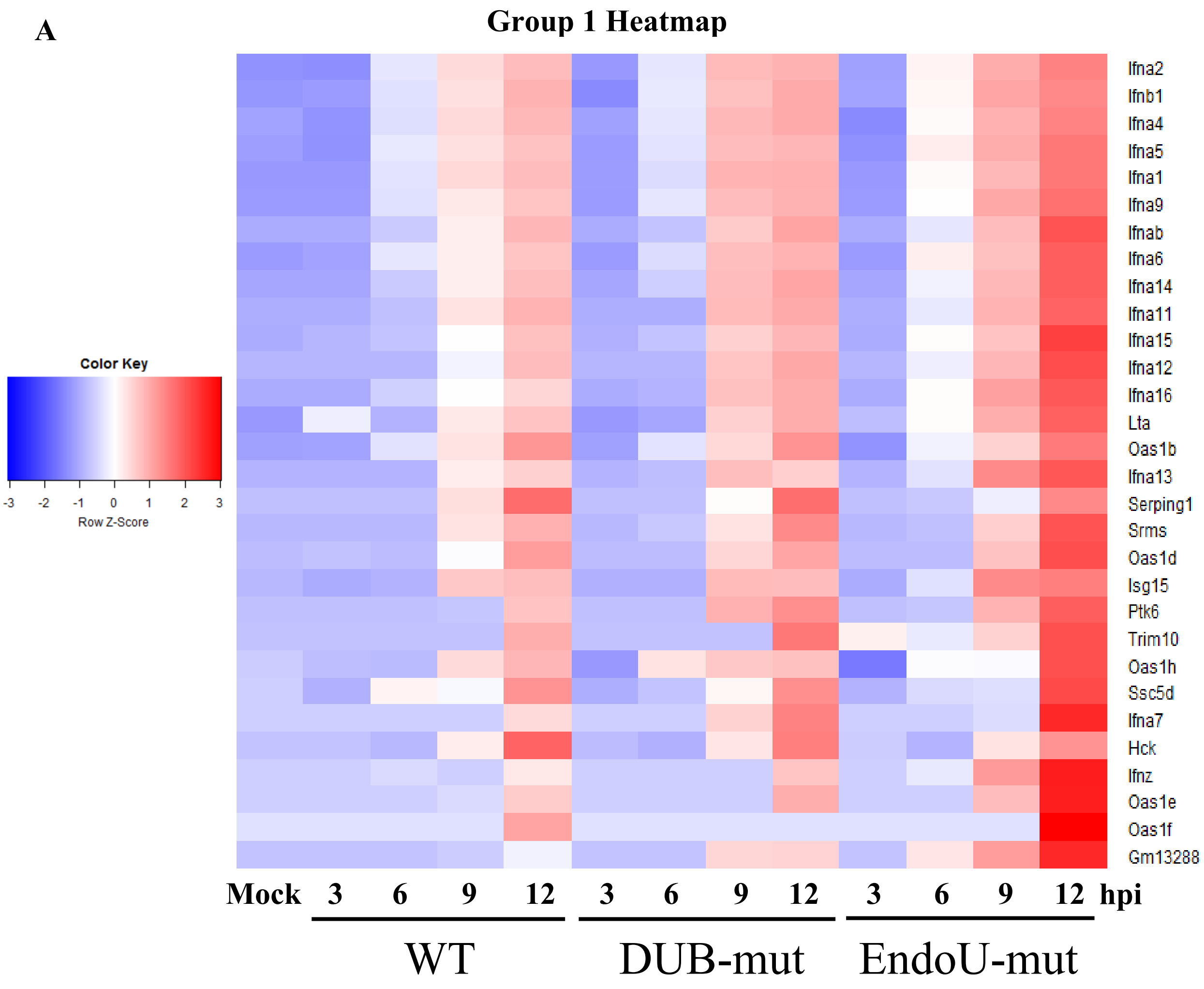

**B** **Group 1 Line Graphs**

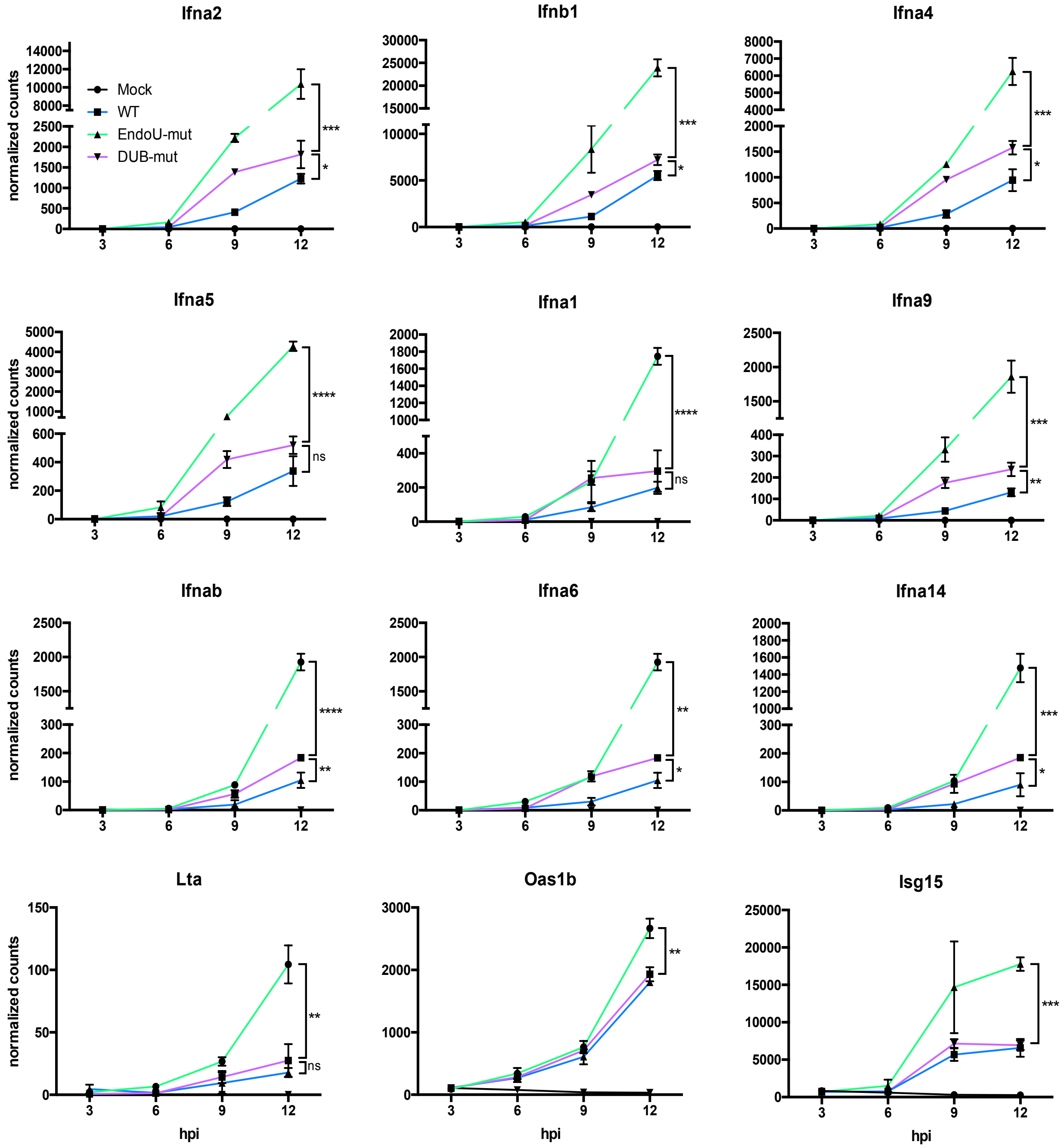

**Figure 16. Expression Profiles of Unique Genes in Statistically Significant Functional Clusters within Group 1.** After applying DAVID functional clustering to Groups 1-6 from Figure 14, the expression profiles of the unique genes in statistically significant functional clusters within Group 1 were plotted as heatmaps and line graphs to emphasize differences in patterns of expression between EndoU-mut-, DUB-mut-, and WT-MHV-infected BMDMs over time (see Table 3). (A) Plotted are row z-score-standardized $\log_2$-transformed means of replicates for all samples. Color bar shows the row z-sore value associated with each color shade,

with warmer colors representing higher relative expression values within a row and cooler colors corresponding to lower relative expression values. See Table S2 in the Appendix for a list of gene names in the order in which they appear in this heatmap. (B) The normalized count values for the top 12 unique genes in statistically significant functional clusters within Group 1 are plotted as line graphs. These genes were chosen by ordering the list of unique genes in statistically significant functional clusters within each group from most- to least-highly upregulated in WT-MHV-infected cells at 12 hpi compared with mock-infected cells. The top 12 genes from each of those lists that was associated with at least 100 normalized counts in any sample were selected. For this group only (and not for Groups 2-4), since the top 12 genes were all type I IFN isoforms with nearly identical expression patterns, we elected to show only 9 of these isoforms and selected 3 other genes from the Group 1 list—Lta, Oas1b, and Isg15—to display here. Plotted are the average normalized counts for each gene in EndoU-mut- (green), DUB-mut- (blue), WT-MHV- (lilac), and mock-infected (black) BMDMs infection groups over all 4 timepoints. The normalized counts from each infection group at 12 hpi were subjected to statistical testing using two-tailed Student's t-tests. * $p < 0.05$; ** $p < 0.01$; *** $p < 0.001$; **** $p < 0.0001$; ns, not significant. Data are presented as means ± SD.

### Group 2.

Unlike in Group 1, the unique genes in statistically significant functional clusters within Group 2, whose expression profiles are shown in a heatmap in Figure 17A, were *least* highly expressed in EndoU-mut-MHV-infected cells compared with DUB-mut- and WT-MHV-infected cells. The majority of these genes encode proteins that act in transcription (Table 3), a few of which appear to have been differentially expressed between DUB-mut- and WT-MHV-infected cells. The normalized counts for some of these genes are plotted in line graphs in Figure 17B.

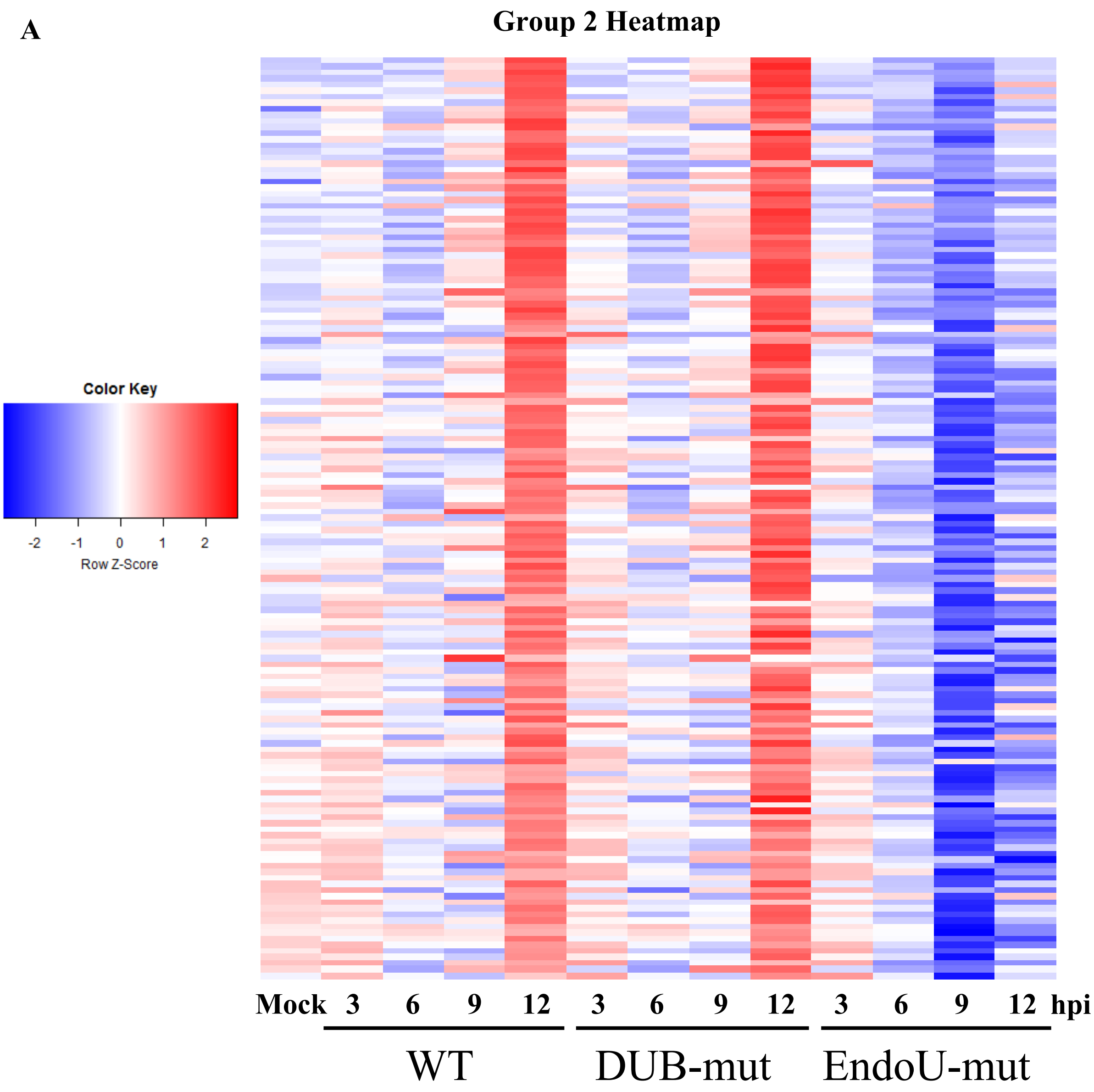
A
Group 2 Heatmap
Color Key
-2
-1
0
1
2
Row Z-Score
Mock
3
6
9
12
3
6
9
12
3
6
9
12
hpi
WT
DUB-mut
EndoU-mut

**B** Group 2 Line Graphs

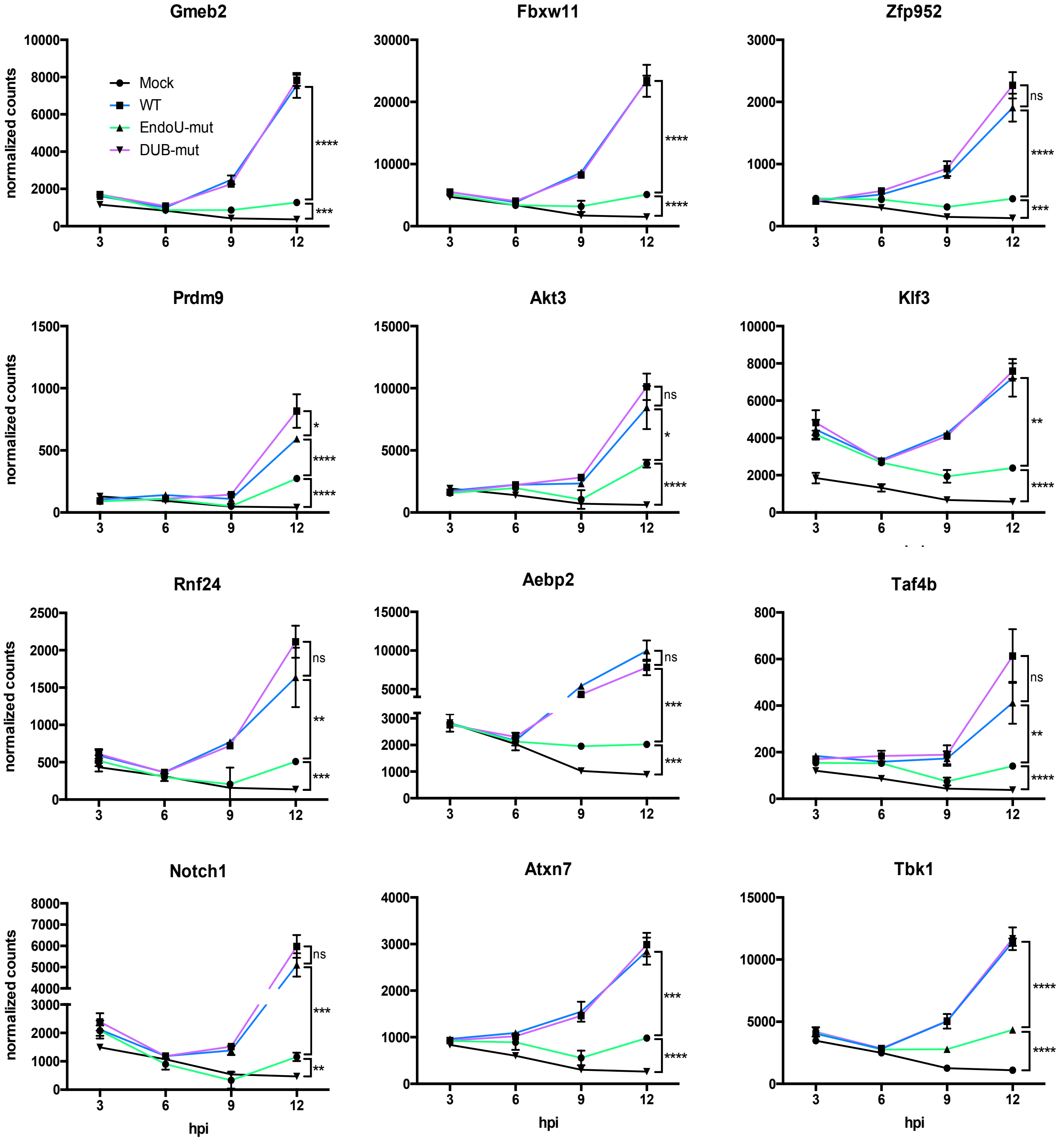

**Figure 17. Expression Profiles of Unique Genes in Statistically Significant Functional Clusters within Group 2.** See Figure 16 for figure legend. See Table S2 for a list of gene names in the order in which they appear in this heatmap.

**Group 3.**

The unique genes in statistically significant functional clusters within Groups 3 and Groups 4 were, in general, least highly expressed in EndoU-mut-MHV-infected cells (albeit still more highly expressed in these cells than were the genes in Group 2). Group 3 most notably contains a number of canonical pro-inflammatory cytokines and chemokines (Tnf, Il1a/Il1b, Il6, Il12a/Il12b, Csf1, Cxcl10, Cxcl11, among others), a host of known antiviral defense genes and sensors of viral infection (including Ifit1/Isg56, Ifit2, Ifit3, Ddx58/RIG-I, and Eif2ak2/PKR), as well as genes involved in the regulation of NF-κB activation and signaling (including Rel/NF-κB, IκBα, IκBδ, and Ikbke). The expression profiles of these genes are shown in a heatmap and line graphs in Figures 18A and 18B, respectively. Unlike the genes in Groups 1 and 2, the genes in Group 3 generally were not associated with a statistically significant differential expression profile in DUB-mut-MHV-infected cells compared with WT-MHV-infected cells. Together, the data in Figure 18 strongly suggest that the macrophages infected with EndoU-mut-MHV were in a significantly less pro-inflammatory state than were the cells infected with either DUB-mut- or WT-MHV. The data also indicate that DUB-mut- and WT-MHV appear to have elicited inflammatory and antiviral responses of similar magnitude, as evidenced by the overwhelming lack of statistically significant differences in gene expression between the DUB-mut- and WT-MHV infection groups.

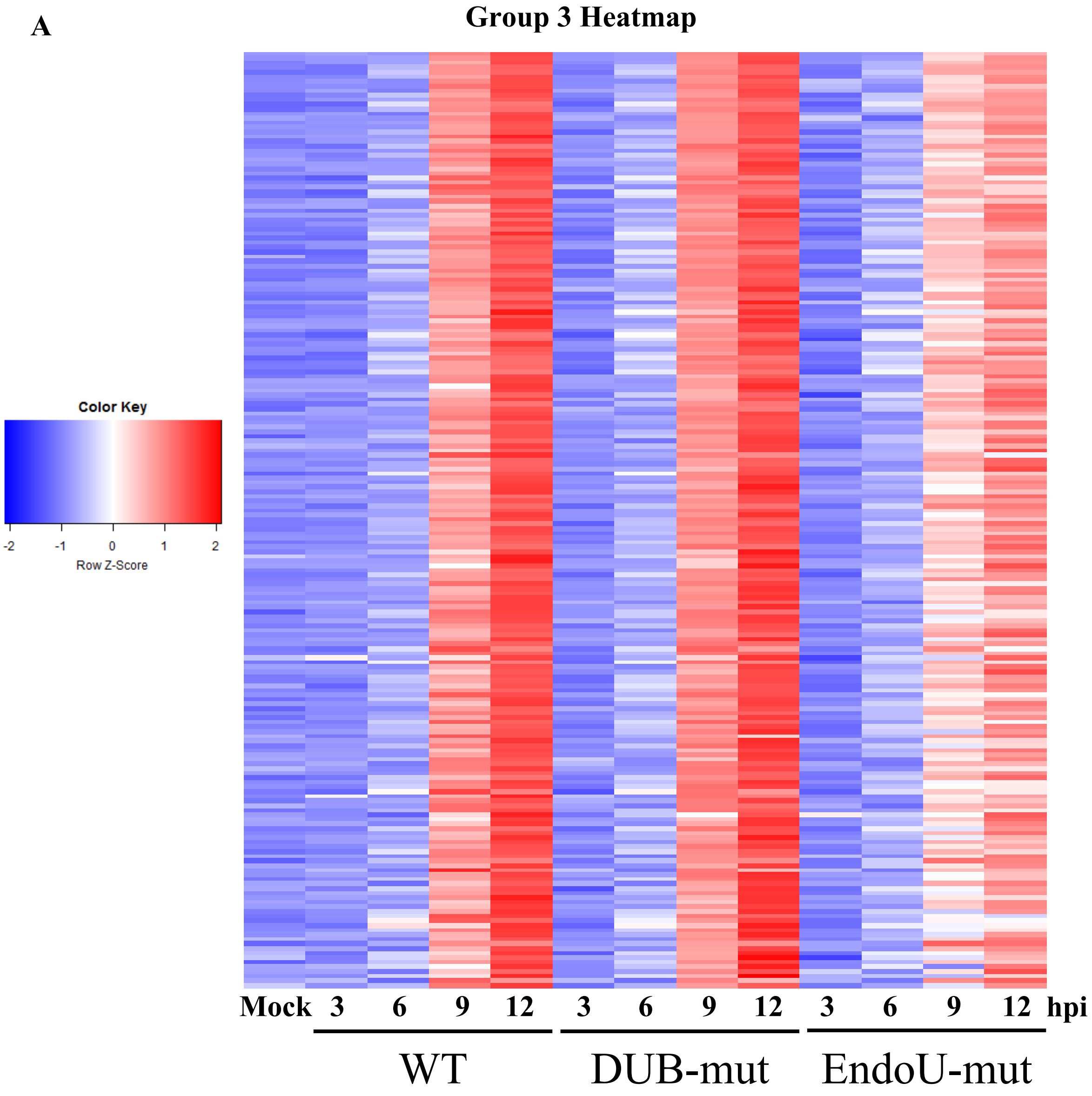
A
Group 3 Heatmap
Color Key
-2
-1
0
1
2
Row Z-Score
Mock
3
6
9
12
3
6
9
12
3
6
9
12
hpi
WT
DUB-mut
EndoU-mut

# Group 3 Line Graphs

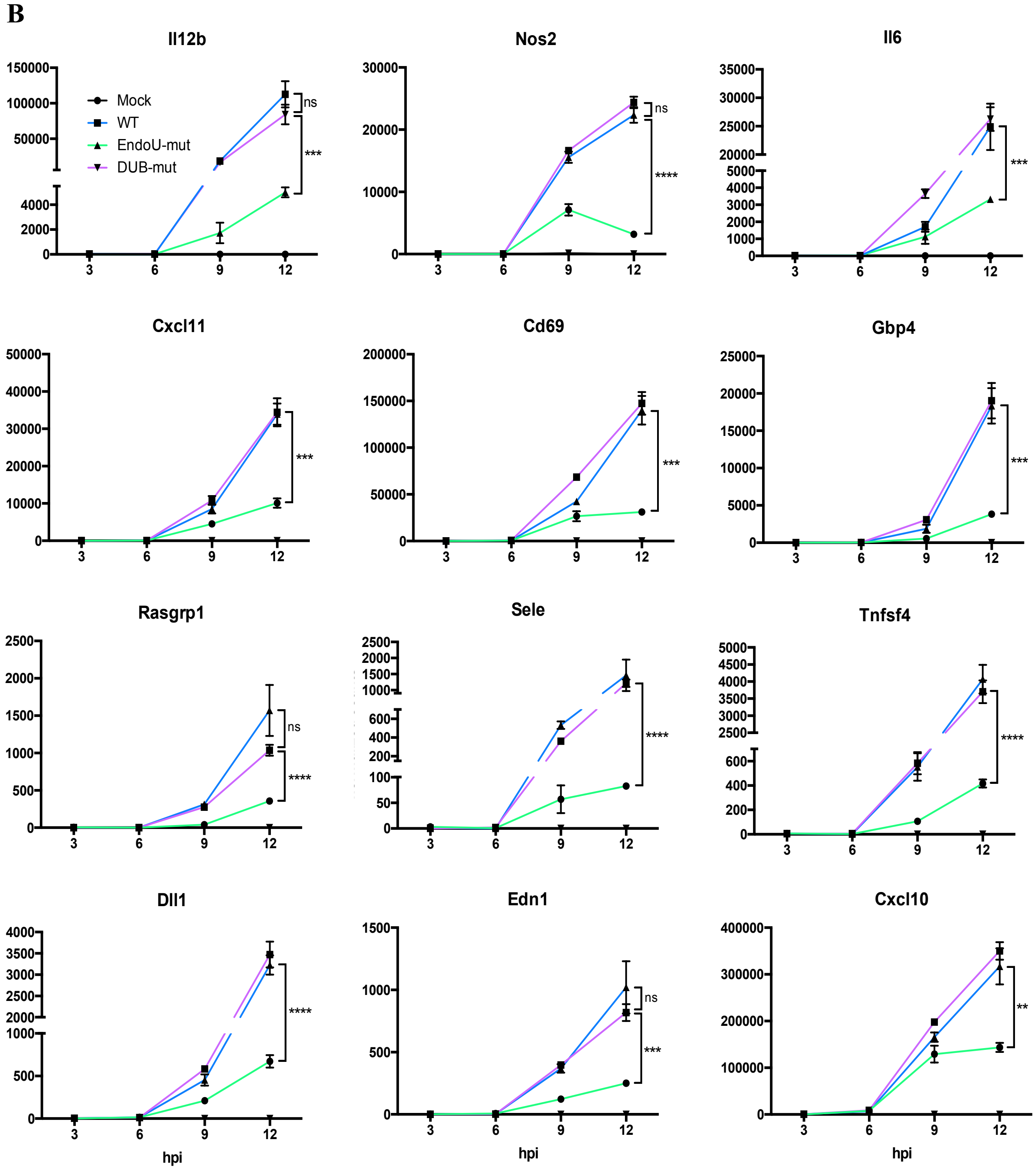

**Figure 18. Expression Profiles of Unique Genes in Statistically Significant Functional Clusters within Group 3.** See Figure 16 for figure legend. See Table S4 for a list of gene names in the order in which they appear in this heatmap.

### Group 4.

Finally, similar to Group 2, the majority of the unique genes in statistically significant functional clusters within Group 4 encode proteins that are involved in transcription, most commonly by acting as transcription factors or molecules that participate in signaling cascades that terminate in large-scale transcriptional changes (Table 3). The expression profiles of these genes are shown in a heatmap and line graphs in Figure 19. Interestingly, in addition to being significantly less highly expressed in EndoU-mut-MHV-infected cells, many of the in Group 4 were also associated with statistically significant differential expression between DUB-mut- and WT-MHV infection groups, demonstrated by the line graphs in Figure 19B. We note that several of these genes—including Plagl1, Kalm, Zfhx4, Asap3, and others—were in fact *most* highly induced by DUB-mutant-MHV infection. A few other genes were not differentially expressed at all between virus-infected groups. The data in Figures 17-19 (which display the expression data from the genes in Groups 2-4, respectively) indicate that the macrophages infected with EndoU-mut-MHV were much less transcriptionally active than were the cells infected with DUB-mut- or WT-MHV. Taken together, the results of our RNA-seq experiments, including the functional clustering analyses that we applied to groups of DEGs, provide compelling data to suggest that DUB-mut-MHV elicited matching expression patterns of all but a select few genes compared with WT-MHV, whereas EndoU-mut-MHV induced a profoundly distinct transcriptional response that differentially impacted the expression of more than 2,800 genes. Potential mechanisms that may contribute to the dysregulation of genes in Groups 1-6 are described in the Discussion chapter of this document.

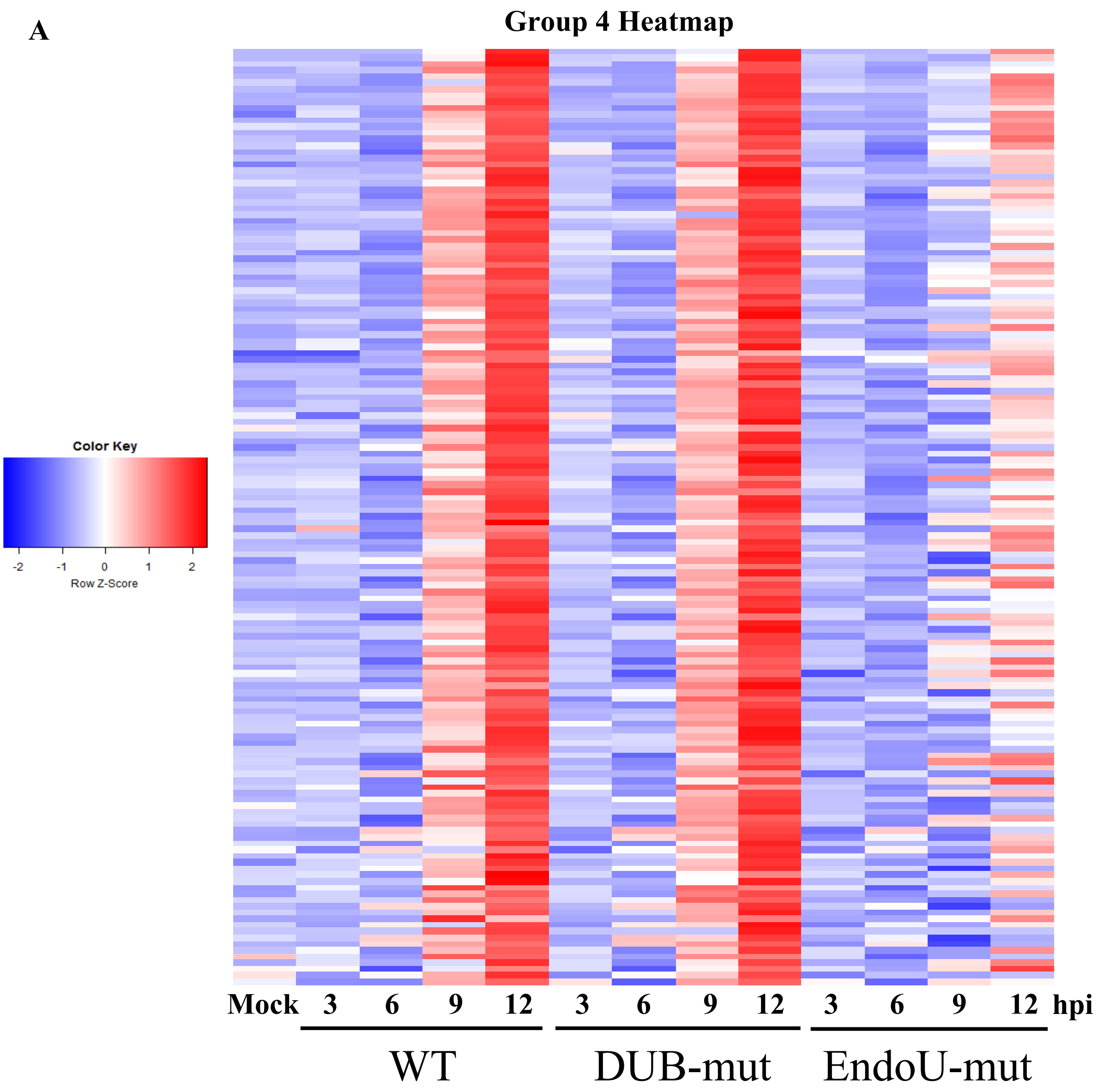
A
Group 4 Heatmap
Color Key
-2
-1
0
1
2
Row Z-Score
Mock
3
6
9
12
3
6
9
12
3
6
9
12
hpi
WT
DUB-mut
EndoU-mut

**B**

## Group 4 Line Graphs

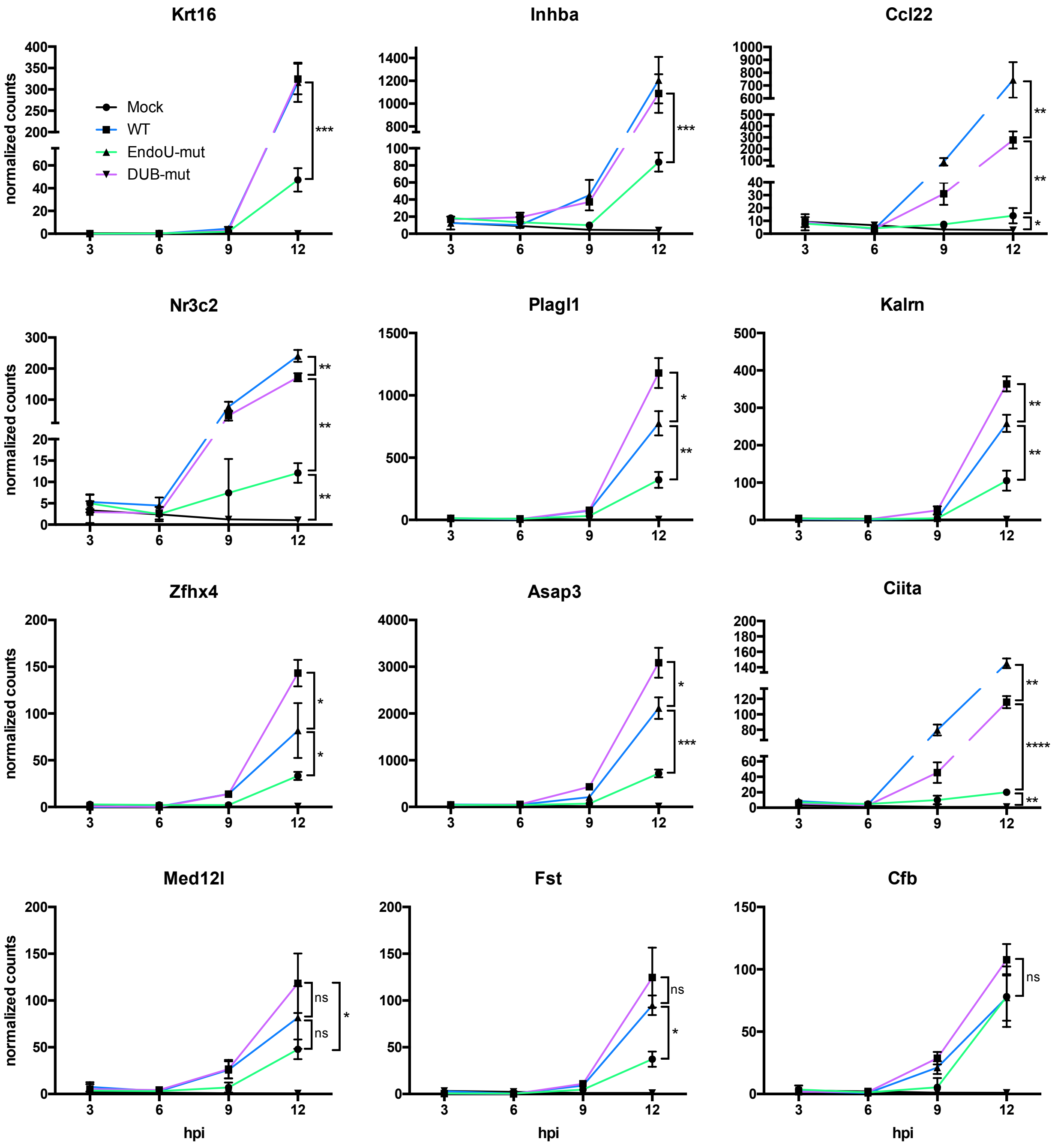

**Figure 19. Expression Profiles of Unique Genes in Statistically Significant Functional Clusters within Group 4.** See Figure 16 for figure legend. See Table S5 for a list of gene names in the order in which they appear in this heatmap.

# CHAPTER IV

# DISCUSSION

## Overview of Results

The work described herein is, to the best of our knowledge, the first report of applying global transcriptome profiling to an immune cell type infected with a mutant coronavirus or the WT parental strain. Using virus-infected primary murine BMDMs, we report that both EndoU-mut- and DUB-mut-MHV induced significantly elevated expression of multiple type I IFN isoforms relative to WT-MHV as early as 6 hpi, with EndoU-mut-MHV-infected BMDMs expressing the highest levels of these transcripts (Figures 11 and 16). Interestingly, aside from these type I IFN genes and a handful of other genes that were most highly expressed during EndoU-mut-MHV infection, the vast majority of the 2,879 genes that were most highly upregulated during WT-MHV infection at 12 hpi relative to mock were, by comparison, *least* highly expressed in EndoU-mut-MHV-infected cells (Figure 14). Functional clustering analyses revealed that these genes comprised a host of canonical pro-inflammatory cytokines (including Tnf, Il6, Il1, and Il2, along with multiple chemokines), antiviral defense genes and sensors of viral infection, regulators of NF-κB activity, as well as a number of other genes that are known to be involved in the induction and/or regulation of transcription (Figures 17-19). These findings are in line with a recent report describing the expression profiles of 754 genes in BMDMs 5-14 dpi with a gliatropic strain of MHV, in which the authors describe the upregulation of a large cluster of pro-inflammatory genes (Savarin *et al*. 2018). Interestingly, Cheung *et al*. (2005) also demonstrated upregulation of several chemokines by 3 hpi in SARS-CoV-infected primary human monocyte-derived macrophages, whereas we did not observe any differential expression at all until 6 hpi. We speculate that this disparity is a product of temporally distinct responses elicited by SARS-CoV and MHV.

Despite containing a marked increase in type I IFN mRNAs during DUB-mut-MHV infection, BMDMs infected with this strain exhibited a transcriptional response that was statistically indistinguishable from that induced by WT-MHV at all timepoints with few exceptions. It is noteworthy that the widespread transcriptional changes associated with EndoU-mut-MHV infection, for which but a single amino acid change in nsp15 was responsible, were accompanied by attenuation of the virus, whereas neither DUB-mut- nor WT-MHV was attenuated (Figure 12). These results indicate that the mere induction of type I IFN in the context of an IFN antagonist-deficient coronavirus is not a sufficient marker for attenuation of the virus or for substantial transcriptional dysregulation of host genes in response to the infection; instead, the *magnitude* of type I IFN expression is key. That EndoU-mut-MHV induced a profoundly higher type I IFN response than even the DUB-mut virus suggests that there is a threshold of IFN expression that must be crossed before a host macrophage mounts a differential response to an IFN antagonist-deficient coronavirus that is capable of mitigating the infection.

### Impact of IFN Expression and Signaling.

Our data indicate that substantial expression of type I IFNs occurred early during infection (by 6 hpi) with each of the 3 viruses used in this study, albeit to profoundly different degrees depending on the particular virus (Figures 11 and 16). However, it is important to note that the expression of IFN isoforms that we observed during our experiments may not have prompted substantial IFN *signaling* or IFN-induced gene expression within the temporal constraints of the timecourse. We previously reported that IFN-α is first detectable in the supernatants of EndoU-mut- and WT-MHV-infected BMDMs between 8 and 12 hpi; in order to influence gene expression, that secreted IFN must then interact with its receptor (IFNAR) on the surfaces of cells in a paracrine or autocrine manner, triggering a signaling cascade that eventually terminates in altered gene expression (Ivashkiv and Donlin 2014; Deng *et al*. 2017). Thus, it is unclear if the enhanced expression of type I IFN that we observed in the context of EndoU-mut- and DUB-mut-MHV infection of BMDMs ultimately influenced the global transcriptional profiles of those cells. Although a handful of groups have published the expression data for a select few genes upon treatment with type I IFN, to our knowledge there exist no published data illuminating the transcriptional profiles of type I IFN-treated macrophages with which we could compare the data that we obtained in this study (Zhou *et al*. 2010; Pertsovskaya *et al*. 2013; Kroetz *et al*. 2015; Labzin *et al*. 2015). We aim to investigate the global transcriptional changes induced in macrophages by type I IFN alone in the near future. From the current study, we conclude that the magnitude and timing of the expression of type I IFN represent a useful *marker* for virus attenuation when studying IFN antagonist-deficient coronaviruses, but whether or not the attenuation of such mutant viruses is due to the induction and downstream signaling of type I IFN remains to be elucidated.

## Mechanisms of Extensive Transcriptional Changes during CoV Infection

### Apoptosis.

Why was global transcription in EndoU-mut-MHV-infected cells dramatically diminished relative to the other two infection groups and why did these cells appear to be significantly less pro-inflammatory in their gene expression profiles despite expressing the highest levels of type I IFNs? One possibility stems from the observation that the replication of

EndoU-mut-MHV is rapidly attenuated during infection of BMDMs compared with DUB-mut- and WT-MHV infection (Figure 12). This early attenuation of EndoU-mut-MHV replication might ultimately mean that macrophages infected with EndoU-mut-MHV, but not DUB-mut- or WT-MHV, were not sufficiently activated to increase the transcription of the pro-inflammatory genes. But what is responsible for disrupting the replication of EndoU-mut-MHV as early as 6 hpi? We and others previously demonstrated that nsp15-EndoU limits apoptosis in macrophages during infection; therefore, it might be the case that BMDMs infected with EndoU-mut-MHV sensed the mutant virus (*via* the PKR and OAS/RNase L pathways, as we have shown) and subsequently began the process of apoptosis so early during infection that the infected cells simply did not have a chance to initiate a broad pro-inflammatory state before dying (Lei *et al*. 2013; Deng *et al*. 2017). Additional work is required to clarify the intriguing and apparently inverse relationship between type I IFN expression and the expression of pro-inflammatory genes in the context of WT- and IFN antagonist-deficient coronavirus infections. The mechanisms that contribute to the early attenuation of EndoU-mut-MHV replication and gene expression, including the role of apoptosis, also warrant further investigation.

### ER Stress.

If early apoptosis might have contributed to the unique transcriptional profile that we obtained from EndoU-mut-MHV-infected BMDMs, what mechanism(s) could explain the markedly enhanced transcriptional activation of host genes that we observed in DUB-mut- and WT-MHV-infected cells? Why did DUB-mut- and WT-MHV-infected BMDMs exhibit the highest pro-inflammatory responses? Indeed, why did WT-MHV elicit such markedly amplified expression of so many genes in general? WT-MHV encodes multiple IFN antagonists, including a functional EndoU that, as we and others recently showed, is required for the evasion of multiple cellular dsRNA sensors (Deng *et al*. 2017; Kindler *et al*. 2017). Therefore, we expected that impaired sensing of viral dsRNA in the context of WT-MHV infection would correspond to a limited host transcriptional response overall, but found precisely the opposite to be true. Having completed a literature search to address these questions, we now speculate that cellular stressors including mitochondrial oxidative stress and endoplasmic reticulum (ER) stress may have played a role in shaping the observed transcriptional responses to the viruses used in this study. Several groups have published compelling data demonstrating that coronaviruses induce substantial oxidative and ER stress during infection, which can have a number of outcomes, including the induction of pro-inflammatory cytokines, translation attenuation, and if left unresolved, eventual apoptosis (Mogensen *et al*. 2003; DeDiego *et al*. 2011; Fung and Liu 2014; Siu *et al*. 2014; Smith 2014; Reineke *et al*. 2015; Fung *et al*. 2016). In particular, it is increasingly clear that coronavirus-induced ER stress and the unfolded protein response that cells mount to alleviate such stress may activate NF-κB-mediated inflammation through multiple pathways, thereby possibly contributing to the transcriptomic profiles that we observed in this study.

ER stress is primarily caused by an accumulation of unfolded proteins within the ER (Xu *et al*. 2005; Smith 2014). Virus infections represent just one of several possible root causes of unfolded protein accumulation since the mass-production of virions using viral proteins places enormous strain on a host cell's protein folding machinery (Xu *et al*. 2005; Smith 2014). Upon detecting ER stress through special sensing pathways within the ER, the cell initiates an unfolded protein response (UPR) in an effort to resolve the source of the stress; this UPR, in turn, can activate a pro-inflammatory response in a process that was recently referred to in one paper as "a new paradigm" of innate immune sensing of viruses (Fung and Liu 2014; Smith 2014; Fung *et al*. 2016). The UPR comprises 3 known pathways, depicted in Figure 20.

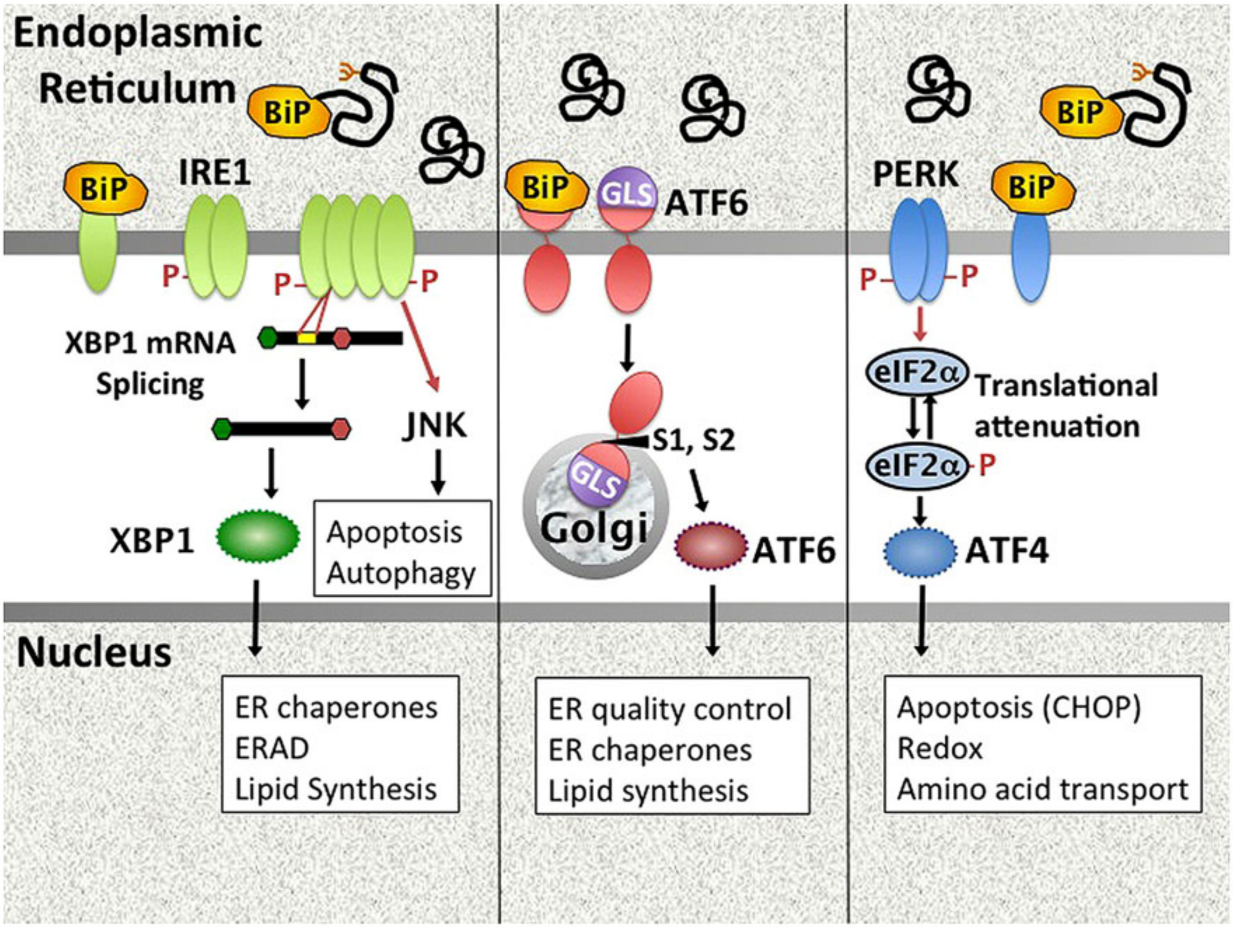

**Figure 20. The Unfolded Protein Response.** The UPR comprises 3 signaling pathways. In unstressed cells, the initiating members of these pathways—IRE1, ATF6, and PERK—are held in an inactive state by BiP, a folding chaperone protein. Each pathway is activated upon the release of BiP. (Left) IRE1 oligomerizes after releasing BiP, initiating a signaling cascade involving JNK and XBP1. (Middle) BiP release from ATF6 reveals a Golgi localization signal (GLS) in ATF6. Upon trafficking to the Golgi, ATF6 is cleaved to produce an active transcription factor. (Right) Once released from BiP, PERK attenuates most translation by phosphorylating eIF2α. In boxes are cellular processes regulated by the UPR, including apoptosis, ERAD (ER associated degradation), lipid synthesis, the expression of ER chaperones, etc. Used with permission from Smith (2014).

An evolving view of the 3 UPR pathways involves the addition of NF-κB and the expression of NF-κB-induced pro-inflammatory genes as a downstream consequence of UPR initiation. For example, PERK-mediated translation attenuation has been shown to activate NF-κB by reducing the protein levels of NF-κB inhibitor IκBα; it has also been proposed that PERK-induced modulation of JNK and p38 (initiated by phosphorylation of eIF2α) may also regulate the expression of pro-inflammatory cytokines (Deng *et al*. 2004; Tam *et al*. 2012; Fung and Liu 2014; Smith 2014). In a similar vein, several labs have published data collectively indicating that IRE1 activation synergistically augments the innate immune response by increasing the activation of NF-κB (Hu *et al*. 2011; Tam *et al*. 2012; Fung and Liu 2014; Smith 2014). Together, these findings point to a role for the ER stress-induced UPR in innate immunity.

Coronavirus infections may be particularly potent sources of ER stress and activators of the UPR due to the expression of their extremely large genomes and the subsequent folding of massive quantities of viral proteins, CoV-induced reorganization of ER membranes to generate the DMVs in which CoV replication complexes are assembled, and depletion of ER membranes during the budding of nascent virions (Fung and Liu 2014; Fung *et al*. 2016). Indeed, multiple groups have reported increased detection of ER stress and UPRs in cells infected with coronaviruses including MHV, SARS-CoV, HCoV-HKU1, MERS-CoV, and IBV (Raaben *et al.* 2007; Bechill *et al.* 2008; DeDiego *et al*. 2011; Fung *et al*. 2014; Siu *et al*. 2014; Rabouw *et al*. 2016; Irigoyen *et al*. 2018). Notably, MHV has been shown to activate all 3 UPR pathways during infection (Raaben *et al*. 2007; Bechill *et al*. 2008; Irigoyen *et al*. 2018). In the current study, using our RNA-seq data, we also detected activation of the UPR by 12 hpi based on increased expression of at least 9 genes that are known to be transcriptional targets of the PERK (Atf4, GADD153/CHOP/Ddit3, and Dusp1), IRE1 (Erdj4/Dnajb9, Edem1, and $p58^{IPK}$/Dnajc3), and ATF6 (GRP78/BiP/Hspa5, GRP94/Hsp90b1, and Herpud1) pathways (Wu *et al*. 2007; Fung and Liu 2014; Smith 2014; Irigoyen *et al*. 2018). These results are illustrated in Figure 21.

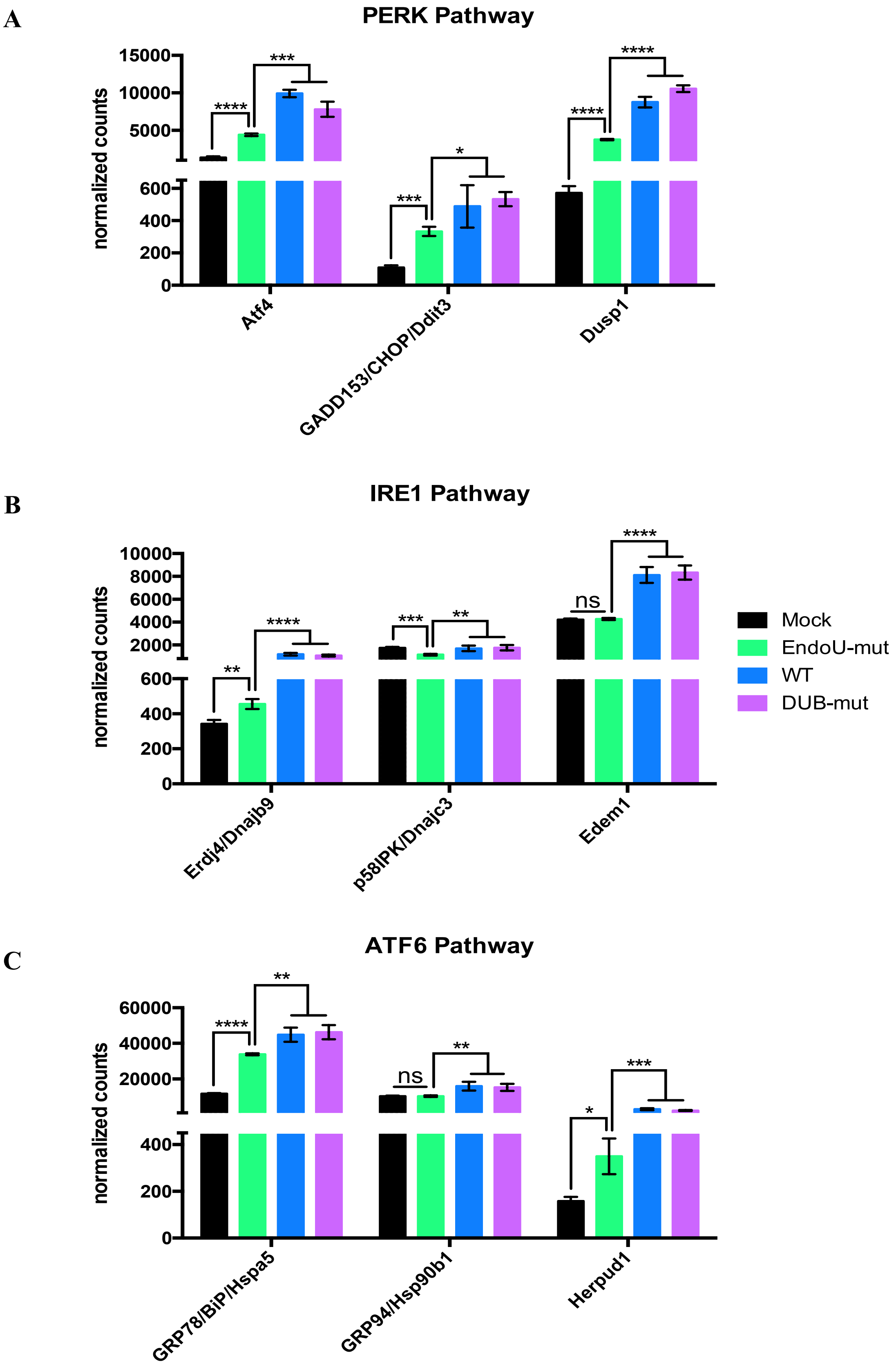
A
PERK Pathway
normalized counts
15000
10000
5000
600
400
200
0
****
***
*
***
****
****
Atf4
GADD153/CHOP/Ddit3
Dusp1
B
IRE1 Pathway
normalized counts
10000
8000
6000
4000
2000
600
400
200
0
**
****
***
**
ns
****
Erdj4/Dnajb9
p58IPK/Dnajc3
Edem1
Mock
EndoU-mut
WT
DUB-mut
C
ATF6 Pathway
normalized counts
60000
40000
20000
400
200
0
**
****
ns
**
*
***
GRP78/BiP/Hspa5
GRP94/Hsp90b1
Herpud1

**Figure 21. Expression of Genes Targeted by UPR Pathways in EndoU-mut-, DUB-mut-, and WT-MHV-infected BMDMs at 12 hpi.** The normalized count values for 9 UPR-induced genes at 12 hpi are plotted. Genes are grouped into 3 panels according to whether their expression is triggered by (A) PERK, (B) IRE1, or (C) ATF6 pathway signaling. Data were subjected to statistical analysis by two-tailed Student's t-tests. * $p < 0.05$; ** $p < 0.01$; *** $p < 0.001$; **** $p < 0.0001$; ns, not significant. Data are presented as means ± SD.

The data in Figure 21 indicate that all 3 UPR pathways were substantially activated in DUB-mut- and WT-MHV-infected cells but relatively minimally activated in EndoU-mut-infected cells relative to mock at 12 hpi. Two genes—Edem1 and GRP94/Hsp90b1—were not statistically significantly upregulated at all in EndoU-mut-infected cells relative to mock, suggesting an overall reduced activation of the UPR pathways by the EndoU-mut-MHV virus compared with the other two viruses. As other groups have previously shown, the apparent activation of these pathways in DUB-mut- and WT-MHV-infected cells was not associated with impaired replication of the viruses, as illustrated in Figure 11, suggesting that MHV—and perhaps other CoVs—has evolved to evade and/or suppress UPR-mediated antiviral activity, including UPR-induced apoptosis (Raaben *et al*. 2007; Bechill *et al*. 2008; Irigoyen *et al*. 2018). Indeed, it has been reported that several SARS-CoV-encoded proteins and at least one MERS-CoV-encoded protein antagonize the ER stress response during infection, indicating that coronaviruses are capable of shaping the UPR to their own benefit (DeDiego *et al*. 2011; Rabouw *et al*. 2016).

It is an intriguing possibility that the results of our RNA-seq experiments in DUB-mut- and WT-MHV-infected BMDMs, which revealed robust expression of nearly 2,900 host genes in response to infection, might be explained at least in part by the ER stress-triggered UPR. If, for example, the infection prompted the UPR, as has been well documented, it is possible that the outcome of UPR pathway signaling led to the activation of NF-κB and the downstream expression of NF-κB-induced inflammatory genes all while evading the initiation of apoptosis, as has also been demonstrated during CoV infections. In light of the results of our qRT-PCR experiments in Figure 12, which revealed that massive amounts of viral N gene transcript accumulated as early as 6 hpi during DUB-mut- and WT-MHV infection, a virus-induced wave of ER stress and the subsequent activation of the UPR would not be unusual. By activating the UPR, the cell's response to this ER stress would have the potential to produce potently pro-inflammatory macrophages *via* NF-κB-mediated gene expression. Prevented from undergoing apoptosis due to virus-encoded antagonists like nsp15-EndoU, these inflammatory macrophages might then contribute to the development of severe inflammatory coronaviral disease, in line with what has been reported in the literature (Cheung *et al*. 2005; Zhou *et al*. 2014; Channappanavar *et al*. 2016). Such a scenario could explain why the DUB-mut- and WT-MHV-infected cells in this study exhibited unimpeded viral replication coupled with dramatically increased expression of pro-inflammatory genes compared to mock-infected cells. Conversely, we hypothesize that the EndoU-mut-MHV-infected cells were rapidly driven toward an apoptotic phenotype early during infection due to the inability of the mutant virus to evade detection by the PKR and OAS/RNase L pathways. Early initiation of apoptosis would, in turn, preclude the buildup of significant ER stress and the subsequent activation of a broad inflammatory response to EndoU-mut-MHV infection akin to what was observed in DUB-mut- or WT-MHV-infected cells. This proposed dichotomy is illustrated in Figure 22. The extensive increase in expression of thousands of genes that our RNA-seq experiments revealed in DUB-mut- and WT-MHV-infected BMDMs likely cannot be attributed to ER stress-induced gene expression alone, but we speculate that the UPR played an important role in shaping at least part of the transcriptional profiles that we report here. At any rate, although additional work is required to fully elucidate the mechanism(s) that underlie the patterns of gene expression that we observed in this study, it is remarkable that a single amino acid change in nsp15-EndoU—but not in nsp3-DUB—was sufficient to profoundly alter the fate of the virus and of EndoU-mut-MHV-infected BMDMs.

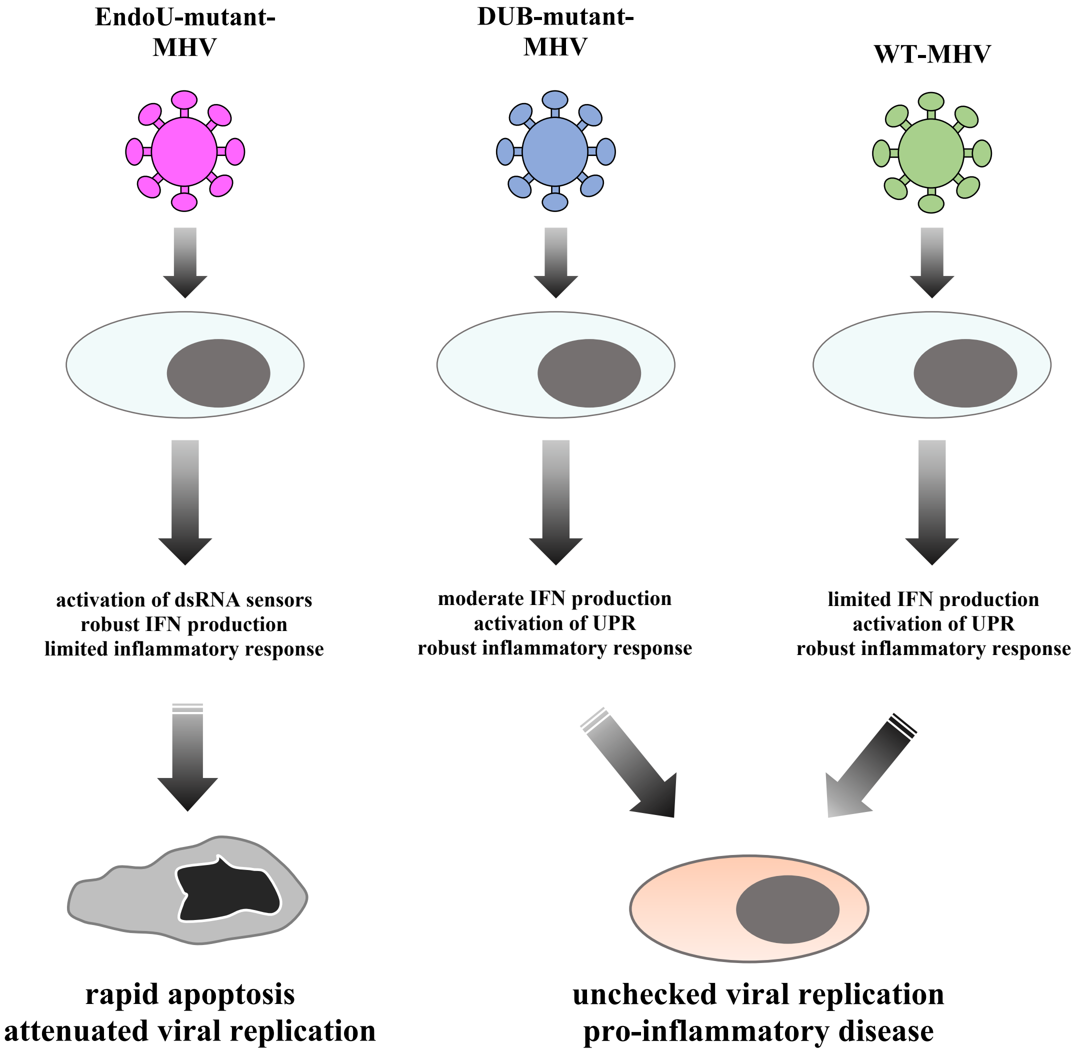

**Figure 22. Proposed Model of the Consequences of EndoU-mut-, DUB-mut-, and WT-MHV Infection in BMDMs.** Upon infection of a BMDM with EndoU-mut-MHV, host dsRNA sensors (including RIG-I, MDA5, PKR, and OAS/RNase L) are activated, resulting in robust transcription of type I IFN genes and rapid induction of apoptosis, the latter of which precludes the development of a potent inflammatory response. Viral replication is severely restricted in these apoptotic macrophages (shriveled grey/black cell) as early as 6 hpi. Although DUB-mut-MHV induces significantly higher type I IFN during infection than WT-MHV, infection with either DUB-mut- or WT-MHV results in the same outcome: accumulation of ER stress and subsequent activation of the UPR, which then likely contributes to the establishment of a robust NF-κB-mediated pro-inflammatory response. BMDMs infected with either of these viruses acquire a potently activated, inflammatory phenotype (orange cell), are unable to attenuate viral replication, and likely contribute to severe immunopathology *in vivo*.

## Targeting CoV-encoded IFN Antagonists for Rational Vaccine Design

Including nsp3-DUB and nsp15-EndoU, multiple coronavirus proteins—including both structural and nonstructural proteins—are reported to antagonize the innate immune response *in vitro* and/or *in vivo*. These include: nsp16-2'O MTase, nsp14-ExoN, nsp1, nsp7, E protein, N protein, M protein, SARS-CoV-ORF6, MERS-CoV-ORF3-5, MERS-CoV-4a, and others (Frieman *et al*. 2007; Frieman *et al*. 2009; DeDiego *et al*. 2014; Rabouw *et al*. 2016; Menachery, Galinski, *et al*. 2017; Menachery, Mitchell, *et al*. 2017; Menachery *et al*. 2018). The very nature of this ever-growing list suggests that CoVs might encode a *hierarchy* of innate immune antagonists that collectively target both shared and unique factors and pathways during infection. The data from this study and our previous work strongly indicate that nsp15-EndoU activity might sit at the top, or near the top, of such a hierarchy since it is evidently indispensable for successful infection both *in vitro* and *in vivo*, while nsp3-DUB might sit near the bottom rung of the ladder given that its activity does not appear to be similarly required (Deng *et al*. 2017; Deng *et al*. manuscript in preparation). Additionally, it is clear from the results of our RNA-seq experiments that the absence of nsp15-EndoU activity induced widespread changes in host gene expression relative to WT-MHV infection, whereas DUB-mut-MHV-infected cells elicited only a slightly altered transcriptional response compared to WT-MHV. These data also support the notion that nsp15-EndoU is a "master" regulator of the host response, whereas nsp3-DUB activity likely acts on a select number of targets to supplement nsp15-EndoU-mediated antagonism. Although additional work is required to clarify the roles of the many CoV-encoded innate immune antagonists relative to each other in the context of infection, that these viral proteins might work together in a hierarchical manner to achieve potent suppression of the antiviral response opens the door to new strategies for live-attenuated vaccine development.

### Combinatorial Approach to Generating IFN Antagonist-deficient CoV Vaccines.

Targeting viral IFN antagonists for the rational design of live-attenuated vaccines is an increasingly popular idea among virologists. In some cases, it is no longer merely an idea: recently-published reports have demonstrated remarkable efficacy of IFN antagonist-deficient MHV, MERS-CoV, SARS-CoV, and influenza A viruses as vaccine candidates (Deng *et al*. 2017; Menachery, Galinski, *et al.* 2017; Du *et al*. 2018; Menachery *et al*. 2018). Two of these studies reported using a combinatorial approach to generating live-attenuated, IFN-sensitive vaccine strains by disrupting multiple IFN antagonists within the same strain. Using a mouse-adapted SARS-CoV strain, Menachery *et al*. (2018) demonstrated that combining a mutation in nsp16-2'O MTase with an additional mutation in nsp14-ExoN resulted in robust protection from subsequent challenge with WT-SARS-CoV in mice without causing demonstrable pathogenesis. Similarly, Du *et al*. (2018) reported that combining 8 total "IFN-sensitive" mutations across the genome of the influenza A virus yielded a "hyper-IFN-sensitive (HIS)" vaccine strain that could be replicated to high titers *in vitro* but was markedly attenuated and induced appreciable humoral and cellular immune responses in mice (Du *et al*. 2018). Importantly, a combinatorial approach to rational vaccine design offers the advantage of reducing the likelihood of reversion to WT-like virulence, which is of particular concern when generating live-attenuated vaccine candidates.

The results of this study indicate that nsp15-EndoU and nsp3-DUB are attractive targets for the generation of a combination vaccine candidate. We observed that EndoU-mut-MHV was remarkably attenuated in macrophages, in line with our previously-published work *in vitro* and *in vivo*, and elicited a significantly diminished transcriptional response overall, including among groups of genes encoding potently pro-inflammatory and chemotactic proteins whose overexpression in the context of WT infection is thought to contribute to the severity of coronaviral disease pathology (Deng *et al*. 2017). On the other hand, replication of DUB-mut-MHV was not attenuated, despite inducing a considerably increased type I IFN response relative to WT-MHV infection, and differentially impacted the expression of only a few genes relative to the parental strain. Therefore, we intend to combine these two mutations in the near future to produce a vaccine candidate that, deficient in two of its IFN antagonism activities, is both safe and even more effective *in vivo* than the EndoU-mutant strain. Very preliminary data from our lab indicate that this approach might hold considerable promise, although substantial work remains to be completed. In conclusion, the work that we report here strongly suggests that combining mutations in nsp3-DUB and nsp15-EndoU with additional mutations in still other conserved CoV-encoded innate immune antagonists—perhaps nsp14-ExoN and nsp16-2'O-MTase, for example—might represent the most promising and universally-effective strategy yet for the generation of live-attenuated coronavirus vaccines.

# APPENDIX

# SUPPLEMENTAL TABLES

**Table S1. List of Gene Names in Order of Appearance in Figure 14.** Listed are the names of the 2,879 genes whose expression profiles are plotted in the heatmap in Figure 14. To preserve the order of the genes as they appear from top to bottom in Figure 14, this list should be read left to right, one row after another. In bold type after each gene name is the DESeq2-generated $\log_2$ fold-change value associated with the increase in expression of each gene in WT-MHV-infected BMDMs at 12 hpi compared with mock-infected cells.

| | Gene Name_**Log$_2$ Fold-change** | |
|---|---|---|
| Enthd1_**7.12** | Lysmd2_**7.04** | Adamts13_**4.45** |
| Gm21370_**5.76** | Stmn4_**7.11** | Adm_**7.34** |
| 1600002D24Rik_**5.04** | Apol9b_**9.66** | Cxcl9_**10.5** |
| 8030451A03Rik_**7.16** | Ifit3b_**9.85** | Ifit3_**8.73** |
| Tgtp2_**9.26** | Cxcl10_**11.33** | Ifit1_**8.01** |
| Mx2_**8.32** | Gm26667_**11.1** | Mxd1_**7.64** |
| Iigp1_**9.58** | Pydc3_**8.85** | Gm4955_**7.81** |
| Pydc4_**7.35** | Oasl1_**8.58** | Slfn4_**8.47** |
| Olfr56_**6.59** | Pyhin1_**6.59** | 2010002M12Rik_**6.73** |
| A530040E14Rik_**8.65** | Cxcl11_**12.87** | Cd69_**12.71** |
| Irg1_**11.13** | Ifit2_**9.47** | Gbp5_**9.66** |
| Tnfsf10_**9.03** | Cmpk2_**8.82** | Rsad2_**8.05** |
| Igtp_**6.74** | Gm12250_**6.29** | Ccl3_**10.12** |
| Irgm1_**6** | Ppm1k_**5.56** | Dll1_**11.52** |
| Tgtp1_**10.35** | Gm12185_**8.27** | Gm5431_**5.38** |
| Mx1_**9.12** | Irgm2_**6.57** | Slfn8_**5.58** |
| Trim21_**5.65** | BC147527_**7.94** | Usp18_**6.93** |
| Mitd1_**4.28** | Ppp1r15a_**7.83** | Themis2_**5.02** |
| Ifi205_**9.14** | Trim30d_**4.35** | Gm14446_**8.17** |
| Gm4951_**8.18** | Slfn1_**7.84** | Parp11_**4.1** |
| Ccl4_**6.93** | Ch25h_**6.26** | Nfxl1_**3.74** |
| 4930512H18Rik_**5.74** | AW011738_**5.97** | Xcr1_**5.59** |
| 5031414D18Rik_**3.88** | Gm10552_**7.02** | RP24-166N8.9_**6.97** |
| Ccl12_**8.09** | BC094916_**7.11** | Ifi47_**6.37** |
| Tpst1_**4** | RP23-364E18.2_**6.84** | Ppm1n_**4.71** |
| Nupr1_**3.77** | Bambi-ps1_**3.76** | Trex1_**4.56** |
| Gpr84_**5.03** | 2500002B13Rik_**3.03** | Gm11772_**5.81** |
| Rtp4_**4.98** | Sap30_**4.35** | Tlr11_**6.22** |
| Olfr1396_**5.43** | Chic1_**7.29** | Gstt4_**6.47** |
| Spta1_**7.16** | Hsh2d_**6.69** | Apol9a_**10.05** |
| Misp_**7.8** | AW112010_**8.59** | Fpr2_**7.59** |
| Socs1_**9.41** | Serpina3f_**9.72** | Gbp6_**10.29** |
| Enpp4_**7.63** | Ccl5_**10.9** | Gbp3_**8.19** |

Gbp2_**7.67**
Il6_**13.15**
Kcnh7_**7.42**
Ddx60_**6.28**
Klrk1_**9.17**
Isg20_**7.43**
Hdc_**7.87**
Slc25a22_**4.87**
Ifi203_**5.04**
E130102H24Rik_**5.48**
Plekha4_**6.49**
Irf7_**5.72**
Trim30c_**8.29**
Gpr18_**5.97**
Slfn5_**4.04**
Saa3_**7.35**
Rasgrp1_**11.42**
H2-Q5_**4.23**
Olfr231_**6.72**
Gm14569_**8.37**
Il18bp_**5.74**
Mov10_**4.48**
Fbn1_**9.49**
Slco3a1_**9.81**
Phf11d_**5.9**
Tmem67_**5.43**
Tnfaip8l3_**7.39**
Gm6904_**4.99**
Gm16094_**5.45**
1600014C10Rik_**4.76**
Gm15156_**4.15**
Nos2_**13.25**
Abtb2_**7.98**
Gm18853_**6.74**
Gm43164_**5.01**
Ptgs2_**10.46**
Gbp9_**6.85**
Ifih1_**7.1**
Peli1_**6.23**
Herc6_**5.73**
Il27_**10.91**
Tor3a_**5.01**
Ifi44_**7.64**
Gbp7_**6.75**
G530011O06Rik_**6.59**
Zbp1_**5.97**
Parp10_**5.14**
Xaf1_**4.68**
Gm11998_**5.71**
Apod_**6.6**
2010110E17Rik_**6.74**
Ccl8_**7.15**
Zeb1_**5.51**
Gm26797_**5.2**
Oasl2_**3.82**
Mmp14_**7.96**
H2-Q7_**4.57**
Vcan_**6.84**
Gm38048_**8.47**
Cp_**6.71**
Phf11a_**6.45**
Dnase1l3_**8.19**
Kif5c_**6.16**
Gm28347_**9.34**
Pml_**4.74**
Tmem229b_**3.44**
Cyp26c1_**6.15**
Dnah12_**5.84**
Il10_**6.68**
Pdcd1_**7.09**
Mycl_**11.54**
C3_**8.97**
Lpar1_**7.75**
Acoxl_**6.04**
Lrrc63_**6.49**
Gbp11_**10.4**
Whamm_**5.41**
Ddx58_**5.08**
Trafd1_**5.58**
Sp140_**5.3**
Il15_**6.94**
Nod1_**6.86**
Tlr3_**6.23**
Gm16340_**6.38**
Ms4a4c_**9.05**
Mnda_**5.24**
Trim30b_**5.67**
Gm15340_**6.26**
BC023105_**8.73**
Gm4841_**6.96**
Gm32200_**6.76**
Batf2_**5.95**
Oas1g_**4.54**
RP24-328P2.5_**4.94**
Trim30a_**3.82**
Hcar2_**7.81**
H2-Q6_**4.74**
Bmp10_**6.93**
Trp53i11_**6.47**
Fgl2_**7.98**
Phf11b_**5.76**
Lipg_**11.96**
Il23r_**9.63**
Slc6a4_**8.57**
Oprd1_**8.52**
Gm13348_**6.15**
Igsf9_**5.58**
Uba7_**4.04**
Foxf1_**7.69**
Rnf135_**4.16**
F3_**8.2**
Traf1_**8**
Il12b_**13.73**
Cd40_**9.11**
Unc80_**9.78**
Gca_**7.47**
Cd274_**9.32**
Parp9_**4.56**
Lhx2_**10.86**
Parp12_**5.09**

Il15ra_**7.08**
Tnfsf4_**11.62**
Csf1_**9.79**
Foxl2os_**7.49**
P2ry13_**7**
3110001I22Rik_**5.29**
Fndc3a_**4.62**
Cxcl16_**4.15**
Trmt61b_**3.98**
Ripk2_**5.04**
Neb_**7.82**
Gm18752_**6.78**
Nt5c3_**4.83**
Ifi35_**4.02**
Myd88_**3.58**
Ddx4_**6.02**
Ptprg_**6.99**
Il1a_**10.5**
Ccrl2_**9.31**
Gm11843_**7.51**
Csrnp1_**8.4**
Icam1_**6.84**
Edn1_**10.61**
H2-K2_**6.7**
Shisa3_**11.33**
Gfi1_**9.39**
Otor_**5.59**
mt-Rnr2_**3.91**
Socs3_**6.21**
Dusp8_**5.92**
Pde4b_**5.43**
Tnfsf18_**7.36**
Pou3f1_**10.64**
Zufsp_**6.42**
Ccnj_**3.88**
Stat2_**5.66**
Parp14_**6.03**
Rnf213_**5.32**
Txlnb_**3.52**
Cited2_**6.79**
Apobec3_**4.15**
Nox1_**8.59**
Arhgef3_**7.13**
Rapgef2_**6.05**
Aim2_**4.44**
Snx10_**3.45**
Trim12a_**4.72**
Aftph_**3.58**
A1cf_**5.92**
Tnn_**5.27**
Golga3_**3.07**
Itgb8_**6.3**
Mndal_**4.1**
Ifi204_**4.38**
Ogfr_**3.86**
Serpina3g_**7.92**
Gm18852_**7.29**
Sele_**11.33**
Vcam1_**10.63**
Clec4e_**5.95**
Nfkbie_**6.28**
Pim1_**7.68**
Nod2_**5.93**
5730508B09Rik_**4.9**
Csf2_**10.96**
Arl5c_**6.21**
C130026I21Rik_**6.57**
mt-Rnr1_**3.24**
Fas_**5.05**
Zc3h12c_**5.6**
Junb_**6.13**
Six1_**6.37**
Gbp4_**12.17**
Daxx_**6.79**
Gm8995_**6.07**
Znfx1_**5.02**
Ncoa7_**4.61**
Gm1966_**6.19**
Gm4070_**5.67**
Tagap_**5.54**
Gm13889_**10.82**
Mafk_**5.29**
Fscn1_**8.94**
Tiparp_**5.95**
Plcl2_**4.79**
Cd200_**9.27**
Katna1_**3.66**
Rnf114_**3.48**
4933430I17Rik_**5.09**
Gm37191_**4.83**
Gm13822_**6.91**
Fam26f_**8.51**
Tmem171_**4.76**
Ube2l6_**3.67**
Bco2_**3.64**
Lck_**3.1**
Atf3_**5.49**
H2-M2_**8.87**
Gem_**9.6**
Gadd45b_**9.04**
Tnfaip3_**7.66**
Birc3_**4.92**
Stat1_**5.5**
Slfn2_**4.61**
Fnbp1l_**4.04**
Dusp2_**6.8**
Gm8641_**4.61**
Adora2a_**10.72**
Rgs16_**4.85**
Nlrp3_**5.57**
Tlr2_**4.81**
Bmp2_**7.6**
Otud1_**8.07**
Mthfr_**5.49**
Dtx3l_**5.86**
Setdb2_**6.12**
Cers6_**5.61**
Tnfsf15_**10.36**
Gvin1_**5.62**
Il10ra_**3.46**

Nxpe3_**8.19**
Zbtb5_**6.09**
Ikzf1_**4.98**
Icosl_**6.29**
Ccnl1_**3.85**
Samd9l_**5.42**
Ccng2_**5.43**
Sgk1_**4.4**
AI607873_**4.44**
Vcpip1_**3.9**
Zmynd15_**5.64**
Gm17017_**4.95**
Gm2065_**6.05**
6530409C15Rik_**3.97**
Gm10522_**3.81**
Gm12764_**5.22**
Gm14963_**4.35**
A930024N18Rik_**6.37**
Phf11c_**5.71**
Fam84b_**4.16**
Gsap_**3.56**
Cdkl5_**3.53**
Rgs2_**3.85**
Fam110b_**3.49**
Iqsec2_**3.17**
Il1b_**9.39**
Zfp36_**5.75**
Clec2d_**6.29**
Nfkbiz_**9.06**
Tifa_**4.52**
Gm5970_**8.39**
Slfn9_**4.7**
Rrad_**3.57**
Slc25a25_**3.28**
Vaultrc5_**5.05**
Igsf6_**3.28**
Gm3086_**3.74**
Zfp819_**4.54**
RP23-23C4.4_**4.05**
Kcna4_**3.86**
Hmgb1-ps5_**5.73**
2810474O19Rik_**5.87**
Slfn3_**5.26**
Rel_**6.12**
Eif2ak2_**4.66**
Adar_**3.83**
Fam46a_**5.84**
Dcp2_**4.28**
Etnk1_**4.69**
9930111J21Rik1_**5.33**
Tlr1_**4.07**
Hs3st3a1_**5.22**
Gm4759_**4.5**
Ikbke_**2.71**
4933417C20Rik_**5.22**
Ms4a4d_**4.13**
Gm11419_**2.65**
Gm11216_**6.1**
Pla2g4c_**5.19**
Trim34a_**4.25**
Lipe_**3.36**
Bcl2a1a_**8.37**
Amn1_**3.36**
Crlf3_**3.07**
Ankle2_**2.57**
Map3k8_**7.12**
Cxcl2_**9.95**
5430427O19Rik_**5.48**
Nfkbia_**4.61**
Tnfsf9_**5.94**
Gm12188_**6.32**
RP23-253G12.9_**5.23**
Dusp1_**3.93**
Gm16161_**5.04**
RP23-353L10.2_**4.66**
AC117682.1_**5.51**
RP23-50I16.3_**2.88**
Flt4_**5.65**
RP23-454P8.3_**4.87**
Gm9089_**5.84**
Ier5_**5.41**
Rasgef1b_**5.95**
Plk2_**8.2**
Birc2_**5.01**
Helz2_**6.2**
Oas2_**4.18**
Fam53c_**4.6**
Papd7_**4.85**
N4bp1_**4.14**
9930111J21Rik2_**4.72**
Lrch1_**3.83**
4930405A21Rik_**4.48**
Gm15990_**5.26**
Amica1_**4.58**
Adamts4_**5.26**
Gm7019_**5.12**
BC034090_**4.16**
Rnf152_**6.63**
Rin2_**3.16**
Irf2_**3.55**
Cacna2d1_**4.64**
Rnd3_**6.98**
Irf9_**3.53**
Trim14_**3.31**
4930486L24Rik_**3.07**
Cxcl1_**10.21**
Irf1_**8.11**
Tnf_**9.35**
Pnrc1_**5.55**
Prdm1_**4.97**
Gdap10_**6.16**
Art2a-ps_**5.07**
Nfkbid_**4.05**
Gm20470_**4.29**
Gm20496_**4.36**
Gm26648_**4.39**
Dhx58os_**3.9**
Gm7804_**4.53**
Cxcl3_**7.33**
Marcksl1_**5.09**

Il23a_**4.93**
Slc2a6_**4.13**
Egr2_**4.49**
Efna2_**3.47**
Efcab3_**7.33**
Ank3_**3.86**
Ttll2_**5.58**
Gm16589_**3.85**
Pla1a_**5.11**
Gm14086_**4.92**
Kcnab1_**6.35**
Slc17a8_**6.49**
Pappa2_**5.65**
Cysltr2_**4.27**
Bcl9_**4.17**
Zfp811_**6.62**
Ccnd2_**4.74**
Agrn_**3.88**
Fat4_**7.29**
Ptgs2os2_**6.09**
En2_**7.55**
Bend7_**6.77**
Trim72_**6.52**
Atp10a_**5.09**
Fam208b_**4.38**
Nfil3_**4.42**
Tlk2_**4.41**
Dnaja2_**4.31**
Plekhf2_**3.98**
Acsl1_**6.31**
Usp42_**4.09**
Socs7_**4.47**
Apaf1_**3.68**
Mtus1_**5.06**
Morc3_**3.52**
Usp25_**4.04**
Zcchc2_**3.77**
Nfkb1_**4.18**
Zc3h7a_**4.22**
4930453N24Rik_**3.35**

Gm26885_**3.48**
Tslp_**4.9**
E230013L22Rik_**3.21**
Elovl2_**4.41**
Slc1a3_**6.49**
Med12l_**6.52**
Gm37131_**5.2**
Spats2l_**7.84**
Col19a1_**4.96**
Kalrn_**7.32**
Gm14490_**7.16**
Axl_**4.08**
Gata3_**6.34**
Arel1_**3.51**
A230050P20Rik_**3.74**
Rnf31_**4.47**
Xkr8_**3.74**
Hrh2_**4.63**
Adamts6_**6.3**
Gbp10_**6.5**
Asap3_**7.17**
Slc28a2_**6.33**
Parp8_**5.05**
Apol10b_**7.51**
Usp12_**4.5**
Mier3_**4.2**
Il13ra1_**5.03**
Tdrd7_**3.95**
1110032F04Rik_**8.13**
Dcbld2_**5.87**
Zfp319_**4.05**
Rnf139_**3.68**
Whsc1l1_**3.54**
Ascc3_**4.45**
Hinfp_**4.2**
Vps54_**4.1**
Sdr39u1_**3.29**
Zfp281_**4.07**
Tle4_**3.49**
Tmem132e_**6.75**

Gm18342_**4.9**
Sod2_**2.93**
Rab20_**3.72**
Pde10a_**5.27**
Col27a1_**5.19**
Alpk2_**7.13**
2310031A07Rik_**5.63**
Macc1_**6.77**
Zfhx4_**6.74**
Plagl1_**7.55**
Pnpt1_**3.11**
Ocln_**7.87**
Kynu_**7.22**
Nsmaf_**2.79**
Gbp8_**4.63**
1810019N24Rik_**5.17**
Grm5_**3.96**
Atp13a4_**8.85**
Ehd3_**5.84**
Mfsd7a_**5.36**
Il33_**6.5**
Mtmr7_**5.18**
Tmcc3_**4.46**
Zic5_**4.82**
Dennd1b_**3.78**
Azi2_**4.21**
Fbxw17_**3.56**
Gcnt2_**4.18**
Lad1_**9.55**
Etv3_**4.38**
Fzd5_**5.27**
Arrdc4_**5.08**
Sema6a_**6.31**
Mgat4a_**4.67**
Phip_**4.76**
Larp1_**3.63**
D16Ertd472e_**5.94**
Ptpn2_**3.83**
Wdr43_**2.99**
Itga4_**3.67**

Naa25_**3.11**
Zfp513_**2.93**
Gm12928_**4.25**
Slc15a2_**4.09**
Ext1_**4.32**
Jarid2_**4.35**
Aida_**3.58**
Cds1_**3.56**
Rhoh_**4.09**
Gm5345_**3.65**
Gm38297_**8.49**
Klf8_**5.79**
Ido2_**4.71**
Vrk2_**3.71**
Tcp10b_**3.45**
Stx16_**2.49**
Gm11999_**6.39**
Nudt13_**2.61**
Ppa1_**4.02**
Omp_**3.67**
RP23-167C5.1_**6.3**
Ifnlr1_**5.28**
Trim36_**5.19**
Serpine1_**6.71**
Stk38l_**4.7**
Ppap2b_**4.77**
Eda2r_**4.36**
Slc25a37_**3.17**
Dusp10_**4.03**
Ppp4r2_**4.04**
Ciita_**6.85**
Gm26809_**4.78**
Tpbg_**7.25**
Fam89a_**9.45**
Klf6_**5.53**
Nfkbib_**4.5**
Gm6377_**5.15**
Rab30_**4.88**
Kpna3_**4.05**
Trim26_**3.3**
Slc7a2_**5.78**
Adrbk2_**3.57**
Sesn3_**4.64**
Tanc2_**5.39**
Flnb_**4.74**
Sirt1_**5.34**
Cpeb3_**4.57**
Tox4_**3.01**
Minpp1_**3.26**
Sema4d_**2.48**
Inhba_**8.15**
Mb21d2_**5.22**
Sgk3_**2.92**
Sco1_**4.12**
F11r_**2.85**
RP23-114F4.1_**5.07**
Trpm6_**6.1**
Fam46d_**7.55**
Hmgn3_**3.94**
Bfar_**3.07**
Htra1_**5.51**
Nr3c2_**7.59**
Zfp382_**5.46**
Swap70_**5.08**
3110043O21Rik_**4.88**
Dse_**3.55**
Etv6_**3.75**
Rras2_**4.94**
Scube2_**5.01**
Dyrk2_**4.1**
Gm5530_**4.72**
Foxp4_**4.09**
Cish_**6.71**
Jak2_**5.96**
Tank_**4.8**
Plscr1_**4.97**
Zfp800_**4.92**
Nfkb2_**3.74**
Cflar_**4.5**
Lrch3_**2.85**
Ptchd1_**4.6**
Zfp691_**2.66**
Jdp2_**5.53**
Phlpp1_**4.64**
Kdr_**4.5**
Slc15a3_**3.25**
Stxbp3_**3.96**
Rufy3_**3.27**
Tlr6_**3.03**
Krt16_**9.99**
Enah_**5.86**
Tcp11x2_**5.98**
Traf2_**3.81**
Cenpj_**3**
Stard5_**2.75**
Gm20125_**4.99**
Pigv_**3.99**
Stard3_**2.92**
Klra2_**3.57**
Olfr99_**4.04**
Clca1_**7.57**
Tet2_**5.35**
Skil_**4.61**
Dusp16_**5.53**
Tgif1_**3.85**
Gm3555_**4.75**
Spred1_**3.08**
Lcp2_**3.83**
Zfp263_**3.42**
Nova1_**3.82**
Rab11fip1_**5.06**
Car2_**7.74**
Lnx1_**6.46**
Adhfe1_**4.83**
Rgs1_**5.64**
Snn_**5.63**
Irak2_**3.63**
Clic4_**3.95**
Zc3hav1_**3.6**
Rab9_**3.55**

Sav1_**3.35**
H3f3b_**3.29**
Cdkn1a_**3.82**
Oser1_**3.42**
Mcl1_**3.22**
Prr5l_**3.95**
RP23-250D22.2_**5.68**
Marcks_**4.13**
Arid5b_**5.92**
Lamc2_**4.16**
Zhx2_**4.7**
Adam17_**3.06**
Fam102b_**3.97**
Gm8388_**3.5**
Synpo2_**3.31**
Gm14208_**2.73**
Ly75_**5.13**
Ep400_**4.07**
Nup98_**4.12**
Dock10_**3.42**
Xrn1_**3.3**
Fnbp4_**3.4**
Plagl2_**3.46**
Tmem170b_**3.41**
Smg7_**3.27**
Ccnl2_**2.94**
Med13l_**3.18**
Ccl22_**7.85**
Col11a2_**3.82**
Gm4992_**4.09**
Gm614_**5.25**
Adgre4_**3.35**
Mefv_**3.55**
RP23-41J13.2_**3.57**
1700055D18Rik_**3.86**
Arid5a_**5.6**
4930430E12Rik_**4.51**
Casp4_**3.86**
Klrg2_**3.88**
Siglecg_**4.99**
Cd83_**6.4**
Cilp2_**5.08**
Nck1_**3.68**
Gpr132_**4.27**
Rasip1_**3.76**
Taf7_**3.07**
Gm5828_**3.6**
D1Ertd622e_**3.77**
Gm11842_**4.46**
Gm7967_**4.05**
Mdm2_**4.8**
Hivep1_**4.09**
Bach1_**3.53**
Gm8902_**3.79**
Gm12664_**3.73**
Fndc7_**4.32**
Mycbp2_**4.23**
Ubr4_**3.7**
Dock4_**3.85**
Zcchc11_**3.64**
Ranbp2_**3.26**
Rbm7_**3.18**
Ankrd17_**3.76**
Atxn7l1_**3.61**
Khnyn_**3.56**
Chd2_**4.43**
Smyd1_**4.01**
5930403N24Rik_**3.64**
Psd_**3.24**
Alox12_**2.51**
Gm7357_**4.97**
Piwil4_**4.67**
Asprv1_**5.28**
Gm16181_**5.14**
Gm12216_**4.43**
Stx11_**5.62**
Ccl7_**4.09**
Nampt_**3.11**
Fst_**6.22**
Nap1l2_**4.09**
Tnfaip2_**5.11**
Mob3c_**3.92**
Relb_**4.44**
Cdk5r1_**5.07**
Bcl2a1d_**4.74**
Gm6485_**3.66**
Ier3_**5.43**
Gm13584_**5.75**
Srgap2_**2.78**
Creb5_**4.59**
Malt1_**5.34**
Prrg4_**4.05**
Frmd4a_**2.36**
Gm26584_**4.24**
Usp17le_**3.74**
Il17rd_**7.38**
Med13_**4.18**
Dync1h1_**3.33**
Chd1_**3.93**
Ralgapa2_**3.36**
Wdr37_**3.95**
Tcf4_**3.47**
Mier1_**3.86**
Tgs1_**3.54**
Synj1_**2.97**
Trps1_**3.13**
Bcl2a1c_**4.88**
H2-Eb1_**4**
Vasp_**2.85**
Shd_**5.46**
Il20rb_**3.59**
Chst15_**5.98**
4930509G22Rik_**4.45**
Tex12_**4.44**
Cldn23_**3.99**
Rnf19b_**4.03**
Ccl2_**3.81**
Gm16026_**5.06**
Slc39a2_**5.19**
Pik3ip1_**5.51**

Gm9869_**5.95**
Cfb_**6.01**
AA467197_**5.42**
A530032D15Rik_**6.14**
Pvrl4_**4.07**
Tapbp_**3.81**
Dram1_**3.64**
Clic5_**9.26**
Lacc1_**4.42**
Car13_**4.05**
Pcgf5_**5.12**
Prpf38a_**4.3**
Mlkl_**3.97**
Rbm43_**3.56**
Ythdf1_**2.98**
Dlx1_**5.88**
Gm37787_**4.31**
Oas1a_**3.41**
Insl6_**3.55**
Gm15337_**4.31**
Ass1_**4.25**
Slamf8_**4.36**
Ms4a4b_**3.86**
Slamf9_**3.26**
Keap1_**2.44**
Casp1_**3.1**
Treml2_**3.35**
Il18_**3.38**
Psme2b_**3.16**
Gm16464_**3.02**
Pla2g16_**3.07**
Oas3_**2.43**
H2-Q2_**2.35**
Yipf7_**2.94**
Gm13495_**3.58**
Gm6264_**2.23**
Cndp1_**4.52**
Gm16425_**3.69**
Enam_**4.22**
RP23-454P8.1_**4.44**
F830016B08Rik_**6.15**
Tnfsf8_**3.55**
Tap1_**4.63**
Akap12_**5.81**
Asb13_**4.21**
Dhx58_**3.94**
Samhd1_**3.86**
Tapbpl_**4.46**
Fzd1_**4.04**
Tor1aip1_**3.25**
Gnb4_**4.97**
Max_**3.18**
Rmdn3_**3.5**
Trim12c_**3.77**
Tmem178_**5.86**
P2ry14_**3.91**
Sh2d6_**4.36**
Sp110_**3.64**
Slc31a2_**2.67**
Cdhr4_**5.51**
Ms4a6c_**2.75**
Hmcn2_**5.17**
Tap2_**3.75**
Sp100_**3.23**
Sepw1_**3.53**
1110038F14Rik_**3.04**
Ogfrl1_**2.83**
Prdx5_**3.21**
Rtn1_**3.78**
Pla2r1_**3.57**
Dck_**2.58**
Il7_**2.6**
AI837181_**2.51**
Abcc8_**5.54**
Ankmy1_**4.56**
Mid1_**3.39**
Gm7160_**2.6**
Gm11626_**2.94**
Orm3_**3.17**
Grhl2_**5.06**
Amotl2_**4.23**
Nlrc5_**3.97**
Angpt1_**7.34**
Mmp25_**7.35**
Usb1_**4.19**
Kmo_**5.78**
Zbtb10_**5.15**
Slamf7_**5.34**
Mtmr14_**4.52**
Tor1aip2_**2.94**
Gch1_**4.1**
Il1rn_**4.61**
2310001H17Rik_**3.48**
Ccdc25_**3.33**
Il2rg_**3.42**
Rap2c_**2.69**
Nmi_**3.87**
Epsti1_**3.46**
Ccdc88b_**2.72**
Gm5424_**4.26**
AI118078_**3.71**
Gm4117_**3.46**
Scimp_**4.65**
Il12rb1_**5.99**
Ccdc173_**3.7**
Dusp28_**3.2**
Lrrc4_**3.19**
Psme2_**3.04**
Gdf11_**5.76**
Cnksr1_**3.8**
Fcgr4_**2.69**
Ptpro_**2.33**
Mroh8_**4.83**
Slc13a1_**4.48**
Gm20661_**4.3**
Gm15726_**3.59**
Tra2a_**3.16**
4930440I19Rik_**3.89**
Rgs4_**2.73**
Mfsd2a_**4.71**

Sh3d21_**4.64**
Gm15694_**3.6**
Gm21188_**4.27**
Adamts1_**3.68**
Spry1_**4.77**
Hivep3_**3.2**
Ppp2r5a_**2.53**
Dnajb6_**2.68**
4930594C11Rik_**3.67**
Jag1_**2.47**
A3galt2_**4.75**
Gpr141_**2.19**
Pde6b_**2.31**
Gm10425_**3.53**
Spic_**4.13**
Nbea_**4.19**
Clec9a_**3.17**
Zfp456_**2.34**
Gm11274_**2.97**
Trac_**4.6**
Crp_**4.87**
RP23-213N8.1_**2.83**
Gm27019_**3.99**
Atp5l-ps2_**3.33**
Kdm6bos_**2.73**
Gm28373_**3.7**
Gm17193_**3.96**
Gm15821_**4.96**
Gm12039_**4.22**
Ptger4_**4.19**
Cep350_**4.06**
Gm37285_**4.97**
Phf21a_**3.84**
Slx4ip_**2.71**
Frmd4b_**2.92**
Nrip1_**2.74**
Gm6679_**3.46**
Lcor_**3.83**
Zfp62_**3.18**
Pik3r3_**2.79**

Bcl2a1b_**3.8**
Cd247_**5.43**
Gm14023_**3.22**
9430034N14Rik_**3.86**
Gm21378_**4.09**
Arg2_**4.53**
Jam2_**2.5**
Gm8221_**3.71**
Gm11874_**2.81**
A630072M18Rik_**3.74**
Tssk3_**3.59**
Mark1_**2.88**
Sh2d4a_**5.13**
1110002J07Rik_**2.34**
Gm12818_**3.02**
Gm1123_**3.84**
Plat_**2.81**
Mocs1_**2.31**
Unc93a_**5.48**
H2-Eb2_**3.19**
Akap2_**4.08**
Ccr7_**2.83**
Dscaml1_**4.42**
Gm10851_**3.01**
Tfap2a_**4.04**
Map1b_**3.65**
Gm38375_**3.43**
Spata5l1_**3.88**
Tmem88_**2.94**
Pim3_**3.94**
Mb21d1_**3.57**
Gm5117_**3.46**
Dapp1_**3.64**
Zc3h12a_**4.2**
Atp10d_**3.3**
Susd6_**2.82**
Mob3b_**3.02**
Zbtb39_**3.29**
Ppfibp1_**2.8**
Zfp654_**2.67**

Gm12902_**3.42**
Exoc3l4_**4.6**
Pilra_**2.57**
Tmem200b_**6.34**
Trim13_**2.8**
Gm9845_**3.57**
Gm13414_**3.19**
Zfp429_**2.77**
Tcea1_**2.11**
Gm21857_**2.94**
Gm15753_**3.26**
1700065D16Rik_**2.81**
Mthfr-ps1_**3.75**
RP24-543J12.4_**4.97**
Txk_**4.31**
Gm12551_**2.82**
Flrt3_**2.39**
RP23-316M11.10_**3.18**
Gm13571_**6.24**
Hoxd1_**6.49**
Slamf1_**5.04**
Gm36933_**2.6**
Ncan_**3.01**
Clca2_**3.12**
Gm6039_**4.04**
Cep85l_**3.92**
RP23-153H17.5_**2.59**
Pilrb1_**3.49**
Gm13833_**3.77**
Gm16973_**3.9**
Unk_**3.09**
Bmper_**4.34**
Gm16712_**3.8**
B630005N14Rik_**3.66**
Zfp949_**2.79**
Pikfyve_**2.59**
Kansl1_**2.99**
Epc1_**3.59**
Ccnt2_**2.85**
Zfp260_**2.54**

Luzp1_**2.51**
Rfwd2_**2.77**
4932442E05Rik_**3.34**
Zfp507_**2.77**
Mdm4-ps_**3**
Gm37718_**2.79**
Arid4a_**3.03**
Maml2_**3.06**
Gm29438_**2.6**
Olfr755-ps1_**3.35**
RP23-461P7.1_**3.23**
Mir7679_**3.37**
AC084073.1_**2.91**
Pth2r_**3.5**
Gm2541_**3.7**
Irx5_**2.59**
Iglon5_**3.62**
Ptpn13_**5.92**
Slc23a3_**2.94**
Gm38130_**2.84**
RP24-445F15.1_**5.61**
Tfcp2l1_**4.24**
Atxn7l1os2_**3.88**
Abcb11_**3.83**
Coch_**5.77**
Flt1_**3.78**
Cacnb2_**7.3**
Nrxn3_**5.79**
Gnrhr_**6.2**
Chrm3_**6.68**
Mttp_**3.43**
Slc27a2_**3.97**
Itk_**5.4**
Gm11992_**5.66**
Gm16038_**5.37**
Gm37417_**6.68**
Gad2_**4.64**
Prom1_**6.46**
1700017D01Rik_**5.12**
Fam184a_**4.46**

Zeb2_**2.52**
Ints12_**2.31**
Rassf4_**2.35**
Filip1l_**2.72**
Plekho2_**2.98**
Fmnl2_**5.85**
Trmt1l_**2.93**
Ikzf2_**2.93**
Gm5815_**2.32**
mmu-mir-7682_**4.99**
Gm27167_**2.39**
RP23-162P5.1_**2.89**
Gm27197_**2.84**
Sema3a_**3.28**
Dtwd1_**2.46**
Gm4852_**2.63**
Lrrc32_**4.24**
Gm10717_**3.34**
Gbgt1_**3.77**
Gm27676_**2.83**
Pdzd2_**3.38**
Dnah7a_**5.28**
Ubd_**4.32**
Gm13986_**3**
Zswim5_**7.71**
Col6a1_**4.56**
Asb11_**6.28**
Tacr2_**6.81**
Bambi_**4.33**
Gm15433_**4.03**
Adgrb1_**5.66**
Gm6899_**3.73**
Gm609_**5.16**
Map2_**5.37**
Prm1_**4.98**
Itga2_**4.75**
A630012P03Rik_**7.55**
1700011M02Rik_**4.02**
Tead4_**5.57**
Spry4_**3.18**

Gm6206_**2.96**
D130040H23Rik_**3.88**
WI1-1749A12.1_**3.25**
Ell2_**2.36**
Gm25405_**2.82**
Lrrc16a_**3.37**
Zscan29_**2.6**
A530072M11Rik_**2.58**
Gm37534_**2.83**
Nfib_**4.51**
Gm12737_**3.21**
Il1f9_**2.87**
C1s1_**2.79**
RP23-387P23.7_**2.99**
Rgs13_**3.23**
RP23-173N16.5_**3.6**
Gm17200_**3.83**
Pls1_**3.42**
Tepp_**2.49**
Gm15728_**4.18**
Kctd19_**3.71**
Stox2_**4.84**
Gpr50_**4.17**
Ms4a8a_**5.37**
Inhbb_**6.69**
Adgrv1_**7.29**
Nkx3-2_**5.71**
RP23-194K16.1_**5.29**
Ak9_**7.09**
C9_**5.18**
Gm13713_**6.35**
Dnah5_**6.99**
Ptx3_**3.64**
Lcn2_**5.15**
Meikin_**6.13**
Gm17473_**4.8**
Dmrtc1a_**6.86**
Aplnr_**5.16**
Pcp4_**3.41**
Tspan15_**7.09**

Frmd5_**5.92**
Gm37711_**5.89**
Enpp3_**5.02**
Csrnp3_**6.56**
Dcn_**4.03**
Unc5c_**3.84**
Hrasls5_**2.74**
Gm8369_**4.13**
Tnc_**4.93**
Prss56_**3.85**
B230307C23Rik_**3.05**
Fam71d_**3.75**
Lrrc55_**3.22**
Mustn1_**5.07**
Slc3a2_**2.87**
Il12a_**7.21**
Afap1l2_**6.32**
Olfr461_**5.12**
Tbx20_**4.24**
Gpc5_**4.3**
4930412F09Rik_**2.98**
Wt1_**4.64**
Gm2389_**2.97**
Dlgap2_**4.91**
Dsp_**4.8**
Gm10634_**4.43**
Mroh2b_**3.94**
9230109A22Rik_**5.26**
Htr7_**3.1**
P3h2_**4.62**
Grid2_**2.99**
Ptgs2os_**6.74**
4930512M02Rik_**4.62**
Gabrb2_**4.52**
Spop_**2.69**
Prpf4_**2.59**
A930035D04Rik_**2.87**
Diras2_**5.58**
Rnf225_**4.18**
Tceb3_**2.09**

Gm15987_**4.53**
Apol6_**3.97**
Gm15056_**4.02**
Gm37560_**4.68**
Pax4_**7.89**
Gm37181_**3.55**
4930579C12Rik_**4.24**
Tmem86b_**3.46**
Gm8979_**4.13**
Myo18b_**3.1**
Fam19a2_**3.73**
4931429I11Rik_**3.24**
Gm8773_**4.42**
Ghr_**5.07**
Gm9847_**4.9**
Cldn1_**3.68**
Cnr1_**5.92**
Dtna_**4.71**
C230034O21Rik_**4.16**
Maob_**4.2**
Etnk2_**4.58**
Mkx_**3.68**
Oxct2b_**6.02**
Clvs1_**6.07**
Pou3f2_**4.6**
Gxylt2_**3.79**
Lrrc6_**3.9**
Steap4_**4.66**
Arhgef28_**3.57**
Mme_**4.3**
Olfr1372-ps1_**3.05**
4930435H24Rik_**5.64**
Epb4.1l4b_**3.9**
Phf6_**2.82**
Asf1a_**2.99**
Gm5406_**2.95**
1700025C18Rik_**3.38**
Slc6a19_**6.6**
Tyk2_**2.78**
Asgr2_**3.63**

Gm14199_**5.69**
Slc1a1_**4.87**
Pcdh17_**5.05**
Lman1l_**3.73**
Gm24944_**4.19**
Nav3_**3.29**
Gm3764_**4**
Pou4f1_**6.03**
Col5a3_**4.32**
Gm7135_**2.66**
Dthd1_**3.41**
Gm11414_**3.25**
Gm38386_**3.59**
Ccdc149_**4.76**
Ido1_**6.18**
Gm16578_**3.52**
Il5ra_**4.32**
Gm9992_**4.74**
Gm2396_**5.2**
Gm37432_**3.01**
2810404F17Rik_**4.05**
Csn1s1_**2.8**
Lypd6_**5.7**
Galnt13_**2.73**
Tdgf1-ps1_**4.53**
Foxa2_**4.02**
Slc6a1_**3.54**
Gm2617_**4.45**
Gm10271_**3.68**
Zfp521_**2.95**
Pdzrn3_**3.59**
Gata4_**5.61**
Gm28114_**6.16**
Elf1_**3.32**
Etohd2_**2.78**
Sdcbp2_**5.09**
Arf4os_**3.18**
Pcsk1_**5.93**
Abcb1a_**3.03**
Sfmbt2_**4.4**

Htra4_**5.37**
Serpinb9_**3.77**
Zfp212_**3.82**
Cdyl2_**3.67**
Ppp6r1_**2.67**
Crim1_**3.8**
G3bp2_**2.81**
Pdss1_**3.1**
Tjp1_**4.56**
Usp15_**3.16**
Tmem209_**2.58**
Crbn_**2.73**
Casp8_**2.37**
Tmem140_**2.68**
Shf_**2.46**
Gm17040_**3.43**
RP24-142B15.8_**3.28**
Polr2g_**3.03**
Gm7609_**2.91**
Irx2_**3.13**
Nlrp4d_**2.72**
Tekt3_**2.36**
B3gnt2_**2.26**
Ralgds_**2.66**
Rasa4_**3.11**
Cd47_**2.69**
Carhsp1_**3.43**
Cd200r4_**3.5**
Tmem184b_**2.7**
Abcg1_**3.85**
Nfix_**2.7**
Cybb_**2.81**
Ube2e2_**3.08**
Clcf1_**6.06**
Sat1_**2.77**
Pde7b_**3.16**
Gm14005_**2.33**
Phc2_**3.21**
Pdcd10_**2.75**
Sumo1_**2.57**

Grap2_**5.9**
Sec24b_**4.09**
Mcm9_**4.23**
Mtcp1_**2.74**
Rcn1_**3.76**
Sgcb_**2.88**
Ppap2a_**3.07**
Gypc_**3.08**
Nlrp10_**4.19**
Cul2_**2.94**
Uaca_**2.49**
Coa5_**2.43**
Diap2_**2.72**
Osmr_**3.88**
Abcg4_**4.71**
Ache_**3.71**
C4b_**2.55**
Caml_**2.38**
Tdrp_**3.36**
Frmd3_**3.1**
2810407A14Rik_**2.78**
Letm2_**2.4**
4930539E08Rik_**3.24**
Cobll1_**2.76**
Upp1_**6.89**
Glipr2_**3.26**
Lmo4_**3.06**
Nub1_**2.83**
D17Wsu92e_**2.51**
Triobp_**3.15**
Otud5_**2.51**
Clcn7_**3.22**
Lif_**3.89**
Mapkapk2_**3.22**
Src_**3.59**
H2-Q4_**2.69**
Ets2_**2.98**
Tmem243_**3.2**
Papd4_**2.83**
Psmd10_**2.3**

Akap7_**5.47**
Ttc39c_**4.25**
Inpp1_**3.82**
Gtpbp2_**3.05**
Cnn3_**4.25**
Rab3ip_**3.15**
Rab21_**2.31**
Zc2hc1a_**2.52**
Armc8_**3.01**
Rbl1_**2.86**
Asah2_**2.89**
Kremen1_**2.35**
Pcsk7_**2.32**
Ace_**3.98**
Tmie_**4.33**
Crtam_**3.92**
Cmtr1_**2.4**
Gp6_**3.4**
Btla_**3.24**
Klrc1_**2.85**
Gm10298_**2.73**
Atp8b1_**2.23**
Ptafr_**3.47**
Tex15_**4.58**
Itpr1_**4.32**
Aim1_**2.98**
Socs2_**5.28**
Lilrb4_**2.52**
Cd86_**3.84**
Klf4_**4.43**
Prkx_**2.83**
Tagln_**2.34**
B3gnt5_**5.37**
Rgl1_**3.41**
Schip1_**3.99**
Spryd7_**2.46**
Ifrd1_**2.72**
Gm14057_**3.14**
Gm14253_**2.82**
Gm38228_**3.64**

Kdm6b_**4.14**
Slc11a2_**3.38**
Gp49a_**2.66**
Itpkb_**2.49**
Sorl1_**2.54**
Dirc2_**2.87**
Arf4_**2.48**
Fam49a_**2.32**
Rela_**2.15**
Ebi3_**2.51**
Arnt2_**3.53**
Abi3bp_**3.09**
H2-Ab1_**3.08**
Armcx6_**2.63**
H2-M3_**2.4**
Gm11613_**2.46**
Nppb_**2.61**
Ppm1l_**3.9**
Dbr1_**2.14**
Plekhn1_**2.67**
Ppp1r10_**2.09**
Plekhg1_**2.48**
Eng_**2.21**
Tlr9_**2.06**
Dync1i2_**2**
Mllt3_**2.91**
Hook2_**2.64**
Stau1_**2.03**
Stat3_**2.64**
Urgcp_**2.34**
Casz1_**2.8**
Acot9_**2.52**
Atad1_**2.48**
Ltv1_**2.2**
Pdgfc_**3.23**
Ctsh_**2.82**
Gphn_**2.39**
Tmem132a_**2.31**
Ehd4_**2.07**
Crem_**2.01**
Hivep2_**2.65**
Stx3_**3.12**
Stk40_**3.22**
Aff1_**2.46**
Fam46c_**4.24**
Rab12_**2.34**
Chd7_**2.88**
Btg1_**2.31**
Irf4_**2.23**
Gm15975_**2.33**
Ryr1_**2.65**
Cd38_**3.97**
Gm9791_**3.09**
Gstt1_**2.82**
Mgat1_**2.1**
F10_**2.38**
Slc4a11_**2.84**
Casp3_**3.25**
Rgs14_**2.28**
Nxf1_**2.45**
Cd300e_**2.34**
Gm19589_**2.9**
Csf3r_**2.62**
Pgap2_**2.1**
Ctgf_**2.05**
Slc25a12_**2.58**
Isoc1_**2.39**
Sh3bp4_**3.63**
Cask_**2.19**
Nck2_**2.31**
Batf_**3.31**
2610002M06Rik_**2.51**
Fbxo7_**2.26**
Rfc3_**2.66**
Zfp821_**2.22**
Fbxo4_**2.14**
Rbms1_**2.04**
Trip10_**2.23**
Hbegf_**2.02**
Greb1l_**2.67**
Cpeb4_**2.99**
Optn_**3.03**
Nr4a3_**3.99**
Trim25_**2.41**
Rhbdf2_**2.76**
Arl4a_**2.68**
Rabgef1_**2.55**
Ankrd33b_**2.69**
4930523C07Rik_**2.63**
Gm37570_**2.26**
Ddit3_**2.15**
Lgals9_**2.74**
Ildr1_**3.1**
Mvp_**2.05**
Tmem219_**2.08**
Gm13768_**4.54**
Phactr1_**4.38**
Rilpl1_**2.56**
Dmtn_**3.7**
Atp13a1_**2.17**
Arhgap28_**2.71**
Nlgn2_**2.28**
Lrp4_**2.29**
Fbrsl1_**2.24**
Myh10_**3.59**
Sppl2a_**2.48**
Cd180_**2.13**
Esr1_**2.69**
Dennd1a_**2.04**
Lgals8_**2.04**
Larp1b_**3.31**
Selt_**2.34**
Cmtm6_**2.47**
Capza2_**2.26**
Lmo2_**2.28**
Wars_**2.31**
Igf2bp2_**2.03**
Mgam_**2.18**
Rap1b_**2.03**
Gm14085_**4.88**

Tgfb1i1_**2.27**
Sass6_**2.01**
Adap2_**2.13**
Mecp2_**2.03**
Mir7026_**2.85**
Tmcc3os_**3.71**
Gm37261_**2.37**
Gm26606_**2.43**
Zcwpw2_**3.24**
Bcl2l15_**3.14**
Gm17046_**2.67**
Vegfc_**3.94**
Chmp4b_**2.7**
Fez2_**2.28**
2010109I03Rik_**2.68**
Gm8394_**2.04**
Slc1a2_**3.18**
Gm8818_**5.31**
Ifnb1_**10.54**
Ifna1_**8.48**
Ifna6_**8.13**
Gm29340_**2.92**
Ifna13_**5.89**
Isg15_**4.63**
Hspa1a_**3.38**
1700041G16Rik_**3.55**
Arhgef37_**4.51**
Fam3b_**7.11**
Rasl11b_**6.6**
Serping1_**5.51**
Hck_**3.23**
Tuba8_**5.55**
Ifna11_**7.97**
Tmprss2_**6.97**
Ifna16_**6.21**
Gm14010_**7.38**
Olfr433_**6.71**
Oas1b_**5.73**
Gm5511_**4.31**
Fpr1_**6.39**
Ncoa1_**2.47**
Sema7a_**2.54**
Ddr2_**2.06**
Cd200r2_**2.24**
Gm17111_**2.44**
Ptprd_**2.82**
Gm5398_**2.33**
Rtn2_**3.03**
5430405H02Rik_**3.12**
Gm16118_**3.19**
Idnk_**2.63**
Peg10_**3.04**
Dbnl_**2.44**
Polb_**2.26**
Gja6_**2.75**
Gm15223_**4.46**
RP24-374B14.4_**3.88**
Kcnd1_**4.3**
Ifna4_**9.73**
Ifna5_**8.59**
Tulp2_**4.39**
Fam71a_**4.56**
4930432E11Rik_**5.15**
Pnp2_**4.69**
Dhh_**4.12**
Plac8_**3.61**
Gm26603_**5.09**
Tarm1_**4.55**
Noxred1_**4.57**
0610043K17Rik_**5.87**
Ly6i_**5.09**
Trim69_**5.15**
Ifnab_**8.29**
Ifna15_**7.4**
Apobec4_**8.93**
Sectm1a_**7.64**
Gm15856_**6.18**
BE692007_**2.98**
Cpne9_**4.57**
Matn4_**5.23**
Axdnd1_**2.38**
Rbm11_**2.26**
Pgam2_**2.58**
Slain1_**2.88**
Gm26788_**3.88**
Gm13147_**2.43**
Tbx15_**2.16**
Il19_**4.04**
Sox3_**4.98**
1700026D08Rik_**2.54**
Plxna4os1_**2.33**
Gng11_**2.96**
Stoml1_**2.12**
Shox2_**2.88**
Muc1_**2.77**
RP23-173N16.8_**5.35**
Ephx3_**3.06**
Mrc2_**4.04**
Ifna2_**10.22**
Ifna9_**8.57**
Gm9694_**4.94**
1500012F01Rik_**3.33**
1700016G22Rik_**5.43**
Hspa1b_**3.74**
Gm18445_**3.91**
Lta_**6.14**
Vgf_**4.7**
Ccdc146_**6.23**
Serpinb2_**5.02**
Pla2g4e_**5.01**
Fap_**5.3**
Gm9574_**5.45**
Ifna14_**8.06**
Ifna12_**7.1**
Heatr9_**9.39**
Art3_**6.51**
RP23-23C4.6_**4.17**
H2-T10_**3.69**
Cyp26a1_**6.43**
Srms_**4.33**

Plscr2_**5.17**
Phlda1_**4**
Plekha6_**5.72**
Tbc1d13_**2.22**
H2-T24_**2.87**
Vwa3b_**3.4**
Gm16022_**4.94**
Gm15229_**3.91**
Ddc_**4.72**
Chrna5_**5.55**
Rsph4a_**2.92**
RP23-267O21.5_**3.92**
Ptk6_**3.8**
Aldh1b1_**3.24**
Trim17_**3.35**
Rec8_**3.41**
Nr1h5_**5.1**
Gm10134_**3.76**
Hhatl_**4.04**
Col24a1_**4.91**
Cyp3a13_**4.98**
Klri1_**3.32**
Ccdc162_**3.55**
Olfr518_**3.09**
Slc6a19os_**4.23**
Slc6a18_**4**
Ppp1r1b_**3.45**
Fitm1_**2.87**
Gm525_**3.36**
Lpcat2_**2.41**
9230104M06Rik_**2.89**
Slc5a5_**3.5**
Gm6548_**2.31**
Gm8810_**4.05**
Oas1e_**3.81**
Ifnz_**3.24**
Nlgn3_**3.52**
Gm17705_**2.86**
Pdgfrl_**3.46**
Islr2_**4.11**
Oas1d_**4.37**
Fam43a_**4.18**
Dyrk4_**4.99**
Col9a3_**4.9**
4930599N23Rik_**3.05**
Icam5_**3.94**
Ptges_**4.43**
A330074K22Rik_**2.47**
Gm15754_**5.65**
Pamr1_**5.68**
Gm8801_**4.99**
Maats1_**3.53**
Gm16028_**3.77**
Carlr_**3.3**
Rbpjl_**4.57**
Adra2b_**3.01**
Cdh22_**3.15**
Fam163a_**4.26**
4921523L03Rik_**3.73**
Insrr_**5.78**
Gm12979_**4.28**
Tmem184a_**4.9**
Gm37519_**3.49**
Gm15527_**3.62**
Cldn11_**2.35**
Adtrp_**3.94**
Scn10a_**3.8**
Robo3_**2.71**
Art2b_**2.86**
Ssc5d_**3.35**
Pacsin1_**4.71**
Reep2_**3.24**
Gm5692_**4.05**
Smtnl1_**3.78**
L3mbtl1_**3.63**
E330021D16Rik_**2.83**
Sema4f_**2.88**
Trim10_**4.18**
Ctrl_**4.34**
Scarf1_**2.6**
Gm11131_**3.64**
Ms4a6b_**3.4**
St8sia1_**3.42**
Hap1_**3.93**
Rnf34_**2.95**
Gm17435_**3.03**
Gm20394_**3.31**
Fbxo39_**4.26**
Nrxn2_**5.55**
Gpr55_**3.94**
Gm38050_**3.68**
Gcg_**5.06**
Usp17ld_**4.01**
RP23-253G12.8_**3.33**
Adcy4_**3.7**
Gm11292_**2.96**
Faah_**3.55**
Ifna7_**3.99**
Gm10287_**3.3**
Dennd6b_**3.89**
Rp31-ps19_**3.69**
Rasgef1c_**4.16**
Wdr86_**4.35**
4930444G20Rik_**3.1**
Gm10344_**3.08**
1600029O15Rik_**3.98**
Gm6537_**3.41**
Gm12631_**2.43**
Gpr87_**2.72**
Dnaaf3_**2.86**
Olfr432_**4.66**
Lag3_**5.84**
Gm13535_**4.53**
Obscn_**4.1**
Igf2_**2.93**
Ly6a_**2.69**
Slc44a3_**3.52**
Gna14_**2.42**
Tcap_**3.58**
Psmb10_**3.04**

Psmb9_**2.79**
Cst7_**2.83**
Sema5b_**3.19**
Rasd1_**3.06**
Ccdc64b_**4.05**
A930011G23Rik_**3.2**
Inca1_**2.35**
Tcaf2_**2.79**
Ltbp1_**4.22**
Acvr1c_**4.48**
Tespa1_**3.9**
Pcdh10_**2.66**
Antxr1_**3.44**
Tnni3_**3.36**
Gm5581_**3.13**
Gm26592_**4.24**
RP24-404P10.2_**2.9**
Tet1_**3.69**
Gm13284_**4.12**
Gm10555_**3.13**
Slc27a5_**3.3**
Gm16133_**3.22**
Col4a2_**2.36**
Olfr431-ps1_**2.98**
Gm24671_**2.94**
Snai1_**3.39**
Grm1_**3.05**
Slc8a2_**2.84**
Ptgdr2_**2.38**
Gm17034_**3.25**
Serpinf2_**2.27**
Gm7582_**3.29**
Nhlh1_**4.46**
Rnu5g_**3.01**
Gm13288_**3.46**
Gm22710_**3.03**
Gm26917_**2.65**
B930036N10Rik_**2.58**
RP23-23C4.5_**4.28**
9330175E14Rik_**3.28**
H2-T22_**2.46**
Clec1b_**2.9**
Fam83a_**2.9**
Gm19684_**3.16**
Tex14_**2.76**
Vnn3_**2.73**
Cox18_**2.08**
Ccdc154_**5.83**
Rasgrf1_**5.93**
RP24-547J21.4_**5.08**
Gm15478_**3.5**
Tnfrsf14_**3.16**
Lox_**2.67**
Gm37387_**3.72**
Gm4832_**2.29**
Car4_**4.18**
Angptl1_**2.84**
Gm19412_**4.32**
Tmem151b_**4.13**
Oas1f_**3.34**
Gm37563_**3.47**
Jsrp1_**2.42**
Rsrp1_**2.15**
Gm884_**2.91**
Asgr1_**2.95**
Dazl_**2.57**
Gast_**2.82**
Ebf4_**2.85**
Cbx4_**2.05**
Clcn1_**2.13**
Rnase10_**3.91**
Rmrp_**2.56**
Gm7599_**3.1**
Ccno_**2.8**
Popdc2_**3.38**
BC051226_**2.04**
Rpph1_**2.21**
Ltb_**2.16**
RP23-422D12.3_**3.85**
RP24-547J21.3_**2.78**
I830077J02Rik_**2.63**
Armc3_**2.79**
Ampd1_**2.81**
Cdh5_**2.34**
Gm26902_**2.4**
9130230L23Rik_**2.65**
Gm1110_**3.24**
Gm16685_**4.81**
Dnah10_**4.53**
Gm37498_**2.86**
Gm3912_**3.68**
Pip5kl1_**2.18**
Gbp2b_**5.49**
Sidt1_**2.74**
Prph_**2.16**
Tcfl5_**3.77**
Homer2_**2.73**
Enpp2_**4.34**
4930535L15Rik_**3.7**
RP24-333H9.2_**3.7**
Fcrl5_**4.46**
Col3a1_**2.63**
Ttc9b_**2.99**
Cend1_**2.89**
4930488B22Rik_**2.92**
Gm17396_**3.04**
Olfr549_**2.94**
Chdh_**2.82**
Gm26707_**3.41**
Lama5_**2.04**
Gm28177_**3.37**
Olfml2a_**2.35**
Etv2_**3.65**
Egr1_**3.52**
Gm28707_**2.21**
Gm15488_**2.84**
Gm26656_**2.18**
RP23-1A12.2_**4.66**
Clec12b_**3.33**
Oas1h_**3.28**

Gm6034_**2.79**
Tldc2_**2.73**
Prrx1_**2.54**
Espn_**2.59**
Serpinh1_**2.5**
Hist4h4_**3.58**
Bbc3_**3.09**
Gm26847_**2.37**
Hist1h4j_**2.5**
Gm4952_**2.47**
Bcat1_**2.85**
Chst2_**3.59**
Jph2_**2.75**
Cdh24_**3.29**
Vil1_**2.45**
Ccbe1_**3.09**
Dst_**3.13**
Cdh11_**2.36**
Foxl2_**4.02**
Gm23247_**2.75**
Gm5532_**2.31**
Gm13450_**3.47**
Gm15701_**2.52**
Gm26582_**3.25**
Slco2a1_**2.1**
Hist1h4d_**2.73**
Gm10800_**2.86**
Gm38162_**2.04**
Bmp8b_**3.21**
Nat14_**2.78**
Gm29083_**4.15**
4933416M07Rik_**3.21**
Gpr171_**4**
Pax5_**4.39**
Lmo7_**3.05**
Ly6c2_**3.92**
Gm2619_**3**
Gm11212_**3.42**
8030442B05Rik_**2.83**
Gpr31b_**5.2**

Ppm1e_**2.04**
Dpysl3_**2.74**
Dnm3_**3.16**
Gm21738_**2.4**
Atp1b2_**2.16**
Timd4_**4.32**
Gm37084_**3**
Gm38227_**2.17**
Myo15b_**2.84**
Rprml_**4.22**
Ttc16_**2.91**
Stk39_**3.41**
RP24-317M4.2_**2.49**
RP23-114P22.5_**2.79**
Igfbp7_**2.33**
Mcmdc2_**2.81**
Dock8_**2.13**
Gm9959_**2.45**
Neurod4_**3.07**
Fcrlb_**4.15**
Aanat_**4.05**
Rapgef4_**3.17**
Gm37419_**2.98**
Gm1070_**2.47**
RP23-182M12.4_**2.99**
RP23-182M12.3_**2.26**
Gm10801_**2.23**
B4galt2_**3.48**
1700001P01Rik_**3.01**
Gm38275_**2.41**
Olfr760-ps1_**4.33**
Gm28169_**3.27**
Gm28321_**6.02**
Ptchd2_**3.4**
RP24-377E5.1_**4.27**
Gabra4_**5.26**
Tm4sf20_**3.21**
Gm2238_**4.99**
Ccl17_**4.84**
Klra17_**5.05**

Adgrg7_**2.05**
Gm16675_**2.55**
Sh2d5_**2.33**
Srpx2_**2.27**
Col6a3_**2.07**
Apon_**2.44**
A130071D04Rik_**3**
Hist2h4_**2.04**
Espnl_**2.49**
Slit2_**3.3**
Cfap54_**4.09**
Bmpr1b_**2.85**
Dlgap1_**2.34**
Gm12735_**2.43**
Masp1_**3.01**
Gm4761_**4.2**
Ms4a14_**2.75**
Pxdn_**2.16**
A430078I02Rik_**3.01**
RP24-142B15.6_**2.68**
Gm8909_**3**
BX510318.1_**2.43**
Gm10053_**2.77**
RP23-199B2.8_**2.41**
Spint2_**2.95**
Ccdc50-ps_**2.1**
Ccr9_**2.65**
1700123I01Rik_**3.13**
Xirp1_**2.68**
Nrg1_**4.34**
Gm28563_**3.03**
Gm29284_**3.84**
Gm29461_**4.76**
Gm10125_**3.89**
Tmprss4_**5.34**
Ano4_**4.72**
Rhbg_**3.34**
Sox5os3_**2.92**
Fbn2_**2.84**
Setbp1_**4.06**

Serpina3e-ps_**4.66**
Gm16213_**2.83**
Crb2_**3.64**
Ly6c1_**3.09**
Gm5468_**3.38**
RP24-418J2.4_**4.2**
Emx2_**3.6**
Scn2a1_**5.86**
Pramef6_**2.97**
Hc_**3.45**
Gm5152_**5.14**
Nt5c1a_**3.09**
Egr4_**2.87**
Ptchd3_**2.7**
Hist1h2ab_**2.72**
Ebf1_**3.07**
Nmnat2_**2.81**
Clec2e_**4.6**
Cidec_**3.12**
Gm10030_**3.48**
Gm11425_**2.17**
Gm11857_**2.1**
Ccl11_**3.56**
Gm37820_**3.75**
Gm24265_**3.03**
RP23-338P12.2_**3.36**
Cycs_**3.09**
Nfkbil1_**2.24**
RP23-50I16.2_**2.58**
Ggct_**2.15**
H2-T23_**2.33**
Psmb8_**2.26**
Slpi_**2.14**
Gm17673_**3**
Gm16156_**2.28**
6820402A03Rik_**2.91**
Fth-ps2_**2.67**
Serpinb1b_**2.62**
Susd2_**2.62**
2410006H16Rik_**2.03**

Hamp_**2.83**
Kncn_**2.77**
Smoc2_**3.97**
4922502D21Rik_**3.03**
Sall1_**5.51**
Gm12752_**3.87**
Gm11784_**3.59**
Gm27008_**2.92**
Hist1h2bl_**3.31**
Igfbp3_**3.34**
Sfrp1_**3.99**
Myt1l_**2.95**
1700019E08Rik_**2.84**
Mir7213_**2.99**
Gm15425_**2.64**
Gm13500_**3.95**
RP24-421E18.7_**3.02**
Gm9830_**2.74**
Akr1c14_**3.09**
Gm13400_**2.94**
Wdr20rt_**2.23**
Gm12984_**4.86**
Fkbp10_**3.17**
Nts_**3.08**
Rasl11a_**2.75**
Cdc42ep2_**3.07**
Snx20_**2.38**
A4galt_**2.99**
Pnp_**2.86**
Ctsc_**2.18**
Gadd45g_**2.31**
Ccdc23_**2.24**
Gm20627_**2.07**
Gm6225_**2.49**
Arhgap8_**4.38**
Adam32_**2.47**
Platr17_**2.89**
Gm14537_**2.46**
Plekhg4_**2.28**
Fam229a_**3.54**

Cfap58_**3.28**
Gm17244_**4.47**
Ttll9_**3.06**
Cachd1_**2.85**
H2-M6-ps_**3.4**
Oxct2a_**4.01**
Foxa1_**3.29**
Pdzph1_**3.44**
Gm11722_**3.36**
Klhl29_**4.39**
Olig3_**3.11**
Gm4954_**2.95**
Mep1a_**2.78**
Gm17207_**2.78**
Nphs2_**2.56**
Pldi_**3.26**
H2-T3_**3.47**
Gm12858_**3.3**
Mospd4_**3.04**
RP24-224N3.9_**2.21**
Fbxl22_**2.13**
Mpo_**4.91**
Baiap3_**3.34**
Gm37115_**2.91**
Hist1h4c_**2.33**
Gm7281_**2.82**
Gm12989_**2.41**
RP24-224N3.8_**3.14**
Chst7_**2.61**
Psma5_**2.32**
Pttg1_**2.35**
Sertad3_**2.51**
Gm37045_**2.39**
Platr6_**2.71**
Gabbr1_**3.13**
Plekhh1_**3.29**
Siglece_**2.66**
Bmp1_**2.94**
Gm14140_**2.23**
Syt7_**2.81**

Dnaic2_**2.44**
Pcdh19_**2.37**
Vgll3_**2.51**
Abcc5_**2.01**
Trp53cor1_**2.88**
Mmp13_**2.03**
Gm13283_**3.16**
Mill2_**2.34**
Ms4a6d_**2.01**
Sparc_**2.67**
Col5a1_**2.52**
Pecam1_**2**
Npr1_**2.23**
Hes1_**2.23**
Ttc21a_**2.28**
BC049352_**2.07**
Rgs20_**3.07**
Pdgfra_**2.28**
n-R5s29_**2.85**
Gm26910_**2.5**
Fos_**3.31**
Gm26522_**2.76**
Gm7115_**2.9**
Mitf_**2.22**
Gm15366_**2.42**
Gm20612_**2.55**
Orai2_**2.3**
Tal2_**3.4**
Kcnj2_**2.88**
Tgif2_**2.78**
Gm38002_**2.44**
E430024P14Rik_**3.31**
Wnt5a_**2.5**
Ccdc116_**2.89**
Btnl7-ps_**3.4**
Gm43160_**2.43**
Met_**2.13**
Il1bos_**4.53**
Gm14269_**3.4**
Sdc4_**2.98**

4933433G15Rik_**3.59**
Gm6335_**2.98**
Gpc4_**2.65**
2900089D17Rik_**2.37**
Cxcl12_**2.47**
RP24-326F21.2_**3.94**
0610039K10Rik_**2.68**
Ms4a4a_**2.46**
A730011C13Rik_**2.18**
Col1a1_**2.26**
Bgn_**2.01**
Fstl1_**2.26**
Zc3h6_**2.1**
Acyp2_**2.04**
Pygm_**2.43**
Col8a1_**2.37**
Gm18953_**2.26**
Scube3_**2.78**
Ifi202b_**3.05**
Btg2_**5.86**
Gykl1_**3.65**
Cacng8_**3.3**
Rnd1_**2.77**
Gm14636_**3.11**
Mir221_**2.81**
2310043L19Rik_**2.89**
Treml4_**2.14**
Id3_**3.9**
Mettl21b_**2.49**
Gm37472_**2.55**
Gm37296_**4.61**
Cmya5_**3.02**
Gm5106_**2.22**
Ptprk_**2.87**
Cyp1b1_**2.9**
Gm8856_**2.7**
Gm11025_**4.75**
Mir3074-1_**2.85**
Bcam_**3.02**
Prr7_**2.89**

Elovl4_**3.43**
Col6a2_**2.85**
Mybpc3_**2.46**
Riiad1_**2.07**
Has1_**2.39**
Gm25594_**4.02**
Skor1_**3.06**
Gm15133_**2.24**
Grem1_**3.09**
Col1a2_**2.22**
Plcd4_**2.35**
Perm1_**2.08**
Mmp9_**2.13**
F8_**2.05**
Tead1_**3.01**
Icam4_**2.29**
Gm22079_**2.64**
Glcci1_**3.04**
8430408G22Rik_**2.1**
Gm17334_**5.37**
Pcdh18_**3.73**
Npnt_**3.16**
Gm18301_**3.24**
Capns2_**2.38**
Hist1h2be_**2.59**
Cd70_**2.86**
Gm20655_**2.67**
Gm27017_**2.86**
Zfp119b_**2.03**
RP23-376H8.2_**2.7**
Gm8989_**3.66**
RP23-465M13.2_**3.06**
Tmem47_**3.11**
4930469K13Rik_**2.19**
Lct_**2.28**
Gm12345_**2.49**
RP24-314I8.3_**3.96**
Gm6736_**3.15**
Gm11865_**2.05**
Cacnb3_**3.95**

Rffl_**3.14**
Fam133b_**2.46**
Tnip1_**2**
Gm15601_**3.41**
Klhl25_**2.39**
Tsc22d1_**2.55**
Acvr2a_**2.51**
Stard7_**2.83**
Zfp619_**2.33**
RP23-434H17.3_**2.41**
Gm12598_**2.75**
Cdkn2b_**2.37**
Acot10_**3.41**
Gm12511_**3.62**
Gm16301_**2.82**
Gm12905_**3.91**
Chac2_**2.54**
Tenm4_**5.01**
Myo16_**3.77**
Numb_**2.62**
Atm_**2.84**
Cntrl_**2.8**
Plcb3_**2.12**
Hmbox1_**2.52**
Rnf214_**2.58**
Pla2g4a_**2.51**
Abca13_**2.18**
Ap3m2_**2.09**
Cpm_**3.77**
Gm6226_**3.92**
Atf4_**2.85**
Gmeb2_**4.38**
Tbk1_**3.38**
Tmem2_**3.6**
Stxbp3-ps_**3.82**
Nr3c1_**3.23**
Rnf24_**3.57**
Cul1_**3.03**
Cnksr3_**3.4**
Rnf145_**2.48**
Sgms1_**2.75**
Gadd45a_**3.3**
RP23-395B13.2_**3.2**
Herpud1_**4.21**
Ifngr1_**2.37**
Snx18_**2.51**
Dusp4_**2.46**
Siah1b_**2.16**
Mir27b_**2.08**
Olr1_**2.02**
Bcar1_**2.7**
Tra2b_**2.08**
Gm26652_**4.1**
4930551O13Rik_**3.06**
Gm38327_**2.79**
Neurl3_**2.27**
Bmp8a_**2.44**
Prdm9_**3.86**
Fhod3_**4.26**
Ccr5_**2.61**
Fryl_**3**
Camsap1_**3.74**
Marf1_**3.1**
Gm15800_**3.27**
Klhl18_**2.26**
Plag1_**2.54**
Col20a1_**2.21**
Cox20_**3.35**
Chac1_**3.7**
Fnip1_**3.27**
Lemd3_**4.22**
Fbxw11_**3.98**
Rnf14_**3.04**
Rnf115_**3.18**
Fbxw7_**2.81**
Scyl2_**2.96**
Ppfibp2_**4.45**
Nab1_**2.8**
Mdfic_**2.87**
Tmod3_**2.84**
Vps37c_**2.58**
Ehd1_**2.19**
Gm37674_**3.93**
Gimap6_**3.13**
Rnf19a_**2.99**
Gm37783_**2.48**
Plxna2_**2.02**
Mdm4_**2.64**
Gm17024_**2.52**
Gm8850_**2.5**
RP23-326O2.2_**2.57**
Gm28050_**3.75**
Gm15785_**3.78**
Hmcn1_**3.5**
Dpf3_**2.93**
Irf8_**3.26**
Prkcq_**2.26**
Akt3_**3.79**
Intu_**4.08**
Atg16l1_**2.55**
Birc6_**2.81**
Snw1_**2.33**
Brwd3_**2.86**
Ttc9c_**2.36**
Sema3c_**3.41**
Mertk_**2.46**
Zfp324_**2.12**
Nrip3_**3.92**
Klf3_**3.63**
Fbxo30_**2.97**
Rbpms_**3.35**
Ppp1r15b_**3.23**
Rbbp8_**3.47**
Zcchc6_**3.23**
Mtm1_**2.68**
A230046K03Rik_**2.89**
Wdfy1_**3.03**
Pfkfb3_**4.2**
Fmr1_**2.82**
Cldnd1_**2.73**

Basp1_**3.18**
Dr1_**2.58**
Fndc9_**4.14**
Cdk12_**3.11**
Uvrag_**2.59**
Smcr8_**2.6**
Rictor_**2.38**
Slfn10-ps_**2.5**
Zfp719_**3.29**
Spty2d1_**3.33**
Erbb2ip_**2.82**
Fem1c_**3.02**
Tbc1d1_**2.87**
Msantd2_**3.09**
Acer3_**2.22**
Tma16_**3.35**
Prkaa2_**4**
Atxn7_**3.43**
Adnp2_**3.22**
Ubap1_**3.01**
Tmem110_**3.86**
Itpkc_**3.26**
Mlxip_**3.01**
Kit_**3.64**
Dcp1a_**2.95**
Inppl1_**2.78**
Cyld_**2.48**
Dio2_**3.06**
Seh1l_**3.3**
Avl9_**2.98**
Ino80_**2.68**
Casp2_**2.94**
Neu3_**2.32**
4932438A13Rik_**2.35**
Arntl_**2.77**
Dcun1d3_**3.03**
Mtdh_**2.51**
Slc44a1_**2.2**
Spata5_**2.68**
Ccdc71l_**2.11**

Stim2_**2.5**
Ppp2r2a_**2.44**
Slc7a11_**4.17**
Neto2_**2.93**
Kansl1l_**2.78**
Nktr_**2.62**
Ptprj_**2.76**
Ccdc63_**4.57**
Aebp2_**3.48**
Sestd1_**2.81**
Cdk6_**2.55**
Ugcg_**3.33**
Pik3r5_**2.59**
Ddx24_**2.51**
Zfp455_**2.21**
Card6_**2.91**
Fbrs_**3.31**
Cnot4_**3.38**
Kpna4_**3.33**
Mob1b_**3.2**
Lsm14a_**2.54**
Zfp868_**2.95**
Taf4b_**3.43**
Btaf1_**3.06**
Pias1_**3.05**
Mapkbp1_**2.88**
Zfyve26_**2.48**
Atp11b_**2.87**
Cggbp1_**2.51**
Rsbn1l_**2.85**
Dmtf1_**2.6**
Zfp213_**2.4**
Herc1_**3.1**
Bbx_**2.47**
Kbtbd2_**2.67**
Ddhd1_**3.33**
Nup54_**2.66**
Traf6_**2.78**
Tmem39a_**2.68**
Grap_**2.52**

Rpe_**2.58**
Irf5_**2.94**
Slc23a2_**3.09**
Arl5b_**3.37**
Zbtb21_**2.68**
Lpin2_**2.48**
Brd2_**2.54**
Osm_**3.83**
Ncoa5_**3.09**
Sertad2_**3.13**
Osgin2_**3.6**
Ccdc50_**2.64**
Fam129a_**2.36**
Elmod2_**2.29**
Myo10_**3.67**
Gripap1_**2.33**
Zfp952_**3.88**
Gpbp1_**3.14**
Sh3bp2_**3.3**
Tab2_**3.13**
Tmem68_**2.43**
Zfp160_**2.47**
Dnajc1_**3.09**
Frs2_**2.84**
Clk1_**2.82**
Dnm1l_**2.92**
Akap13_**3.31**
Ttc39b_**2.67**
Ankfy1_**2.45**
Phf20l1_**2.76**
Pde7a_**2.68**
A430106G13Rik_**2.62**
Lnpep_**2.62**
Gm13719_**3.74**
Ikzf5_**2.52**
Gramd3_**3.76**
Cx3cl1_**3.04**
Zfp628_**2.43**
Trit1_**2.18**
WI1-1010L24.1_**3.44**

1700109H08Rik_**3.35**
Gm15717_**2.74**
RP23-293K21.1_**2.31**
Tcea1-ps1_**2.08**
Ulbp1_**3.57**
Gm6483_**2.25**
Ppp1r12a_**2.63**
Crkl_**2.01**
RP23-425I8.2_**3.28**
Pdp1_**3.11**
Ccne1_**3.43**
Mylip_**3.08**
Notch1_**3.44**
Fbxo42_**2.61**
Gm13391_**2.8**
Slc9a1_**2.23**
Inpp5b_**2.59**
Dock11_**2.35**
Efcab6_**3.49**
Kmt2c_**2.65**
Usp47_**2.84**
Galnt7_**2.14**
Itpripl2_**2.4**
Dnajc13_**2.59**
Hipk2_**2.41**
Parp4_**2.24**
Mtmr11_**2.29**
BC030336_**2.02**
Tlr4_**2.04**
Ctnnal1_**2.54**
Stag2_**2.05**
Htr2a_**2.69**
Mcur1_**2.04**
Raf1_**2.06**
Ptpn23_**2.4**
RP23-164N7.3_**2.19**
Ino80d_**2.37**
Sema4b_**2.68**
Stam2_**2.09**
Rragc_**2.52**
Plekhm3_**2.5**
Tmed8_**2.16**
Slc8a1_**2.26**
Rfx5_**2.31**
Zfp407_**2.29**
Atad2b_**2.33**
Tnks_**2.47**
Gm37893_**2.44**
Gm336_**2.85**
Rusc2_**2.85**
Fut8_**2.64**
Ktn1_**3.4**
Rnf4_**2.59**
Notch2_**2.55**
Dcaf6_**2.11**
Net1_**2.87**
Scfd1_**2.81**
Hps3_**2.09**
Kdm4a_**2.61**
Usp31_**2.96**
Stag1_**2.8**
Gcc1_**2.15**
R3hcc1l_**2.25**
Ap3b1_**2.38**
Npepps_**2.25**
Sipa1l1_**2.22**
Wrn_**2.23**
Pphln1_**2.11**
Trnt1_**2.15**
Arap2_**2.96**
Adgrg6_**2.79**
Kctd10_**2.19**
Pfkp_**2.22**
Cblb_**2.86**
AW549877_**2.38**
Ric1_**2.17**
Kmt2a_**2.37**
Gab2_**2.43**
Arl4c_**2.19**
Elk4_**2.43**
Mllt6_**2.78**
Alpk1_**2.01**
Dclre1c_**2.09**
Dlc1_**3.82**
Prdm2_**2.57**
Gm19026_**3.16**
Nrp2_**2.04**
Gm20689_**2.07**
Fam167a_**3.93**
Cyp4f18_**3.11**
Kitl_**2.21**
Pkn2_**2.77**
Phlpp2_**2.69**
Atp8a1_**2.68**
Sik3_**2.56**
St3gal5_**2.53**
Utrn_**3.17**
Ankib1_**2.36**
Mark2_**2.33**
Ambra1_**2.33**
Krit1_**2.37**
AI314180_**2.2**
Cpsf2_**2.04**
Psme4_**2.35**
Msi2_**2.32**
Arfgef1_**2.12**
Dgkh_**2.39**
Trip12_**2.02**
Acvr1_**2.14**
Pi4k2b_**2.39**
Pacs2_**2.48**
Eif4e3_**2.09**
Abhd16a_**2.19**
Mtmr12_**2.81**
Lyst_**2.3**
Hectd2_**2.21**
Med1_**2.1**
Atp2b1_**2.5**
Rab8b_**2.39**
Tmem168_**2.17**

Map4k3_**2.53**
Kctd3_**2.13**
Pkp4_**2.44**
Foxp1_**2.26**
Cdyl_**2.2**
Golph3_**2.17**
Reps1_**2.14**
Gucd1_**2.33**
Eif5_**2.11**
Ints8_**2.55**
Prmt10_**2.23**
Osbpl3_**2.36**
Ing3_**2.08**
Pwwp2a_**2.29**
Slc38a2_**2.53**
U2surp_**2.08**
Epc2_**2.32**
Pum2_**2.06**
Btbd7_**2.07**
Setd2_**2.09**
Ncoa3_**2.1**
Gm21092_**2.07**
Rab28_**2.02**
Cep192_**2.15**
Irs2_**2.22**
Kansl3_**2.03**
Gm11739_**2.12**
Gm15512_**2.1**
Lzts2_**2.28**
Zfp827_**2.42**
Bcor_**2.02**
Gdf15_**3.15**
Fdxacb1_**2**
Sik1_**2.44**
Traf3_**2.19**
Zfp655_**2.25**
Gm12263_**2.09**
Zbtb8a_**2.32**
Epha4_**2.42**
Adap1_**2.33**

Ahr_**2.67**
Twsg1_**2.41**
Fbxo11_**2.58**
Gfpt1_**2.04**
Rnpc3_**2.18**
Ppp2r3a_**2.37**
Akna_**2.06**
Bsdc1_**2.03**
Grhl1_**2.37**
4930402H24Rik_**2.25**
2810403A07Rik_**2.07**
Arhgap26_**2.51**
Micu3_**2.25**
Pan3_**2.15**
Rbm39_**2.2**
Wac_**2.39**
Crybg3_**2.61**
Zkscan6_**2.22**
Ccdc186_**2.01**
Kdm3a_**2.5**
Lrig2_**2.07**
Bmp2k_**2.6**
Ythdc1_**2.05**
Arhgap10_**2.07**
Wee1_**2.14**
Unkl_**2.02**
Zbtb46_**2.45**
Mreg_**3.09**
Pbx4_**2.1**
Sde2_**2.1**
Plau_**2.72**
Siah1a_**2.39**
Slc25a33_**2.26**
Sema6d_**2.38**
Prkab2_**2.04**
Tanc1_**2.03**
Gm6776_**2.21**
Zfpm2_**2.98**
Gm527_**2.28**
Slc35f5_**2.23**

Tsc22d2_**2.49**
Iqgap1_**2.29**
Riok3_**2.19**
Rcbtb1_**2.35**
Ptbp2_**2.31**
Slc30a4_**2.16**
Zbtb18_**2.11**
Gm43166_**2.14**
Ndst3_**2.64**
Arid2_**2.13**
Vash1_**2.91**
Crtc2_**2.43**
Dip2c_**2.27**
Zfp39_**2.25**
Plcxd2_**2.31**
Suco_**2.35**
Fbxo38_**2.08**
Ubr5_**2.26**
Ttc17_**2.37**
Rc3h1_**2.16**
Arhgap22_**2.19**
E2f5_**2.38**
Iba57_**2.01**
Mcts2_**2.61**
Xpo6_**2.04**
Pbx1_**2**
Gm37874_**2.76**
Kctd6_**2.46**
St3gal3_**2.21**
Gm16907_**2.01**
Slc25a19_**2.22**
Rap2b_**2**
Gm7224_**2.08**
Zbtb17_**2.21**
Pik3c2a_**2.14**
Dmxl1_**2.03**
RP23-356K2.5_**3.32**
Spata21_**2.67**
RP23-171F16.5_**3.35**
Ccdc94_**2**

Psip1_**2.16**
Aig1_**2.26**
Gpatch3_**2.11**
Gm9396_**2.58**
Ankrd24_**2.06**
Egfr_**2.49**
Klf11_**3.29**
Bahcc1_**2.1**
Gm10254_**2.4**
Efr3b_**2.2**
Col15a1_**2.92**
Tm4sf5_**2.44**
Rcor2_**2.17**
Tnfrsf11b_**2.68**
Stap2_**2.01**
Gm21859_**2.64**
Slc12a5_**2.39**
Gm4997_**2.45**
Gm15236_**2.44**
1810011O10Rik_**2.83**
Dnajb3_**3.08**
Gm8000_**3.61**
Rps4l-ps_**3.39**
Dnmt3a-ps1_**3.69**
Ablim2_**2.18**
Gm17087_**4.07**
Gm15238_**2.78**
Gm38329_**2.33**
Gm8185_**2.27**
Gm38091_**2.13**
Gm7104_**2.62**
Msantd1_**2.39**
Dnah3_**2.53**
Grem2_**2.44**
Pex13-ps_**2.89**
Gm14292_**2.05**
Gm3052_**2.23**
Gm12057_**2.49**
Leng1_**2.06**
Gm6872_**2.15**

Mbip_**2.01**
Prpsap1_**2.36**
Siah2_**2.31**
Med28_**2.25**
Lrrd1_**2.2**
Klk1b11_**2.03**
RP23-357D17.4_**2.76**
Olfr111_**2.32**
Akap6_**3.22**
Pilrb2_**2.07**
Cdc14a_**2.04**
Spin3-ps_**2.06**
Paqr3_**2.1**
1110035H17Rik_**2.36**
Gm23468_**2.92**
Gm2539_**3.04**
9130230N09Rik_**3.09**
Nudt9_**2.16**
Mfsd6l_**2.01**
Gm11455_**2.73**
Ccl20_**4.68**
Trpc4_**3.35**
A930019D19Rik_**2.64**
Gm20531_**2.32**
Gm6695_**2.13**
Gm12115_**2.75**
Gm11945_**2.32**
Gm4799_**2.01**
Gpr182_**2.58**
Gm5946_**2.03**
Kcna7_**2.6**
Gm25026_**3.1**
Gabbr2_**2.46**
Dnaja1-ps_**3.88**
Gm12791_**2.41**
Gm29488_**2.71**
Gm8141_**2.29**
Arntl2_**2.42**
Tmem170_**2.06**
Ovol1_**2.13**

Dnajc21_**2.06**
Tiprl_**2.03**
Sycp2_**2.68**
Ece2_**2.04**
Gm37621_**2.04**
1700058P15Rik_**2.59**
Mab21l3_**3.09**
Gm6162_**2.18**
AU020206_**2.2**
Msl2_**2.57**
Zfp438_**2.08**
Gm5920_**2.06**
Gm8261_**2.05**
Nyap2_**2.07**
Tmem200a_**2.94**
Foxc1_**2.61**
Sertad1_**2.59**
Gm15793_**2.07**
D330050G23Rik_**2.23**
Gm15773_**2.57**
Shbg_**3.93**
Naip3_**2.31**
Lgr6_**2.34**
Mir23b_**2.4**
Rbm6-ps2_**4**
Gm12221_**2.66**
Gm4149_**2.08**
Gm11620_**3.23**
Gm6119_**3.49**
Gm2756_**2.59**
Gm13359_**2.56**
Gm23205_**2.31**
Gm37689_**2.25**
RP23-358O22.1_**3.03**
Gm22516_**2.33**
Gm17160_**2.99**
Yes1_**3.21**
Hk2_**2.15**
Orc1_**2.06**
Fbxl15_**2.11**

| | | |
|---|---|---|
| 2010300C02Rik_**2.09** | Gm13361_**2.34** | Gm36638_**2.25** |
| Igf2bp1_**2.28** | Gm10499_**2.9** | H2-Bl_**2.44** |
| Tuba3b_**2.99** | Cdo1_**2.04** | Gm6305_**2.28** |
| 4930518I15Rik_**2.19** | Gm37760_**2.12** | Npff_**2.16** |
| 5830444B04Rik_**2.1** | RP23-370G17.4_**2.75** | Gm16731_**2.38** |
| Mcc_**2.3** | Apom_**2.03** | RP23-409I5.2_**2.03** |
| Cebpd_**2.39** | Tnip3_**2.18** | |

**Table S2. List of 30 Unique Genes in Statistically Significant Functional Clusters within Group 1.** See Table S1 for table legend.

Gene Name_**$\mathbf{Log_2}$ Fold-change**

| | | |
|---|---|---|
| Ifna2_**10.22** | Ifnb1_**10.54** | Ifna4_**9.73** |
| Ifna5_**8.59** | Ifna1_**8.48** | Ifna9_**8.57** |
| Ifnab_**8.29** | Ifna6_**8.13** | Ifna14_**8.06** |
| Ifna11_**7.97** | Ifna15_**7.4** | Ifna12_**7.1** |
| Ifna16_**6.21** | Lta_**6.14** | Oas1b_**5.73** |
| Ifna13_**5.89** | Serping1_**5.51** | Srms_**4.33** |
| Oas1d_**4.37** | Isg15_**4.63** | Ptk6_**3.8** |
| Trim10_**4.18** | Oas1h_**3.28** | Ssc5d_**3.35** |
| Ifna7_**3.99** | Hck_**3.23** | Ifnz_**3.24** |
| Oas1e_**3.81** | Oas1f_**3.34** | Gm13288_**3.46** |

**Table S3. List of 151 Unique Genes in Statistically Significant Functional Clusters within Group 2.** See Table S1 for table legend.

Gene Name_**$\mathbf{Log_2}$ Fold-change**

| | | |
|---|---|---|
| Gmeb2_**4.38** | Prkaa2_**4** | Fbxw11_**3.98** |
| Zfp952_**3.88** | Prdm9_**3.86** | Kit_**3.64** |
| Akt3_**3.79** | Efcab6_**3.49** | Klf3_**3.63** |
| Rnf24_**3.57** | Aebp2_**3.48** | Dpf3_**2.93** |
| Taf4b_**3.43** | Notch1_**3.44** | Atxn7_**3.43** |
| Tbk1_**3.38** | Cnot4_**3.38** | Zfpm2_**2.98** |
| Rbpms_**3.35** | Spty2d1_**3.33** | Klf11_**3.29** |
| Zfp719_**3.29** | Gm15800_**3.27** | Itpkc_**3.26** |
| Irf8_**3.26** | Nr3c1_**3.23** | Adnp2_**3.22** |
| Rnf115_**3.18** | Gpbp1_**3.14** | Sertad2_**3.13** |
| Cdk12_**3.11** | Ncoa5_**3.09** | Mylip_**3.08** |
| Pias1_**3.05** | Rnf14_**3.04** | Cul1_**3.03** |
| Fem1c_**3.02** | Mlxip_**3.01** | Rnf19a_**2.99** |
| Fbxo30_**2.97** | Zfp868_**2.95** | Irf5_**2.94** |

Mdfic_**2.87**
Cblb_**2.86**
Atm_**2.84**
Epha4_**2.42**
Atf4_**2.85**
Clk1_**2.82**
Birc6_**2.81**
Fbxw7_**2.81**
Nab1_**2.8**
Traf6_**2.78**
Arntl_**2.77**
Pkn2_**2.77**
Phf20l1_**2.76**
Sgms1_**2.75**
Mcts2_**2.61**
Ino80_**2.68**
Ahr_**2.67**
Kbtbd2_**2.67**
Kmt2c_**2.65**
Kdm4a_**2.61**
Zfp827_**2.42**
Dmtf1_**2.6**
Egfr_**2.49**
Bmp2k_**2.6**
Rnf4_**2.59**
Fbxo11_**2.58**
Dr1_**2.58**
Prdm2_**2.57**
Zbtb46_**2.45**
Sik3_**2.56**
Notch2_**2.55**
Cdk6_**2.55**
Tsc22d1_**2.55**
Plag1_**2.54**
Brd2_**2.54**
Map4k3_**2.53**
Ikzf5_**2.52**
Hmbox1_**2.52**
Acvr2a_**2.51**
Cggbp1_**2.51**
Kdm3a_**2.5**
Rnf145_**2.48**
Lpin2_**2.48**
Prkcq_**2.26**
Bbx_**2.47**
Zfp160_**2.47**
Mertk_**2.46**
Sik1_**2.44**
Zfp628_**2.43**
Elk4_**2.43**
Crtc2_**2.43**
Hipk2_**2.41**
Zfp213_**2.4**
Siah1a_**2.39**
Pi4k2b_**2.39**
Wac_**2.39**
Klhl25_**2.39**
Grhl1_**2.37**
E2f5_**2.38**
Kmt2a_**2.37**
Ino80d_**2.37**
Ankib1_**2.36**
Rcbtb1_**2.35**
Zfp619_**2.33**
Snw1_**2.33**
Zbtb8a_**2.32**
Mark2_**2.33**
Siah2_**2.31**
Epc2_**2.32**
Rfx5_**2.31**
Neurl3_**2.27**
Ubr5_**2.26**
Foxp1_**2.26**
Med28_**2.25**
Zfp655_**2.25**
Zfp39_**2.25**
Hectd2_**2.21**
Zkscan6_**2.22**
Pfkp_**2.22**
Zfp455_**2.21**
Rcor2_**2.17**
Kitl_**2.21**
Zbtb17_**2.21**
Cdyl_**2.2**
Rbm39_**2.2**
Arhgap22_**2.19**
Riok3_**2.19**
Kctd10_**2.19**
Traf3_**2.19**
Siah1b_**2.16**
Psip1_**2.16**
Wee1_**2.14**
Pik3c2a_**2.14**
Acvr1_**2.14**
Pbx4_**2.1**
Zfp324_**2.12**
Zbtb18_**2.11**
Pphln1_**2.11**
Dcaf6_**2.11**
Med1_**2.1**
Ncoa3_**2.1**
Setd2_**2.09**
Ing3_**2.08**
Akna_**2.06**
Raf1_**2.06**
Trip12_**2.02**
Bcor_**2.02**
Alpk1_**2.01**
Pbx1_**2**

**Table S4. List of 203 Unique Genes in Statistically Significant Functional Clusters within Group 3.** See Table S1 for table legend.

|  | Gene Name_**Log$_2$ Fold-change** |  |
|---|---|---|
| Il12b_**13.73** | Nos2_**13.25** | Il6_**13.15** |
| Cxcl11_**12.87** | Cd69_**12.71** | Gbp4_**12.17** |
| Rasgrp1_**11.42** | Sele_**11.33** | Tnfsf4_**11.62** |
| Dll1_**11.52** | Edn1_**10.61** | Cxcl10_**11.33** |
| Irg1_**11.13** | Lhx2_**10.86** | Adora2a_**10.72** |
| Il27_**10.91** | Ccl5_**10.9** | Tgtp1_**10.35** |
| Csf2_**10.96** | Pou3f1_**10.64** | Cxcl9_**10.5** |
| Vcam1_**10.63** | Tnfsf15_**10.36** | Il1a_**10.5** |
| Ptgs2_**10.46** | Serpina3f_**9.72** | Gbp6_**10.29** |
| Cxcl1_**10.21** | Ccl3_**10.12** | Gfi1_**9.39** |
| Cxcl2_**9.95** | Ifit3b_**9.85** | Csf1_**9.79** |
| Klrk1_**9.17** | Gbp5_**9.66** | Il23r_**9.63** |
| Iigp1_**9.58** | Socs1_**9.41** | Ifit2_**9.47** |
| Il1b_**9.39** | Tnf_**9.35** | Cd274_**9.32** |
| Ccrl2_**9.31** | Tgtp2_**9.26** | Ifi205_**9.14** |
| Mx1_**9.12** | Cd40_**9.11** | Nfkbiz_**9.06** |
| Tnfsf10_**9.03** | Gadd45b_**9.04** | C3_**8.97** |
| Nox1_**8.59** | Cmpk2_**8.82** | Ifit3_**8.73** |
| Dnase1l3_**8.19** | Oasl1_**8.58** | Bcl2a1a_**8.37** |
| Csrnp1_**8.4** | Slc6a4_**8.57** | F3_**8.2** |
| Gm12185_**8.27** | Mx2_**8.32** | Gm4951_**8.18** |
| Plk2_**8.2** | Gbp3_**8.19** | Gm14446_**8.17** |
| Irf1_**8.11** | Ccl12_**8.09** | Rsad2_**8.05** |
| Ifit1_**8.01** | Mmp14_**7.96** | Traf1_**8** |
| Foxf1_**7.69** | Tnfaip8l3_**7.39** | Slfn1_**7.84** |
| Hcar2_**7.81** | Ppp1r15a_**7.83** | Adm_**7.34** |
| Lpar1_**7.75** | Pim1_**7.68** | Gbp2_**7.67** |
| Fpr2_**7.59** | Tnfaip3_**7.66** | Bmp2_**7.6** |
| Spta1_**7.16** | Tnfsf18_**7.36** | Gm4841_**6.96** |
| Cxcl3_**7.33** | Isg20_**7.43** | Saa3_**7.35** |
| Ccl8_**7.15** | Map3k8_**7.12** | Ifih1_**7.1** |
| Il15ra_**7.08** | Rnf152_**6.63** | P2ry13_**7** |
| Itgb8_**6.3** | Il15_**6.94** | Ccl4_**6.93** |
| Nod1_**6.86** | Gbp9_**6.85** | Icam1_**6.84** |
| 2010002M12Rik_**6.73** | Daxx_**6.79** | Cited2_**6.79** |
| Gbp7_**6.75** | Igtp_**6.74** | Tlr11_**6.22** |

| | | |
|---|---|---|
| Il10_**6.68** | Six1_**6.37** | Pdcd1_**7.09** |
| Bmp10_**6.93** | Pyhin1_**6.59** | Irgm2_**6.57** |
| Ifi47_**6.37** | Icosl_**6.29** | Ddx60_**6.28** |
| Tlr3_**6.23** | Peli1_**6.23** | Socs3_**6.21** |
| Helz2_**6.2** | Junb_**6.13** | Rel_**6.12** |
| Rapgef2_**6.05** | Irgm1_**6** | Zbp1_**5.97** |
| Batf2_**5.95** | Tiparp_**5.95** | Clec4e_**5.95** |
| Tnfsf9_**5.94** | Nod2_**5.93** | Flt4_**5.65** |
| Zfp36_**5.75** | Herc6_**5.73** | Irf7_**5.72** |
| Stat2_**5.66** | Trim21_**5.65** | Xcr1_**5.59** |
| Slfn8_**5.58** | Nlrp3_**5.57** | Tagap_**5.54** |
| Zeb1_**5.51** | Atf3_**5.49** | Stat1_**5.5** |
| Mthfr_**5.49** | Pde4b_**5.43** | Gm5431_**5.38** |
| 9930111J21Rik1_**5.33** | Il23a_**4.93** | 3110001I22Rik_**5.29** |
| Slfn3_**5.26** | Parp10_**5.14** | Ddx58_**5.08** |
| Amica1_**4.58** | Fas_**5.05** | Ripk2_**5.04** |
| Ifi203_**5.04** | Themis2_**5.02** | Birc2_**5.01** |
| Ikzf1_**4.98** | Prdm1_**4.97** | Zfp819_**4.54** |
| Birc3_**4.92** | Rgs16_**4.85** | Tlr2_**4.81** |
| Adamts13_**4.45** | 1600014C10Rik_**4.76** | Pml_**4.74** |
| Slfn9_**4.7** | Xaf1_**4.68** | Eif2ak2_**4.66** |
| Slfn2_**4.61** | Ncoa7_**4.61** | Nfkbia_**4.61** |
| H2-Q7_**4.57** | Trex1_**4.56** | Oas1g_**4.54** |
| Egr2_**4.49** | Aim2_**4.44** | Sgk1_**4.4** |
| Ifi204_**4.38** | Trim34a_**4.25** | Oas2_**4.18** |
| Cxcl16_**4.15** | Rnf135_**4.16** | Apobec3_**4.15** |
| Tlr1_**4.07** | Nfkbid_**4.05** | Dusp1_**3.93** |
| Rgs2_**3.85** | Ccnl1_**3.85** | Adar_**3.83** |
| Oasl2_**3.82** | Nupr1_**3.77** | Myd88_**3.58** |
| Irf2_**3.55** | Cdkl5_**3.53** | Il10ra_**3.46** |
| Trim14_**3.31** | Lck_**3.1** | Crlf3_**3.07** |
| Sod2_**2.93** | Ikbke_**2.71** | |

**Table S5. List of 149 Unique Genes in Statistically Significant Functional Clusters Within Group 4.** See Table S1 for table legend.

| Gene Name_**Log$_2$ Fold-change** | | |
|---|---|---|
| Krt16_**9.99** | Inhba_**8.15** | Ccl22_**7.85** |
| Nr3c2_**7.59** | Plagl1_**7.55** | Kalrn_**7.32** |
| Zfhx4_**6.74** | Asap3_**7.17** | En2_**7.55** |

Ciita_**6.85**
Med12l_**6.52**
Il33_**6.5**
Fst_**6.22**
Gata3_**6.34**
Cfb_**6.01**
Dlx1_**5.88**
Cd247_**5.43**
Jak2_**5.96**
Arid5b_**5.92**
Enah_**5.86**
Hoxd1_**6.49**
Klf8_**5.79**
Rgs1_**5.64**
Arid5a_**5.6**
Jdp2_**5.53**
Klf6_**5.53**
Slamf1_**5.04**
Zfp382_**5.46**
Tet2_**5.35**
Sirt1_**5.34**
Malt1_**5.34**
Slamf7_**5.34**
Grhl2_**5.06**
Fzd5_**5.27**
Zbtb10_**5.15**
Pcgf5_**5.12**
Plscr1_**4.97**
Zfp800_**4.92**
Bcl2a1d_**4.74**
Mdm2_**4.8**
Tank_**4.8**
Phip_**4.76**
Ido2_**4.71**
Zhx2_**4.7**
Tap1_**4.63**
Skil_**4.61**
Creb5_**4.59**
Cpeb3_**4.57**
Spic_**4.13**
Txk_**4.31**
Rnf31_**4.47**
Tapbpl_**4.46**
Ascc3_**4.45**
Relb_**4.44**
Chd2_**4.43**
Nfil3_**4.42**
Etv3_**4.38**
Jarid2_**4.35**
Tfap2a_**4.04**
Mycbp2_**4.23**
Smyd1_**4.01**
Azi2_**4.21**
Hinfp_**4.2**
Zc3h12a_**4.2**
Mier3_**4.2**
Med13_**4.18**
Nfkb1_**4.18**
Bcl9_**4.17**
Ccl7_**4.09**
Hivep1_**4.09**
Foxp4_**4.09**
Axl_**4.08**
Zfp281_**4.07**
Zfp319_**4.05**
Rnf19b_**4.03**
H2-Eb1_**4**
Nfib_**4.51**
Nlrc5_**3.97**
Hmgn3_**3.94**
Dhx58_**3.94**
Chd1_**3.93**
Lcor_**3.83**
Agrn_**3.88**
Mier1_**3.86**
Casp4_**3.86**
Samhd1_**3.86**
Tgif1_**3.85**
Phf21a_**3.84**
Lcp2_**3.83**
Ptpn2_**3.83**
Ccl2_**3.81**
Dennd1b_**3.78**
Ankrd17_**3.76**
Etv6_**3.75**
Tap2_**3.75**
Nfkb2_**3.74**
Nck1_**3.68**
Sp110_**3.64**
Irak2_**3.63**
Mefv_**3.55**
Zc3hav1_**3.6**
Usp17le_**3.74**
Epc1_**3.59**
Mb21d1_**3.57**
Tnfsf8_**3.55**
Whsc1l1_**3.54**
Tgs1_**3.54**
Bach1_**3.53**
Tle4_**3.49**
Tcf4_**3.47**
Plagl2_**3.46**
Zfp263_**3.42**
Oas1a_**3.41**
Il18_**3.38**
Trim26_**3.3**
Zfp507_**2.77**
Sp100_**3.23**
Hivep3_**3.2**
Max_**3.18**
Zfp62_**3.18**
Med13l_**3.18**
Trps1_**3.13**
Nampt_**3.11**
Taf7_**3.07**
Maml2_**3.06**
Arid4a_**3.03**
Tlr6_**3.03**
Ikzf2_**2.93**
Ccnl2_**2.94**

Zfp513_**2.93**
F11r_**2.85**
Nrip1_**2.74**
Rgs4_**2.73**
Zfp260_**2.54**
Jag1_**2.47**
Ell2_**2.36**
Ccnt2_**2.85**
Trim13_**2.8**
Zfp654_**2.67**
Zscan29_**2.6**
Zeb2_**2.52**
Keap1_**2.44**
Tcea1_**2.11**
Vasp_**2.85**
Srgap2_**2.78**
Zfp691_**2.66**
Ccr7_**2.83**
Sema4d_**2.48**
Oas3_**2.43**

# REFERENCE LIST

Afgan E, Baker D, van den Beek M, Blankenberg D, Bouvier D, Čech M, Chilton J, Clements D, Coraor N, Eberhard C, *et al*. 2016. The Galaxy platform for accessible, reproducible and collaborative biomedical analyses: 2016 update. Nucleic Acids Res. 44(W1):W3–W10. doi:10.1093/nar/gkw343.

Almeida JD, Tyrrell DAJ. 1967. The morphology of three previously uncharacterized human respiratory viruses that grow in organ culture. J Gen Virol. 1:175–178. doi:10.1099/0022-1317-1-2-175.

Amarasinghe A, Abdul-Cader MS, Nazir S, De Silva Senapathi U, Van Der Meer F, Cork SC, Gomis S, Abdul-Careem MF. 2017. Infectious bronchitis corona virus establishes productive infection in avian macrophages interfering with selected antimicrobial functions. PLOS ONE. 12(8):e0181801. doi: 10.1371/journal.pone.0181801.

Bang FB, Warwick. 1960. Mouse macrophages as host cells for the mouse hepatitis virus and the genetic basis of their susceptibility. Proc Natl Acad Sci U S A. 46(8):1065–1075.

Barretto N, Jukneliene D, Ratia K, Chen Z, Mesecar AD, Baker SC. 2005. The papain-like protease of severe acute respiratory syndrome coronavirus has deubiquitinating activity. J Virol. 79(24):15189–15198. doi:10.1128/JVI.79.24.15189-15198.2005.

Bechill J, Chen Z, Brewer JW, Baker SC. 2008. Coronavirus infection modulates the unfolded protein response and mediates sustained translational repression. J Virol. 82(9):4492–4501. doi:10.1128/JVI.00017-08.

Bhardwaj K, Guarino L, Kao CC. 2004. The severe acute respiratory syndrome coronavirus nsp15 protein is an endoribonuclease that prefers manganese as a cofactor. J Virol. 78(22):12218–12224. doi:10.1128/JVI.78.22.12218-12224.2004.

Bhardwaj K, Sun J, Holzenburg A, Guarino LA, Kao CC. 2006. RNA recognition and cleavage by the SARS coronavirus endoribonuclease. J Mol Biol. 361(2):243–256. doi:10.1016/j.jmb.2006.06.021.

Bhoj VG, Chen ZJ. 2009. Ubiquitylation in innate and adaptive immunity. Nature. 458(7237):430–437. doi:10.1038/nature07959.

Bibeau-Poirier A, Servant MJ. 2008. Roles of ubiquitination in pattern-recognition receptors and type I interferon receptor signaling. Cytokine. 43(3):359–367. doi:10.1016/j.cyto.2008.07.012.

Bogdan C, Mattner J, Schleicher U. 2004. The role of type I interferons in non-viral infections. Immunol Rev. 202(1):33–48. doi:10.1111/j.0105-2896.2004.00207.x.

Cameron MJ, Kelvin AA, Leon AJ, Cameron CM, Ran L, Xu L, Chu Y-K, Danesh A, Fang Y, Li Q, *et al*. 2012. Lack of innate interferon responses during SARS coronavirus infection in a vaccination and reinfection ferret model. PLOS ONE. 7(9):e45842. doi:10.1371/journal.pone.0045842.

Cervantes-Barragán L, Kalinke U, Züst R, König M, Reizis B, López-Macías C, Thiel V, Ludewig B. 2009. Type I IFN-mediated protection of macrophages and dendritic cells secures control of murine coronavirus infection. J Immunol. 182(2):1099–1106. doi:10.4049/jimmunol.182.2.1099.

Chan JFW, Lau SKP, To KKW, Cheng VCC, Woo PCY, Yue K-Y. 2015. Middle East respiratory syndrome coronavirus: another zoonotic betacoronavirus causing SARS-like disease. Clin Microbiol Rev. 28(2):465–522. doi:10.1128/CMR.00102-14.

Channappanavar R, Fehr AR, Vijay R, Mack M, Zhao J, Meyerholz DK, Perlman S. 2016. Dysregulated type I interferon and inflammatory monocyte-macrophage responses cause lethal pneumonia in SARS-CoV-infected mice. Cell Host Microbe. 19(2):181–193. doi:10.1016/J.CHOM.2016.01.007.

Chen Y, Savinov SN, Mielech AM, Cao T, Baker SC, Mesecar AD. 2015. X-ray structural and functional studies of the three tandemly linked domains of non-structural protein 3 (nsp3) from Murine hepatitis virus reveal conserved functions. J Biol Chem. 290(42):25293–25306. doi:10.1074/jbc.M115.662130.

Cheung CY, Poon LLM, Ng IHY, Luk W, Sia S-F, Wu MHS, Chan K-H, Yuen K-Y, Gordon S, Guan Y, *et al*. 2005. Cytokine responses in severe acute respiratory syndrome coronavirus-infected macrophages in vitro: possible relevance to pathogenesis. J Virol. 79(12):7819–7826. doi:10.1128/JVI.79.12.7819-7826.2005.

Cho Y, Yoon KJ. 2014. An overview of calf diarrhea - infectious etiology, diagnosis, and intervention. J Vet Sci. 15(1):1–17. doi:10.4142/jvs.2014.15.1.1.

Clementz MA, Chen Z, Banach BS, Wang Y, Sun L, Ratia K, Baez-Santos YM, Wang J, Takayama J, Ghosh AK, *et al*. 2010. Deubiquitinating and interferon antagonism activities of coronavirus papain-like proteases. J Virol. 84(9):4619–4629. doi:10.1128/JVI.02406-09.

Coleman CM, Sisk JM, Halasz G, Zhong J, Beck SE, Matthews KL, Venkataraman T, Rajagopalan S, Kyratsous CA, Frieman MB. 2017. CD8 + T cells and macrophages regulate pathogenesis in a mouse model of Middle East respiratory syndrome. J Virol. 91(1):e01825-16. doi:10.1128/JVI.01825-16.

Collins AR. 2002. In vitro detection of apoptosis in monocytes/macrophages infected with human coronavirus. Clin Diagn Lab Immunol. 9(6):1392–1395. doi:10.1128/CDLI.9.6.1392-1395.2002.

Cong F, Liu X, Han Z, Shao Y, Kong X, Liu S. 2013. Transcriptome analysis of chicken kidney tissues following coronavirus avian infectious bronchitis virus infection. BMC Genomics. 14:743. doi:10.1186/1471-2164-14-743.

Cruz JLG, Becares M, Sola I, Oliveros JC, Enjuanes L, Zúñiga S. 2013. Alphacoronavirus protein 7 modulates host innate immune response. J Virol. 87(17):9754–9767. doi:10.1128/JVI.01032-13.

DeDiego ML, Nieto-Torres JL, Jiménez-Guardeño JM, Regla-Nava JA, Álvarez E, Oliveros JC, Zhao J, Fett C, Perlman S, Enjuanes L. 2011. Severe acute respiratory syndrome coronavirus envelope protein regulates cell stress response and apoptosis. PLOS Pathog. 7(10):e1002315. doi:10.1371/journal.ppat.1002315.

DeDiego ML, Nieto-Torres JL, Jimenez-Guardeño JM, Regla-Nava JA, Castaño-Rodriguez C, Fernandez-Delgado R, Usera F, Enjuanes L. 2014. Coronavirus virulence genes with main focus on SARS-CoV envelope gene. Virus Res. 194:124–137. doi:10.1016/j.virusres.2014.07.024.

de Hoon MJL, Imoto S, Nolan J, Miyano S. 2004. Open source clustering software. Bioinformatics. 20(9):1453–1454. doi:10.1093/bioinformatics/bth078.

Deng J, Lu PD, Zhang Y, Scheuner D, Kaufman RJ, Sonenberg N, Harding HP, Ron D. 2004. Translational repression mediates activation of nuclear factor kappa B by phosphorylated translation initiation factor 2. Mol Cell Biol. 24(23):10161–10168. doi:10.1128/MCB.24.23.10161-10168.2004.

Deng X, Baker SC. 2018. An “old” protein with a new story: coronavirus endoribonuclease is important for evading host antiviral defenses. Virology. 517:157–163. doi:10.1016/j.virol.2017.12.024.

Deng X, Hackbart M, Mettelman RC, O’Brien A, Mielech AM, Yi G, Kao CC, Baker SC. 2017. Coronavirus nonstructural protein 15 mediates evasion of dsRNA sensors and limits apoptosis in macrophages. Proc Natl Acad Sci U S A. 114(21):E4251–E4260. doi:10.1073/pnas.1618310114.

Devaux P, Hudacek AW, Hodge G, Reyes-Del Valle J, Mcchesney MB, Cattaneo R. 2011. A recombinant measles virus unable to antagonize STAT1 function cannot control inflammation and is attenuated in rhesus monkeys. J Virol. 85(1):348–356. doi:10.1128/JVI.00802-10.

de Wit E, van Doremalen N, Falzarano D, Munster VJ. 2016. SARS and MERS: recent insights into emerging coronaviruses. Nat Rev Microbiol. 14(8):523–534. doi:10.1038/nrmicro.2016.81.

Dijkman R, van der Hoek L. 2009. Human coronaviruses 229E and NL63: close yet still so far. J Formos Med Assoc. 108(4):270–279. doi:10.1016/S0929-6646(09)60066-8.

Du Y, Xin L, Shi Y, Zhang TH, Wu NC, Dai L, Gong D, Brar G, Shu S, Luo J, *et al*. 2018. Genome-wide identification of interferon-sensitive mutations enables influenza vaccine design. Science. 359(6373):290–296. doi:10.1126/science.aan8806.

Elliott R, Li F, Dragomir I, Chua MMW, Gregory BD, Weiss SR. 2013. Analysis of the host transcriptome from demyelinating spinal cord of murine coronavirus-infected mice. PLOS ONE. 8(9):e75346. doi:10.1371/journal.pone.0075346.

Falzarano D, de Wit E, Feldmann F, Rasmussen AL, Okumura A, Peng X, Thomas MJ, van Doremalen N, Haddock E, Nagy L, *et al*. 2014. Infection with MERS-CoV causes lethal pneumonia in the common marmoset. PLOS Pathog. 10(8):e1004250. doi:10.1371/journal.ppat.1004250.

Frias-Staheli N, Giannakopoulos N V., Kikkert M, Taylor SL, Bridgen A, Paragas J, Richt JA, Rowland RR, Schmaljohn CS, Lenschow DJ, *et al*. 2007. Ovarian tumor domain-containing viral proteases evade ubiquitin- and ISG15-dependent innate immune responses. Cell Host Microbe. 2(6):404–416. doi:10.1016/j.chom.2007.09.014.

Frieman M, Ratia K, Johnston RE, Mesecar AD, Baric RS. 2009. Severe acute respiratory syndrome coronavirus papain-like protease ubiquitin-like domain and catalytic domain regulate antagonism of IRF3 and NF-κB signaling. J Virol. 83(13):6689–6705. doi:10.1128/JVI.02220-08.

Frieman M, Yount B, Heise M, Kopecky-Bromberg SA, Palese P, Baric RS. 2007. Severe acute respiratory syndrome coronavirus ORF6 antagonizes STAT1 function by sequestering nuclear import factors on the rough endoplasmic reticulum/Golgi membrane. J Virol. 81(18):9812–9824. doi:10.1128/JVI.01012-07.

Fuchs SY. 2012. Ubiquitination-mediated regulation of interferon responses. Growth Factors. 30(3):141–148. doi:10.3109/08977194.2012.669382.

Fujimoto I, Pan J, Takizawa T, Nakanishi Y. 2000. Virus clearance through apoptosis-dependent phagocytosis of influenza A virus-infected cells by macrophages. J Virol. 74(7):3399–3403. doi:10.1128/JVI.74.7.3399-3403.2000.

Fung TS, Liao Y, Liu DX. 2014. The endoplasmic reticulum stress sensor IRE1 protects cells from apoptosis induced by the coronavirus infectious bronchitis virus. J Virol. 88(21):12752–12764. doi:10.1128/JVI.02138-14.

Fung TS, Liao Y, Liu DX. 2016. Regulation of stress responses and translational control by coronavirus. Viruses. 8(7):184. doi:10.3390/v8070184.

Fung TS, Liu DX. 2014. Coronavirus infection, ER stress, apoptosis and innate immunity. Front Microbiol. 5:296. doi:10.3389/fmicb.2014.00296.

Gaunt ER, Hardie A, Claas ECJ, Simmonds P, Templeton KE. 2010. Epidemiology and clinical presentations of the four human coronaviruses 229E, HKU1, NL63, and OC43 detected over 3 years using a novel multiplex real-time PCR method. J Clin Microbiol. 48(8):2940–2947. doi:10.1128/JCM.00636-10.

Gorbalenya AE, Enjuanes L, Ziebuhr J, Snijder EJ. 2006. Nidovirales: evolving the largest RNA virus genome. Virus Res. 117(1):17–37. doi:10.1016/j.virusres.2006.01.017.

Gosert R, Kanjanahaluethai A, Egger D, Bienz K, Baker SC. 2002. RNA replication of mouse hepatitis virus takes place at double-membrane vesicles. J Virol. 76(8):3697–3708. doi:10.1128/JVI.76.8.3697–3708.2002.

Haller O, Kochs G, Weber F. 2006. The interferon response circuit: induction and suppression by pathogenic viruses. Virology. 344(1):119–130. doi:10.1016/J.VIROL.2005.09.024.

Hartwig SM, Holman KM, Varga SM. 2014. Depletion of alveolar macrophages ameliorates virus-induced disease following a pulmonary coronavirus infection. PLOS ONE. 9(3):e90720. doi:10.1371/journal.pone.0090720.

Harun MSR, Kuan CO, Selvarajah GT, Wei TS, Arshad SS, Bejo MH, Omar AR. 2013. Transcriptional profiling of feline infectious peritonitis virus infection in CRFK cells and in PBMCs from FIP diagnosed cats. Virol J. 10:329. doi:10.1186/1743-422X-10-329.

Heaton SM, Borg NA, Dixit VM. 2016. Ubiquitin in the activation and attenuation of innate antiviral immunity. J Exp Med. 213(1):1–13. doi:10.1084/jem.20151531.

Hsu L-C, Mo Park J, Zhang K, Luo J-L, Maeda S, Kaufman RJ, Eckmann L, Guiney DG, Karin M. 2004. The protein kinase PKR is required for macrophage apoptosis after activation of Toll-like receptor 4. Nature. 428(6980):341–345. doi:10.1038/nature02405.

Hu F, Yu X, Wang H, Zuo D, Guo C, Yi H, Tirosh B, Subjeck JR, Qiu X, Wang XY. 2011. ER stress and its regulator X-box-binding protein-1 enhance polyIC-induced innate immune response in dendritic cells. Eur J Immunol. 41(4):1086–1097. doi:10.1002/eji.201040831.

Huang DW, Sherman BT, Lempicki RA. 2009a. Bioinformatics enrichment tools: paths toward the comprehensive functional analysis of large gene lists. Nucleic Acids Res. 37(1):1–13. doi:10.1093/nar/gkn923.

Huang DW, Sherman BT, Lempicki RA. 2009b. Systematic and integrative analysis of large gene lists using DAVID bioinformatics resources. Nat Protoc. 4(1):44–57. doi:10.1038/nprot.2008.211.

Hui DS, Memish ZA, Zumla A. 2014. Severe acute respiratory syndrome vs. the Middle East respiratory syndrome. Curr Opin Pulm Med. 20(3):233–241. doi:10.1097/MCP.0000000000000046.

Irigoyen N, Firth AE, Jones JD, Chung BYW, Siddell SG, Brierley I. 2016. high-resolution analysis of coronavirus gene expression by RNA sequencing and ribosome profiling. PLOS Pathog. 12(2):e1005473. doi:10.1371/journal.ppat.1005473.

Irigoyen N, Franaszek K, Dinan AM, Moore NA, Siddell SG, Brierley I, Firth AE. 2018. Activation of the unfolded protein response and inhibition of translation initiation during coronavirus infection. bioRxiv. 292979 [preprint]. Updated May 12, 2018. doi:10.1101/292979.

Ivanov KA, Hertzig T, Rozanov M, Bayer S, Thiel V, Gorbalenya AE, Ziebuhr J. 2004. Major genetic marker of nidoviruses encodes a replicative endoribonuclease. Proc Natl Acad Sci. 101(34):12694–12699. doi:10.1073/pnas.0403127101.

Ivashkiv LB, Donlin LT. 2014. Regulation of type I interferon responses. Nat Rev Immunol. 14(1):36–49. doi:10.1038/nri3581.

Josset L, Menachery VD, Gralinski LE, Agnihothram S, Sova P, Carter VS, Yount BL, Graham RL, Baric RS, Katzea MG. 2013. Cell host response to infection with novel human coronavirus EMC predicts potential antivirals and important differences with SARS coronavirus. MBio. 4(3):e00165-13. doi:10.1128/mBio.00165-13.

Josset L, Tchitchek N, Gralinski LE, Ferris MT, Eisfeld AJ, Green RR, Thomas MJ, Tisoncik-Go J, Schroth GP, Kawaoka Y, *et al*. 2014. Annotation of long non-coding RNAs expressed in Collaborative Cross founder mice in response to respiratory virus infection reveals a new class of interferon-stimulated transcripts. RNA Biol. 11(7):875–890. doi:10.4161/rna.29442.

Kang H, Bhardwaj K, Li Y, Palaninathan S, Sacchettini J, Guarino L, Leibowitz JL, Cheng Kao C. 2007. Biochemical and genetic analyses of murine hepatitis virus nsp15 endoribonuclease. J Virol. 81(24):13587–13597. doi:10.1128/JVI.00547-07.

Kim D, Langmead B, Salzberg SL. 2015. HISAT: a fast spliced aligner with low memory requirements. Nat Methods. 12(4):357–360. doi:10.1038/nmeth.3317.

Kindler E, Gil-Cruz C, Spanier J, Li Y, Wilhelm J, Rabouw HH, Züst R, Hwang M, V'kovski P, Stalder H, *et al*. 2017. Early endonuclease-mediated evasion of RNA sensing ensures efficient coronavirus replication. PLOS Pathog. 13(2):e1006195. doi:10.1371/journal.ppat.1006195.

Knoops K, Kikkert M, van den Worm SHE, Zevenhoven-Dobbe JC, van der Meer Y, Koster AJ, Mommaas AM, Snijder EJ. 2008. SARS-coronavirus replication is supported by a reticulovesicular network of modified endoplasmic reticulum. PLOS Biol. 6(9):1957–1974. doi:10.1371/journal.pbio.0060226.

Kroetz DN, Allen RM, Schaller MA, Cavallaro C, Ito T, Kunkel SL. 2015. Type I interferon induced epigenetic regulation of macrophages suppresses innate and adaptive immunity in acute respiratory viral infection. PLOS Pathog. 11(12). doi:10.1371/journal.ppat.1005338.

Kuo L, Koetzner CA, Masters PS. 2016. A key role for the carboxy-terminal tail of the murine coronavirus nucleocapsid protein in coordination of genome packaging. Virology. 494:100–107. doi:10.1016/J.VIROL.2016.04.009.

Labzin LI, Schmidt S V., Masters SL, Beyer M, Krebs W, Klee K, Stahl R, Lütjohann D, Schultze JL, Latz E, *et al*. 2015. ATF3 is a key regulator of macrophage IFN responses. J Immunol. 195(9):4446–4455. doi:10.4049/jimmunol.1500204.

Laurent-Rolle M, Boer EF, Lubick KJ, Wolfinbarger JB, Carmody AB, Rockx B, Liu W, Ashour J, Shupert WL, Holbrook MR, *et al*. 2010. The NS5 protein of the virulent West Nile virus NY99 strain is a potent antagonist of type I interferon-mediated JAK-STAT signaling. J Virol. 84(7):3503–3515. doi:10.1128/JVI.01161-09.

Lee C. 2015. Porcine epidemic diarrhea virus: an emerging and re-emerging epizootic swine virus. Virol J. 12:193. doi:10.1186/s12985-015-0421-2.

Lei J, Kusov Y, Hilgenfeld R. 2018. Nsp3 of coronaviruses: structures and functions of a large multi-domain protein. Antiviral Res. 149:58–74. doi:10.1016/j.antiviral.2017.11.001.

Lei Y, Moore CB, Liesman RM, O'Connor BP, Bergstralh DT, Chen ZJ, Pickles RJ, Ting JP-Y. 2013. MAVS-mediated apoptosis and its inhibition by viral proteins. PLOS ONE. 4(5):e5466. doi:10.1371/journal.pone.0005466.

Liao Y, Smyth GK, Shi W. 2014. featureCounts: an efficient general purpose program for assigning sequence reads to genomic features. Bioinformatics. 30(7):923–930. doi:10.1093/bioinformatics/btt656.

Lindner HA, Fotouhi-Ardakani N, Lytvyn V, Lachance P, Sulea T, Ménard R. 2005. The papain-like protease from the severe acute respiratory syndrome coronavirus is a deubiquitinating enzyme. J Virol. 79(24):15199–15208. doi:10.1128/JVI.79.24.15199-15208.2005.

Liu H, Yang X, Zhang Z, Li J, Zou W, Zeng F, Wang H. 2017. Comparative transcriptome analysis reveals induction of apoptosis in chicken kidney cells associated with the virulence of nephropathogenic infectious bronchitis virus. Microb Pathog. 113:451–459. doi:10.1016/j.micpath.2017.11.031.

Liu X, Zhu L, Liao S, Xu Z, Zhou Y. 2015. The porcine microRNA transcriptome response to transmissible gastroenteritis virus infection. PLOS ONE. 10(3):e0120377. doi:10.1371/journal.pone.0120377

Love MI, Huber W, Anders S. 2014. Moderated estimation of fold change and dispersion for RNA-seq data with DESeq2. Genome Biol. 15(12):550. doi:10.1186/s13059-014-0550-8.

McDermott JE, Mitchell HD, Gralinski LE, Eisfeld AJ, Josset L, Bankhead A, Neumann G, Tilton SC, Schäfer A, Li C, *et al*. 2016. The effect of inhibition of PP1 and TNFα signaling on pathogenesis of SARS coronavirus. BMC Syst Biol. 10(1):93. doi:10.1186/s12918-016-0336-6.

Menachery VD, Eisfeld AJ, Schäfer A, Josset L, Sims AC, Proll S, Fan S, Li C, Neumann G, Tilton SC, *et al*. 2014. Pathogenic influenza viruses and coronaviruses utilize similar and contrasting approaches to control interferon-stimulated gene responses. MBio. 5(3):e01174-14. doi:10.1128/mBio.01174-14.

Menachery VD, Gralinski LE, Mitchell HD, Dinnon III KH, Yount Jr. BL, McAnarney ET, Graham RL, Waters KM, Baric RS. 2018. Combination attenuation offers strategy for live-attenuated coronavirus vaccines. J Virol (forthcoming). doi:10.1128/JVI.00710-18.

Menachery VD, Gralinski LE, Mitchell HD, Dinnon III KH, Leist SR, Yount Jr. BL, Graham RL, McAnarney ET, Stratton KG, Cockrell AS, et al. 2017. Middle East respiratory syndrome coronavirus nonstructural protein 16 is necessary for interferon resistance and viral pathogenesis. mSphere. 2(6):e00346-17. doi:10.1128/mSphere.00346-17.

Menachery VD, Mitchell HD, Cockrell AS, Gralinski LE, Yount Jr. BL, Graham RL, McAnarney ET, Douglas MG, Scobey T, Beall A, *et al*. 2017. MERS-CoV accessory ORFs play key role for infection and pathogenesis. MBio. 8(4):e00665-17. doi:10.1128/mBio.00665-17.

Mielech AM, Chen Y, Mesecar AD, Baker SC. 2014. Nidovirus papain-like proteases: multifunctional enzymes with protease, deubiquitinating and deISGylating activities. Virus Res. 194:184–190. doi:10.1016/j.virusres.2014.01.025.

Mielech AM, Kilianski A, Baez-Santos YM, Mesecar AD, Baker SC. 2014. MERS-CoV papain-like protease has deISGylating and deubiquitinating activities. Virology. 450–451:64–70. doi:10.1016/j.virol.2013.11.040.

Mogensen TH, Melchjorsen J, Höllsberg P, Paludan SR. 2003. Activation of NF-κB in virus-infected macrophages is dependent on mitochondrial oxidative stress and intracellular calcium: downstream involvement of the kinases TGF-β-activated kinase 1, mitogen-activated kinase/extracellular signal-regulated kinase kinase 1, and IκB kinase. J Immunol. 170(12):6224–6233. doi:10.4049/jimmunol.170.12.6224.

Nga PT, de Parquet MC, Lauber C, Parida M, Nabeshima T, Yu F, Thuy NT, Inoue S, Ito T, Okamoto K, *et al*. 2011. Discovery of the first insect nidovirus, a missing evolutionary link in the emergence of the largest RNA virus genomes. PLOS Pathog. 7(9):e1002215. doi:10.1371/journal.ppat.1002215.

Paolini R, Bernardini G, Molfetta R, Santoni A. 2015. NK cells and interferons. Cytokine Growth Factor Rev. 26(2):113–120. doi:10.1016/j.cytogfr.2014.11.003.

Pedersen NC. 2014. An update on feline infectious peritonitis: diagnostics and therapeutics. Vet J. 201(2):133–141. doi:10.1016/j.tvjl.2014.04.016.

Peng X, Gralinski L, Ferris MT, Frieman MB, Thomas MJ, Proll S, Korth MJ, Tisoncik JR, Heise M, Luo S, *et al*. 2011. Integrative deep sequencing of the mouse lung transcriptome reveals differential expression of diverse classes of small RNAs in response to respiratory virus infection. MBio. 2(6):e00198-11. doi:10.1128/mBio.00198-11.

Perlman S, Netland J. 2009. Coronaviruses post-SARS: update on replication and pathogenesis. Nat Rev Microbiol. 7(6):439–450. doi:10.1038/nrmicro2147.

Pertsovskaya I, Abad E, Domedel-Puig N, Garcia-Ojalvo J, Villoslada P. 2013. Transient oscillatory dynamics of interferon beta signaling in macrophages. BMC Syst Biol. 7(59). doi:10.1186/1752-0509-7-59.

Poppe M, Wittig S, Jurida L, Bartkuhn M, Wilhelm J, Müller H, Beuerlein K, Karl N, Bhuju S, Ziebuhr J, *et al*. 2017. The NF-κB-dependent and -independent transcriptome and chromatin landscapes of human coronavirus 229E-infected cells. PLOS Pathog. 13(3):e1006286. doi:10.1371/journal.ppat.1006286.

Raaben M, Groot Koerkamp MJA, Rottier PJM, de Haan CAM. 2007. Mouse hepatitis coronavirus replication induces host translational shutoff and mRNA decay, with concomitant formation of stress granules and processing bodies. Cell Microbiol. 9(9):2218–2229. doi:10.1111/j.1462-5822.2007.00951.x.

Rabouw HH, Langereis MA, Knaap RCM, Dalebout TJ, Canton J, Sola I, Enjuanes L, Bredenbeek PJ, Kikkert M, de Groot RJ, *et al*. 2016. Middle East respiratory coronavirus accessory protein 4a inhibits PKR-mediated antiviral stress responses. PLOS Pathog. 12(10):e1005982. doi:10.1371/journal.ppat.1005982.

Reineke LC, Kedersha N, Langereis MA, van Kuppeveld FJM, Lloyd RE. 2015. Stress granules regulate double-stranded RNA-dependent protein kinase activation through a complex containing G3BP1 and Caprin1. MBio. 6(2):e02486-14. doi:10.1128/mBio.02486-14.

Ricagno S, Egloff M-P, Ulferts R, Coutard B, Nurizzo D, Campanacci V, Cambillau C, Ziebuhr J, Canard B. 2006. Crystal structure and mechanistic determinants of SARS coronavirus nonstructural protein 15 define an endoribonuclease family. Proc Natl Acad Sci U S A. 103(32):11892–11897. doi:10.1073/pnas.0601708103.

RStudio Team. 2015. RStudio: Integrated Development for R. R Studio, Inc., Boston, MA.

Saldanha AJ. 2004. Java Treeview—extensible visualization of microarray data. Bioinformatics. 20(17):3246–3248. doi:10.1093/bioinformatics/bth349.

Savarin C, Dutta R, Bergmann CC. 2018. Distinct gene profiles of bone marrow-derived macrophages and microglia during neurotropic coronavirus-induced demyelination. Front Immunol. 9:1325. doi:10.3389/fimmu.2018.01325.

Schneider WM, Chevillotte MD, Rice CM. 2014. Interferon-stimulated genes: a complex web of host defenses. Annu Rev Immunol. 32:513–45. doi:10.1146/annurev-immunol-032713-120231.

Schoggins JW, Rice CM. 2011. Interferon-stimulated genes and their antiviral effector functions. Curr Opin Virol. 1(6):519–525. doi:10.1016/j.coviro.2011.10.008.

Schroeder A, Mueller O, Stocker S, Salowsky R, Leiber M, Gassmann M, Lightfoot S, Menzel W, Granzow M, Ragg T. 2006. The RIN: an RNA integrity number for assigning integrity values to RNA measurements. BMC Mol Biol. 7(3). doi:10.1186/1471-2199-7-3.

Schulz KS, Mossman KL. 2016. Viral evasion strategies in type I IFN signaling - a summary of recent developments. Front Immunol. 7:498. doi:10.3389/fimmu.2016.00498.

Shirato K, Chang H-W, Rottier PJM. 2018. Differential susceptibility of macrophages to serotype II feline coronaviruses correlates with differences in the viral spike protein. Virus Res. 255:14–23. doi:10.1016/j.virusres.2018.06.010.

Simmons JD, Wollish AC, Heise MT. 2010. A determinant of sindbis virus neurovirulence enables efficient disruption of Jak/STAT signaling. J Virol. 84(21):11429–11439. doi:10.1128/JVI.00577-10.

Siu K-L, Chan C-P, Kok K-H, Woo PC-Y, Jin D-Y. 2014. Comparative analysis of the activation of unfolded protein response by spike proteins of severe acute respiratory syndrome coronavirus and human coronavirus HKU1. Cell Biosci. 4(1):3. doi:10.1186/2045-3701-4-3.

Smith JA. 2014. A new paradigm: innate immune sensing of viruses via the unfolded protein response. Front Microbiol. 5:222. doi:10.3389/fmicb.2014.00222.

Sulea T, Lindner HA, Purisima EO, Ménard R. 2005. Deubiquitination, a new function of the severe acute respiratory syndrome coronavirus papain-like protease? J Virol. 79(7):4550–4551. doi:10.1128/JVI.79.7.4550-4551.2005.

Sun Z, Chen Z, Lawson SR, Fang Y. 2010. The cysteine protease domain of porcine reproductive and respiratory syndrome virus nonstructural protein 2 possesses deubiquitinating and interferon antagonism functions. J Virol. 84(15):7832–7846. doi:10.1128/JVI.00217-10.

Sunniva Oma V, Tråvén M, Alenius S, Myrmel M, Stokstad M. 2016. Bovine coronavirus in naturally and experimentally exposed calves; viral shedding and the potential for transmission. Virol J. 13:100. doi:10.1186/s12985-016-0555-x.

Talon J, Salvatore M, O'Neill RE, Nakaya Y, Zheng H, Muster T, Garcia-Sastre A, Palese P. 2000. Influenza A and B viruses expressing altered NS1 proteins: a vaccine approach. Proc Natl Acad Sci U S A. 97(8):4309–4314. doi:10.1073/pnas.070525997.

Tam AB, Mercado EL, Hoffmann A, Niwa M. 2012. ER stress activates NF-κB by integrating functions of basal IKK activity, IRE1 and PERK. PLOS ONE. 7(10):e45078. doi:10.1371/journal.pone.0045078.

Teng M. 2012. The non-structural proteins of RSV: targeting interferon antagonists for vaccine development. Infect Disord Drug Targets. 12(2):129–137. doi:10.2174/187152612800100170.

Thompson MR, Kaminski JJ, Kurt-Jones EA, Fitzgerald KA. 2011. Pattern recognition receptors and the innate immune response to viral infection. Viruses. 3(6):920–940. doi:10.3390/v3060920.

van Kasteren PB, Beugeling C, Ninaber DK, Frias-Staheli N, van Boheemen S, García-Sastre A, Snijder EJ, Kikkert M. 2012. Arterivirus and nairovirus ovarian tumor domain-containing deubiquitinases target activated RIG-I to control innate immune signaling. J Virol. 86(2):773–785. doi:10.1128/JVI.06277-11.

VanLeuven JT, Ridenhour BJ, Gonzalez AJ, Miller CR, Miura TA. 2017. Lung epithelial cells have virus-specific and shared gene expression responses to infection by diverse respiratory viruses. PLOS ONE. 12(6):e0178408. doi:10.1371/journal.pone.0178408.

Venkataraman T, Coleman CM, Frieman MB. 2017. overactive epidermal growth factor receptor signaling leads to increased fibrosis after severe acute respiratory syndrome coronavirus infection. J Virol. 91(12):e00182-17. doi:10.1128/JVI.00182-17.

Versteeg GA, Slobodskaya O, Spaan WJM. 2006. Transcriptional profiling of acute cytopathic murine hepatitis virus infection in fibroblast-like cells. J Gen Virol. 87(7):1961–1975. doi:10.1099/vir.0.81756-0.

Virelizier JL, Allison AC. 1976. Correlation of persistent mouse hepatitis virus (MHV-3) infection with its effect on mouse macrophage cultures. Arch Virol. 50(4): 279–285.

Virology: coronaviruses. 1968. Nature. 220(5168):650.

Wang G, Chen G, Zheng D, Cheng G, Tang H. 2011. PLP2 of mouse hepatitis Virus A59 (MHV-A59) targets TBK1 to negatively regulate cellular type I interferon signaling pathway. PLOS ONE. 6(2):e17192. doi:10.1371/journal.pone.0017192.

Wang X, Rosa AJM, Oliverira HN, Rosa GJM, Guo X, Travnicek M, Girshick T. 2006. Transcriptome of local innate and adaptive immunity during early phase of infectious bronchitis viral infection. Viral Immunol. 19(4):768–774. doi:10.1089/vim.2006.0051.

Warnes GR, Bolker B, Bonebakker L, Gentleman R, Liaw WHA, Lumley T, Maechler M, Magnusson A, Moeller S, Schwartz M, *et al*. 2016. gplots: Various R Programming Tools for Plotting Data. https://CRAN.R-project.org/package=gplots.

Wu J, Rutkowski DT, Dubois M, Swathirajan J, Saunders T, Wang J, Song B, Yau G-DY, Kaufman RJ. 2007. ATF6α optimizes long-term endoplasmic reticulum function to protect cells from chronic stress. Dev Cell. 13(3):351–364. doi:10.1016/j.devcel.2007.07.005.

Xing Y, Chen J, Tu J, Zhang B, Chen X, Shi H, Baker SC, Feng L, Chen Z. 2013. The papain-like protease of porcine epidemic diarrhea virus negatively regulates type I interferon pathway by acting as a viral deubiquitinase. J Gen Virol. 94(Pt7):1554–1567. doi:10.1099/vir.0.051169-0.

Xiong H, Morrison J, Ferris MT, Gralinski LE, Whitmore AC, Green R, Thomas MJ, Tisoncik-Go J, Schroth GP, Pardo-Manuel de Villena F, *et al*. 2014. Genomic profiling of Collaborative Cross founder mice infected with respiratory viruses reveals novel transcripts and infection-related strain-specific gene and isoform expression. G3 (Bethesda). 4(8):1429–1444. doi:10.1534/g3.114.011759.

Xu C, Bailly-Maitre B, Reed JC. 2005. Endoplasmic reticulum stress: cell life and death decisions. J Clin Invest. 115(10):2656–2664. doi:10.1172/JCI26373.

Yilla M, Harcourt BH, Hickman CJ, McGrew M, Tamin A, Goldsmith CS, Bellini WJ, Anderson LJ. 2005. SARS-coronavirus replication in human peripheral monocytes/macrophages. Virus Res. 107(1):93–101. doi:10.1016/j.virusres.2004.09.004.

Yoneda M, Guillaume V, Sato H, Fujita K, Georges-Courbot M-C, Ikeda F, Omi M, Muto-Terao Y, Wild TF, Kai C. 2010. The nonstructural proteins of Nipah virus play a key role in pathogenicity in experimentally infected animals. PLOS ONE. 5(9):e12709. doi:10.1371/journal.pone.0012709.

Yount B, Denison MR, Weiss SR, Baric RS. 2002. systematic assembly of a full-length infectious cDNA of mouse hepatitis virus strain A59. J Virol. 76(21):11065–11078. doi:10.1128/JVI.76.21.11065-11078.2002.

Zheng D, Chen G, Guo B, Cheng G, Tang H. 2008. PLP2, a potent deubiquitinase from murine hepatitis virus, strongly inhibits cellular type I interferon production. Cell Res. 18(11):1105–1113. doi:10.1038/cr.2008.294.

Zhou H, Zhao J, Perlman S. 2010. Autocrine interferon priming in macrophages but not dendritic cells results in enhanced cytokine and chemokine production after coronavirus infection. MBio. 1(4):e00219-10. doi:10.1128/mBio.00219-10.

Zhou J, Chu H, Li C, Wong BH-Y, Cheng ZS, Poon VK-M, Sun T, Lau CC-Y, Wong KK-Y, Chan JY-W, *et al*. 2014. Active replication of Middle East respiratory syndrome coronavirus and aberrant induction of inflammatory cytokines and chemokines in human macrophages: implications for pathogenesis. J Infect Dis. 209(9):1331–1342. doi:10.1093/infdis/jit504.

Ziebuhr J, Snijder EJ, Gorbalenya AE. 2000. Virus-encoded proteinases and proteolytic processing in the Nidovirales. J Gen Virol. 81(4):853–879. doi:10.1099/0022-1317-81-4-853.

# VITA

The author, Aaron Volk, was born in Geneva, IL on August 13, 1994 to Ronald Volk and Lisa O'Leary Volk. He attended Augustana College in Rock Island, IL and graduated with his Bachelor of Arts degree, *summa cum laude* and a member of Phi Beta Kappa, in May 2016. Shortly thereafter, Aaron matriculated into the Infectious Disease and Immunology Research Institute graduate program at Loyola University Chicago and joined the lab of Professor Susan C. Baker, PhD, in the fall of 2016.

For his thesis project, Aaron investigated the responses that macrophages mount against infection with coronavirus vaccine strain candidates, contributing to what is known about how coronaviruses antagonize innate antiviral immunity. He hopes that his work will be helpful in guiding the rational design of live-attenuated coronavirus vaccine candidates. Upon completion of his graduate studies, Aaron will seek employment in the healthcare industry and plans to work while he studies for the MCAT and applies to medical schools to hopefully achieve his goal of someday practicing medicine.